Title
Flame Dynamics and Chemi-Ion Flows Driven by Applied Electric Fields

Permalink
https://escholarship.org/uc/item/3273d8pg

Author
Tinajero, Jesse Alexander

Publication Date
2017

Peer reviewed|Thesis/dissertation

UNIVERSITY OF CALIFORNIA,
IRVINE

Flame Dynamics and Chemi-Ion Flows Driven by Applied Electric Fields

DISSERTATION

submitted in partial satisfaction of the requirements
for the degree of

DOCTORATE OF PHILOSOPHY

in Mechanical and Aerospace Engineering

by

Jesse A. Tinajero

Thesis Committee:
Professor Derek Dunn-Rankin, Chair
Professor Vince McDonell
Professor Manuel Gamero

2017

DEDICATION

To everyone who

gave me their encouragement

throughout my life

and

to all those

who believed in me.

TABLE OF CONTENTS

LIST OF FIGURES

LIST OF TABLES

Page

ACKNOWLEDGMENTS

First and foremost, I would like to thank Professor Dunn-Rankin for the tremendous opportunities that he has granted me for the past five years. He has provided me with opportunities that I could not have imagined I would be apart of before joining his lab. The environment that he has welcomed me into has been one that has allowed me to grow as a student, a researcher, and a person.

Without my labmates, It would not have been possible for me to have enjoyed and progressed in my work as much as I have. Everyday spent in the lab I have learned from them. Everyday spent in the lab I was challenged by them. Everyday spent in the lab I feel pushed to improve myself and my work in order to keep up with them.

I especially want to thank...

those that have worked on the electric field combustion topic before me. Sunny Karnani and Alice Chien have been amazing mentors simply by showing a path to work towards.

Vinicius Sauer and David Escofet-Martin were there when I joined the LFA lab, there now that I am finishing, and have been there through out my entire graduate experience. I am so fortunate to have these two as my friends and colleagues. There knowledge, experience, and hard work have been so beneficial for me and my growth.

Marco Minniti, Ali Ziaee, and Rosa Padilla for being more than just labmates but also close friends.

Everyone who has worked with me on my research project. Claudia Camara-Lopez, Albert Aguilera, Ali Zavar, Miguel Plascencia, Alejandro Sherman, Jie Bai, Guillaume Eplenier, Dorsa Shirazi, Dustin Hall, Lewis Liao, Louise Autef, Guillaume Bernard, Igor Alves, and Francisco Javier Villegas.

This work is supported by NASA ISS Research Project via agreement NNX11AP42A, with Dennis Stocker as contract monitor.

Curriculum Vitae

Jesse A. Tinajero Jr.

Education

Summer 2017	**Doctor of Philosophy Candidate**, *The University of California*, Irvine, Mechanical Engineering. Title: *Dynamics of Chemi-Ion Driven Flows in an Applied Electric Field*
Mar. 2015	**Masters of Science**, *The University of California*, Irvine, Mechanical Engineering.
Aug. 2012	**Bachelor of Science**, *The University of Illinois*, Chicago, Mechanical Engineering.

Research Interests

Current research interests include:

The interaction between electric fields and flames.

Optical diagnostics for use in combustion research.

The effects of electric fields on flame carbon.

Electric probes for measuring electrical properties of flames.

The electric field effects on laminar diffusion flames in micro-gravity.

Overseeing the planning of microgravity experiments to be performed on board the International Space Station (ISS) through NASA Glenn Research Center's Advanced Combustion via Microgravity Experiments (ACME).

Teaching Experience

Fall, 2013	**ENGRMAE 107**, *Thermal Fluids Lab*, teaching assistant for Professor Yun Wang.
Winter, 2017	**ENGRMAE 151**, *Mechanical Engineering Design*, teaching assistant for Professor Derek Dunn-Rankin.

Work Experience

May 2012 - August 2014	**Woodward MPC**, *Skokie, IL.*, Summer Intern, IRAD Group - Hydraulics Lab.

Laboratory & Research Skills

Data Acquisition , Optics , Data Processing , Image/Video Processing , Computer Vision , Designing/Building Experiments , High Voltage Equipment

Computer Skills

Operating Systems	Windows & Linux
Programming	Python, MATLAB, Labview, C++, Cantera, OpenFOAM

Miscellaneous	Microsoft Word/Excel/Powerpoint , LaTeX , AutoCAD , Inventor , SOLIDWORKS

Academic Superivision

International Scholars

March 2015	**Albert Aguilera**, *Universitat Politècnica de Catalunya*, Relating CH* chemiluminescence with charged species in a non-premixed methane flame, Thesis.
September 2015	**Claudia Lòpez Càmara**, *Universitat Rovira i Virgili*, Numerical Study of Soot Behavior in the Presence of an Applied Electric Field, Thesis.
Summer 2015	**Guillaume Eplenier**, *ENSMA*, Chemical Kinetics Calculations of Flames with Ions and Excited Species, Intern/Project.
Summer 2016	**Louise Autef**, *ENSMA*, Experiments and Modeling of Small Diffusion Flames in Electric Fields, Intern/Project.
Summer 2016	**Guillaume Bernard**, *ENSMA*, Ion Currents from Surfaces in Small Burners, Intern/Project.

UCI Undergraduate Researchers

Ali Zavar, Miguel Plascencia, Alejandro Sherman, Dorsa Shirazi, Dustin Hall, Lewis Liao.

Academic Awards & Accomplishments

Summer 2015 & 2016	Attended Combustion Institute Summer School at Princeton University
Summer 2012	Received UIC College of Engineering Bell Honors Award
Acad. year 2011-12	UIC Motorsports - Baja SAE team leader

Journal Publications

May 2017	**Combustion Science and Technology**, *Characterizing I-V Curves For Non-Premixed Methane Flames Stabilized On Different Burner Configurations* , Primary Author: Jesse Tinajero; Co-Authors: Derek Dunn-Rankin, Guillame Bernard, Louise Autef. DOI:10.1080/00102202.2017.1331218

Academic Publications

Master's Thesis

Title	*Chemi-Ion Driven Flows in an Electric Field*
Supervisor	Professor Derek Dunn-Rankin

Conference Experience

Combustion Institute

Pasadena, US, 2014	**2014 Western States Section of the Combustion Institute**, *Schlieren Imaging of Chemi-Ion Driven Flows in a Time Varying Electric Field*, Paper/Presentation, Primary Author: Jesse Tinajero; Co-Authors: Derek Dunn-Rankin, Miguel Plascencia, Jie Bia.

San Francisco, US, 2014	**35th International Symposium on Combustion**, *Carbon Particle Behavior in Flames Exposed to an Electric Field*, Poster Presentation, Primary Author: Jesse Tinajero; Co-Authors: Derek Dunn-Rankin.
Cincinnati, US, 2015	**9th U.S. National Combustion Meeting**, *Relating CH* chemiluminescence with charged species in a non-premixed methane flame*, Paper/Presentation, Primary Author: Albert Aguilera; Co-Authors: Derek Dunn-rankin, Jesse Tinajero.
Provo, US, 2015	**2015 Western States Section of the Combustion Institute**, *Numerical Simulation of Methane/Air Flames including Ions and Excited Species*, Paper/Presentation, Primary Author: Claudia Lopez-Camara; Co-Authors: Jesse Tinajero, Guillaume Eplenier, Derek Dunn-rankin.
Seoul, KR, 2016	**36th International Symposium on Combustion**, *Dynamics of Chemi-Ion Driven Flows*, Poster Presentation, Primary Author: Jesse Tinajero; Co-Authors: Derek Dunn-Rankin.
College Park, MD, 2017	**10th U.S. National Combustion Meeting**, *Enhanced Flame Ion Production Through External Electric Fields*, Paper/Presentation, Primary Author: Jesse Tinajero; Co-Authors: Derek Dunn-rankin, Guillame Bernard, Louise Autef.

American Society for Gravitational and Space Research

Orlando, US, 2013	**2013 ASGSR Annual Meeting**, *E-FiELD FLames: Electric Field Effects on Laminar Diffusion Flames*, Presentation, Primary Author: Jesse Tinajero; Co-Authors: Sunny Karnani, Derek Dunn-Rankin.
Pasadena, US, 2014	**2014 ASGSR Annual Meeting**, *Ground-Based Schlieren Experiments of Chemi-Ion Driven Flows in a Time-Varying Electric Field*, Presentation, Primary Author: Jesse Tinajero; Co-Authors: Derek Dunn-Rankin, Miguel Plascencia, Jie Bia.
Alexandria, US, 2015	**2015 ASGSR Annual Meeting**, *Numerical Simulation of a Co-flow Methane/Air flame with an applied electrical field*, Presentation, Primary Author: Claudia Lopez-Camara; Co-Authors: Jesse Tinajero, Derek Dunn-rankin.
Cleveland, US, 2016	**2016 ASGSR Annual Meeting**, *Using Voltage Current Curves To Characterize Electric Field Effects On Flames For Different Burner/Mesh Electrode Configurations*, Presentation, Primary Author: Jesse Tinajero; Co-Authors: Louise Autef, Guillaume Bernard, Derek Dunn-rankin.
Cleveland, US, 2016	**2016 ASGSR Annual Meeting**, *Numerical Simulation of Flames under the Influence of Electric Field*, Presentation, Primary Author: Claudia Lopez-Camara; Co-Authors: Jesse Tinajero, Valentina Ricchiuti, Derek Dunn-rankin.

ABSTRACT OF THE THESIS

Flame Dynamics and Chemi-Ion Flows
Driven by Applied Electric Fields

By

Jesse A. Tinajero

DOCTORATE OF PHILOSOPHY in Mechanical and Aerospace Engineering

University of California, Irvine, 2017

Professor Derek Dunn-Rankin, Chair

The enhancement to laminar, non-premixed flames by the application of an external electric field is studied. It has long been known that naturally occurring ions are produced through chemical reactions during the combustion of hydrocarbon flames. Chemi-ionization has been noted in the literature as the source of naturally occurring flame ions and electrons. Because chemi-ions exist in very small quantities within the flame (10^9 - 10^{10} ions/cm^3), they contribute very little to the overall natural combustion process and can usually be neglected in conventional combustion applications/studies. However, with the application of an external electric field, the chemi-ions/electrons can have a dramatic effect on combustion through ion driven winds.

Ion current measurements are characterized for conical-type methane flames stabilized on axially symmetric burners with longitudinal electric fields applied. The ion currents are used to correlate the flux of chemi-ions to measured flame characteristics. The manipulation of the flame by ion winds is analyzed through CH^* chemiluminescence where flame geometry and light emission are the main targets to be studied. The modification to the thermal flow field is analyzed through schlieren imagery. The visualization through schlieren demonstrates how ion winds enhance the exhaust gas and provides a means of analyzing the interaction between ion fluxes and surrounding neutral flow. Numerical CFD models are described and validated. Ion wind body forces are generalized to simple body forces to test the extent to which ion winds can be used to describe the experimental observations. The numerical models provide a means of studying more in-depth complicated interactions of the flame and gaseous flows to enhanced body forces. Finally, a theoretical model is developed which highlights the important mechanisms involved in the modification of flame and gas flow dynamics by body forces due to gravity and external electric fields.

Ion winds are shown to be the dominant mechanism in external electric field enhanced combustion. Ion winds explain nearly all of the observed effects on flames by external fields. The relatively small disparities that do exist between the experimental results and numerical results are likely from the uncertainties associated with chemical kinetics of minor species with extremely small concentrations and the use of simplified transport in the simulation.

Chapter 1

Introduction

Calcote [1948] was among the first to show how transverse electric fields can be used to deflect burner stabilized flames, and he explained that the observed effects "can be almost completely explained by a mechanical interpretation." Calcote's historic paper dates back half way into the 20th century, however, the idea of a mechanical drag can be attributed to the even earlier work of Chattock [1899].

The mechanical drag has been given the name "ion wind" among the electric field combustion community. Ion wind theory claims that naturally occurring ions and electrons are accelerated in response to a Lorentz force from the external field. These charges are extracted from the flame and undergo continuous non-reacting molecular collisions with neutral molecules thereby producing a net acceleration in the exhaust gas. This acceleration changes the flow behavior and results in some modifications to the flame behavior; in the example of Calcote [1948], the modified flame behavior is a deflection of flame shape.

Ion wind has been studied over the decades, e.g. Lawton and Weinberg [1970], and to this day it is still considered to be the dominating mechanism behind the observations made when applying external fields to flames. However, before ion winds can be discussed further, a discussion on the competing theories to ion winds should be made.

The only major competing theories to the ion wind theory involve the role of electrons. Because electrons are so small compared to chemi-ions they contribute much less to ion winds because of the fewer number of collisions they undergo while migrating through the inter-electrode space. Therefore, electrons have been hypothesized to contribute to the experimental observations through two means; Joule heating (thermal) and electron enhanced chemical kinetics.

Joule heating effects via high energy electrons are widely understood to be very small compared to heat release from the combustion reaction. An example can be found from Jaggers and Engel [1971] who estimated the electrical power of their experiments to be on the order of 1 W (compared to the combustion power of approximately 10^4 W) and this small power dissipation could only increase the flame temperature by 1° K.

Miller [1973] attempted to define electron induced chemical effects by suggesting that "overheated" electrons accelerated by the field can undergo collisions with free radicals in the flame front producing additional vibrational excitation states leading to enhanced chemical kinetic reaction rates. Possibly the most cited study that favored electronic chemical kinetics was made by Jaggers and Engel [1971] who used the theory to explain their observations of increased burning velocities. It is interesting to note that a year later, a not as well cited study was published by Jaggers et al. [1972] which claimed that "The burning velocities obtained again showed <u>no</u> appreciable variation." The burning velocity measurements that they were referring to was from the burner stabilized experiments made by Bowser and Weinberg [1972] who discredited the electronic chemical theory in favor of ion wind theory. A comprehensive summary of the electronic chemical effects can be found in the review of Fialkov [1997] who concluded that "a high-frequency electric field affects the propagating flame velocity, but shows little or no effect on the burning velocity of the flame on the burner." That is to say that while premixed flames appear to propagate faster, their actual burning rate is unchanged.

Marcum and Ganguly [2005] explained that their flame instabilities were caused by a thermal-diffusive effect created by a lowering of the flame's global Lewis number via highly mobilized, highly diffusive chemi-ions. To explain their observed increase to the laminar burning speed, they suggested an "electric pressure" effect. Wisman et al. [2007] elaborated further by claiming that the maximum ion wind induced pressure change under the theory presented by Lawton and Weinberg [1964] is insufficient to describe their observations. Their suggestion was explained to be related to a chemical kinetic effect but not one due to highly energized electrons. Rather, their chemical effects were related to the dissociative recombination of positive chemi-ions near the burner surface. This would result in an excessive amount of flame radicals in the preheating zone; namely H, OH, and O. These radicals are highly diffusive and would produce a thermal-diffusive instability by lowering the flame's global Lewis number below unity. A flame speed modification would accompany the instability and result in an increase in burning rate.

A recent series of studies by Tran and Cha [2015, 2016, 2017] arrive to a similar conclusion as Fialkov [1997]. Instead of an increase of flame propagation speed, they actually measured a decrease. However, after accounting for the velocity of the unburned gas just ahead of the flame, they determined that no significant change to the burning rate of their flame propagation experiments could be found due to the application of electric fields. In fact, they found that the velocity of the unburned gas was manipulated by ion winds. A recent theoretical model produced by Murphy et al. [2017] found that the role of electrons is only important at high field strengths and only through thermal means (Joule heating) and not chemical (at least not primarily chemical).

While the majority of the electric field combustion community has come to an agreement that ion wind theory could almost completely account for the observed effects, attempts to describe the effects favoring chemistry still remain. An important purpose of this dissertation is to answer the following two questions.

1. Is ion wind theory enough to explain the effects observed when an external electric field is applied to a methane flame stabilized on an axisymmetric burner?
2. How does an ion wind produce these observed effects?

Because non-premixed flames are far less studied than premixed flames, non-premixed flames will be the the focus of this dissertation. In order to answer the two above questions, it is first necessary to observe what are the effects of external electric fields on methane non-premixed flames. Both transient and steady state dynamics will be studied on the interaction between chemi-ions with the flame dynamics and the thermal flow field from the perspective of ion wind theory.

The procedure to answer these two questions is as followed.

Current-voltage (i.e, I-V) curves are first presented in order to characterize the observations based on ion current measurements rather than solely electric field strength. The ion current measurements will be correlated to various flame characteristics. This will demonstrate how important ion current measurements are to electric field combustion studies, especially since burner/electrode geometries can have a major effect on the results.

The interaction between external electric fields and flame dynamics will then be studied through the resulting flame geometry and flame light emission from CH^* chemiluminescence under varying electric field strengths. The flame geometry is an important combustion parameter that could have significant effect on the flame's full structure. As described in the above paragraphs, the flame's geometry can be significantly manipulated by external fields. This section will study how this manipulation could have an effect on the rest of the flame's characteristics.

The thermal flow field is then studied using high-speed schlieren imagery. Ion wind theory suggests that the external electric fields are able to modify the flame first through the interaction of chemi-ions and the flow field. Studying the flow field is no simple task since chemi-ions and electrons don't allow for many flow diagnostic techniques to work reliably. The un-intrusive characteristic of schlieren imagery makes it the optimal method for studying the flow field.

Because the experimental methods are limited in the amount of information that can be extracted, numerical simulations are helpful to tie together the observed information to the suggested hypotheses. The numerical simulation will be validated by comparing predicted results to experimental results. The numerical simulation will then be used to look at aspects of how ion wind body forces may form the experimentally observed enhancement to the flame dynamics and thermal flow field.

As it is true for all areas of science, theoretical models are necessary for identifying the underlying mechanisms involved in the manipulation of flames and their flow fields by external electric fields. The final task in this dissertation will discuss the development of a simple model based on the Roper flame model first described by Roper [1977] and an electrically modified Bernoulli's equation.

Chapter 2

Burner & Electrical Configuration

It is common practice in combustion research to reduce problems to one dimension in hopes of simplifying the problem so that very specific aspects can be studied without the complexity of multidimensional convection effects. The same is true for electric field combustion studies. Studies of premixed flames under the influence of external fields on flat flame burners have been performed, for example, by Bowser and Weinberg [1972], Xu [2014] and Sánchez-Sanz et al. [2015]. However, non-premixed flames are more complex. Two recent examples of electric field studies of non-premixed flames stabilized on counter flow burners can be found in Guerra-Garcia and Martinez-Sanchez [2015] and Park et al. [2016]; such burners are traditionally analyzed along the centerline to reduce non-premixed flame problems to one dimension. It is clear from these studies, however, that such simplifications cannot be made with electric field combustion problems because of the two dimensional effects inherent in the presence of ion winds. The experimental configuration chosen for the current study is a methane flame stabilized on a co-flow burner. This type of burner is two dimensional but axisymmetric and it has been widely studied; e.g. Burke and Schumann [1948], Smooke et al. [1991], Ma et al. [2015].

Three different burner configurations were tested in the experiment; a coflow burner (Fig. 2.1a), a coflow burner with an extruded central fuel tube (Fig. 2.1b), and a jet burner (Fig. 2.1c).

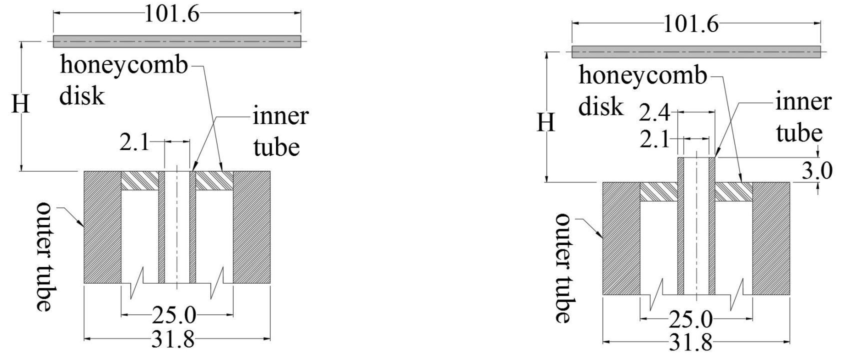

(a) Coflow burner with flush fuel tube

(b) Coflow burner with extruded fuel tube

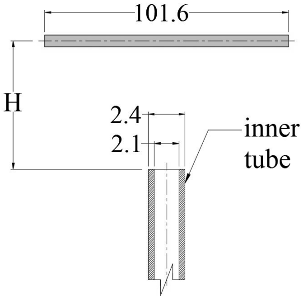

(c) Jet burner

Figure 2.1: Burner configurations: section views. All burner materials are made with stainless steel. The downstream mesh electrode was made from stainless steel material. All dimensions are in millimeters.

All components of the burners were made from stainless steel. In all experiments, the burner was configured as the grounded electrode. A circular, stainless steel mesh was used as the second electrode. The mesh was coaxially placed above the burner. For the two coflow burner configurations, the height of the mesh electrode above the burner, H, was measured from the top surface of the coflowing section to the central plane of the mesh. This is shown in Figs. 2.1a & 2.1b. In the jet burner configuration, H was defined from the height above the tube exit. The different definitions of H were chosen to provide the best representation of a global characteristic value of the electric field strength produced externally by the power supply. Two values of H were tested in these experiments; 2.5 and 3.5 cm. Other important dimensions are shown in these figures. Sample raw images of the flames from each burner are shown in Fig. 2.2.

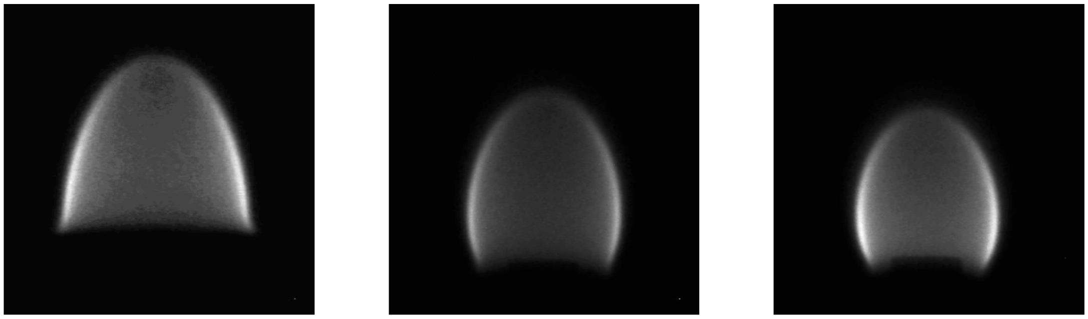

(a) flush fuel tube (b) extruded fuel tube (c) jet burner

Figure 2.2: Sample raw flame images for each burner.

The decision to use these burners was based on two criteria. First, as mentioned at the start of this chapter, premixed flames have been widely studied and one dimensional non-premixed burners (e.g. counterflow burners) are not suitable for the complexities inherent in ion wind driven convection. Coflow and jet type burners, on the other hand, are axially symmetric 2D burners that are well studied for non-premixed flames and can retain their symmetry even when ion driven winds are present.

Second, these three types of burners represent three electric field distributions (see Appendix A). The coflow burner with flush fuel tube represents the case (without a flame) of two charged plates that would ideally form a uniform field with parallel electric field lines. Analytically, the electric field is equal to $-\triangle V/H$. The jet burner represents the simple case (again without a flame) of point to plane electrodes that form an electric field that converges to the thin burner tube. The strongest local electric field is expected to be near the fuel tube tip. The coflow burner with the extruded fuel tube is an intermediate configuration that uses characteristics from both plane to plane and point to plane. In this case, the electric field lines maintain quasi-parallel form but also allows for a flame structure similar to the jet burner.

The details of the local electric fields will vary from the idealized fields, especially near corners, sharp edges and within the low density regions produced by the flame. Though rarely critical for ion wind driven flow assessments, when such details are needed, electric field solvers are available, again for cases with no flame. Simulations of how the burner configurations affect local electric fields without a flame were performed by Karnani [2011].

The gas flows were metered through individual rotameters which were calibrated with bubble meters. Two fuels were tested, methane and hydrogen (both research grade 99.9% pure). The fuel was fed to the central tube of the burner. It is important to understand that the two major convective competitors to ion winds are buoyancy and initial gas jet momentum. The flow rate of the fuel supplied to the burner was kept low (27 & 40 mL/min measured by the rotameter at ambient temperature). A typical nozzle velocity under these flow rates is on the order of 10 - 20 cm/s. This is compared to buoyancy driven or electric field driven gas velocities which are higher than 100 cm/s. This nearly eliminates the momentum from the initial gas jet injection. For a similar purpose, the coflow section was unused for all burners. The elimination of the coflow was justified for two reasons; to test the electric field's capabilities in an equally quiescent environment for all burners and to amplify the relative effects from the air entrainment caused by ion winds. The quiescent environment was assisted by placing the burner centered inside a closed, nominally cubic acrylic housing with dimensions of 50 cm × 58 cm × 50 cm. The ambient temperature inside the housing remained at 24° C ±1° C throughout each experiment. Any exhaust gas accumulation (though insignificant) was ventilated in between each test. A Trek 609A high voltage amplifier was used to produce up to a ± 10 kV electric potential between the two electrodes. A 1 MΩ shunt resistor was placed in series with the two electrodes and the high voltage amplifier was wired between the burner and the electrical ground. This shunt resistor was used to measure the ion current through each test. A Fluke 80k-40 high voltage probe provided a real time measurement of

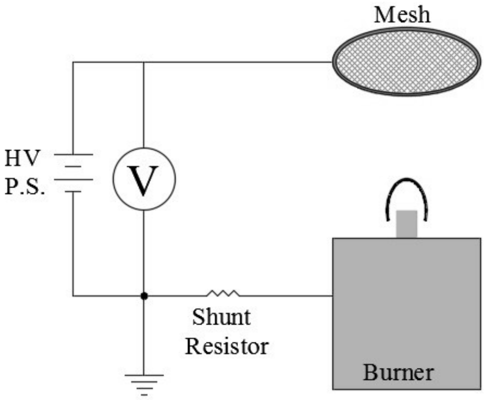

Figure 2.3: Electrical schematic

the electric potential between the electrodes. The ion current and electrode potential were measured in real time with computer based data acquisition controlled with LabVIEW. The ion current and electrode potential were each sampled at 1000 samples per second. A command signal was defined and sent to the high voltage amplifier through the data acquisition system so that sweeps could be programmed without intervention. The schematic of the electrical/burner configuration is shown in Fig. 2.3.

Chapter 3

I-V Curves

3.1 I-V Curve Introduction

Ion current measurements are an inexpensive diagnostic tool that can be used to monitor flame characteristics (though it is important to avoid artificial currents from corona discharge). The use of ion currents is wide ranging; for example Peerlings et al. [2013] studied the usefulness of using saturated ion current measurements to measure the thermo-acoustic response of flames, Boothman et al. [1969], who used saturation ion current measurements to understand flame ion production rates, and Lawton and Weinberg [1964], who used ion current measurements to estimate maximum electric field body forces. Many others have explored using ion currents in optically closed combustion systems (e.g. Badawy et al. [2012], Rao and Honnery [2015]) because of the fundamental information that they provide, e.g. ignition time and flame front location, in an analogous way to measuring temperature and pressure.

Current-voltage (I-V) curves are used in many electrical applications involved in the displacement of charge. The concept of an I-V curve for an ion producing flame is described in

Fig. 3.1. As the applied electrode voltage is increased (from left to right), the ion current gradually increases until it reaches saturation. At saturation, the total rate of chemi-ions extracted from the flame is equal to the rate at which chemi-ions are produced inside the flame. Field strengths above this saturation point cannot, therefore, increase the ion current.

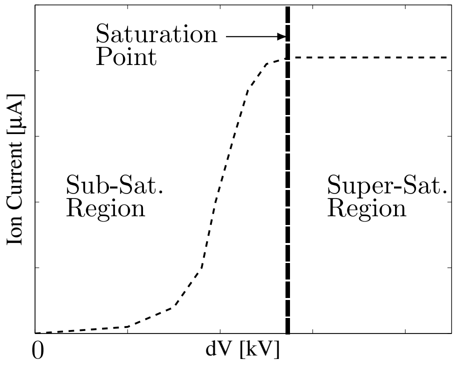

Figure 3.1: Simple voltage current curve.

Considering that external electric fields alone are not enough to produce ion winds since a sufficient number of ions need also to be present, see for example Lawton and Weinberg [1970], I-V curves have the potential to serve as an outstanding global indicator of the strength of electric field body forces in electrically actuated flame systems. In fact, the local electric body force scales directly with the local current density (or ion flux). The ion current production rate within the flame can also be determined from the ion current saturation point in the I-V curve. An interesting feature of the I-V curves that will be discussed in this chapter is the enhancement to the ion current at field strengths above the saturation point and how this varies for different burner/electrode configurations. Since saturation should prevent further ion current, the super-saturation ion current must arise from a change in the flame or from leakage current. The hypotheses proposed are i) a mixing of fresh oxidizer with fuel near the base of the flame formed by ion winds enhancing reaction rates and flame temperature to produce more ions, or ii) secondary ionization mechanisms such as thermal ionization, corona discharge, or electron collisional avalanching. To demonstrate the value of studying I-V curves, this chapter explores electric field influences on small non-premixed flames in the three burner configurations (Fig. 2.1), each of which creates a different electric field distribution and opportunity for convection to influence the combustion.

Despite the importance of ion currents in electric field combustion research, the majority of publications do not report them, referring instead only to field strength or voltage. To summarize, the purpose of this chapter is to: i) further demonstrate ion currents as a diagnostic tool in a way where just using simple field strength is not enough, and ii) determine the source of the enhancement of ion current measurements above saturated field strengths.

3.2 Experimental Procedure

Fig. 3.2a shows the high voltage output temporal profile applied to the mesh electrode in order to resolve and record the I-V curves. The voltage was decreased by -400 V incremental steps from 0 to -10 kV. Each step was held for 2 seconds. Here, as also found in prior work of Karnani et al. [2012], the time needed for the flame to react and stabilize after a change in field strength is on the order of 100ms. Therefore, 2 seconds was sufficient time for calculating the I-V curves. The ion current was also measured during the application of the voltage sweep. The resulting ion current measurement profiles depended on flow rate and electrode spacing, H. Two sample measurements are shown in Figs. 3.2b and 3.2c.

To produce the I-V curve, the ion current was averaged over the 2 seconds at each voltage step. The red lines in Figs. 3.2b and 3.2c represent the value of the averaged ion current measurements. Also, notice that a short spike in ion current occurs at the instance the voltage is increased. This spike in ion current is the contribution of capacitive electric current needed to displace charge from one electrode to the other in order to generate the electric potential. The capacitative ion current lasted less than 10 ms in all cases (<10 samples). The combination of capacitative spike in ion current and transient flame motion were found to have a negligible effect on the average value of the ion current.

The ion current shown in Fig. 3.2c became unstable at high field strengths and eventually fell to zero. The instability was caused by flame fluctuations and the zero ion current occurred at flame extinction due to the ion wind blowing out the flame.

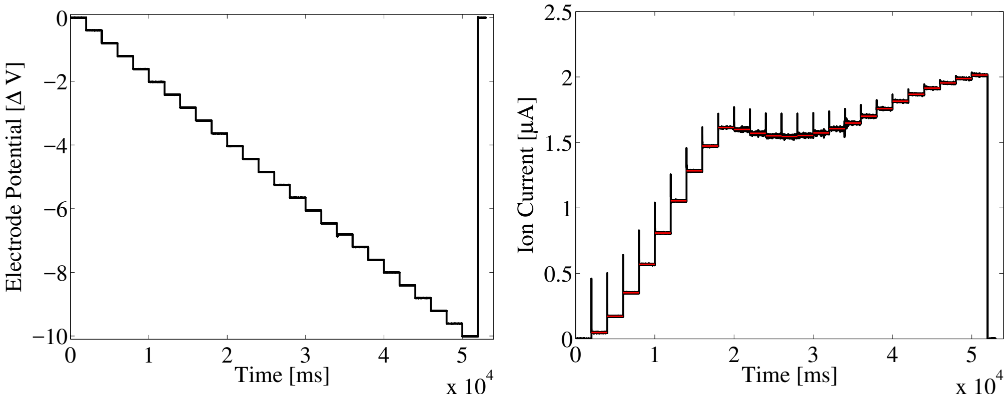

(a) Sample electrode potential profile

(b) Stable ion current

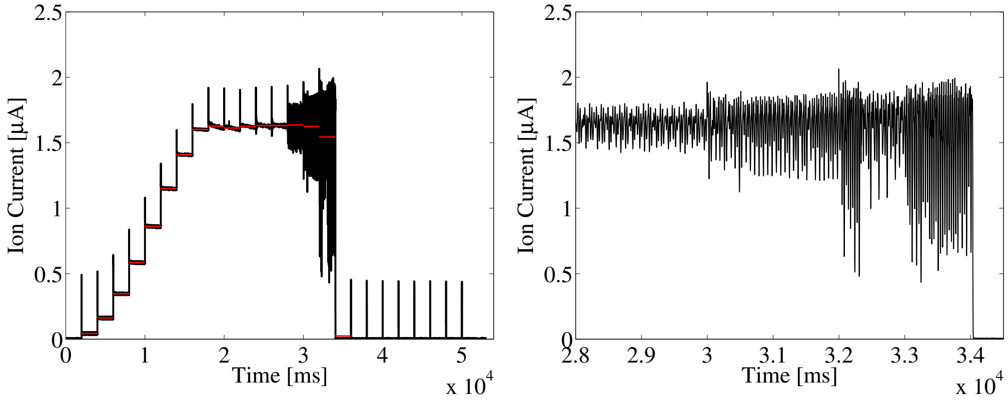

(c) Unstable ion current

(d) Close up of ion current instability

Figure 3.2: Sample measurements

3.3 I-V Curves Results

The average value of the ion current at each voltage step was calculated and plotted against nominal field strength. The latter is equal to the applied electric potential to the electrodes divided by the spacing between the electrodes.

$$E_{nominal} = -\frac{\triangle V_{app}}{H}. \tag{3.1}$$

The I-V curves are shown in Fig. 3.3. The left column presents the experiments performed with H = 2.5 cm while the right column displays the experiments performed with H = 3.5 cm. Each figure includes methane at two flow rates (filled symbols) and hydrogen at two flow rates (open symbols). Error bars in these figures represent the standard deviation of the instantaneous ion current value from the averaged value at each step.

3.3.1 Methane Flame Results

For methane, ion current saturation was achieved at approximately 1 kV/cm in all cases regardless of electrode spacing and flow rate. With a flush coflow burner, a clear saturation ion current was achieved and remained the same above 1 kV/cm until about 3 kV/cm. Above 3 kV/cm, the ion current began to increase again. The coflow burner with an extruded center fuel tube showed a similar behavior, however, the increase in ion current began at approximately 2 kV/cm. The jet burner had a constant saturation ion current, however, large error bars are shown representing large instabilities above the saturation point. Fig. 3.2d is an example of an unstable ion current measurement that would produce such large error bars.

In general, the standard deviation of the ion current from the averaged values are fairly small. This was seen in Fig. 3.2b, where under a steady DC field strength, a stable flame can provide a steady flow of ions. However, large instabilities were observed that were able to force flame extinguishment under strong enough field strengths. This was particularly pronounced with the jet burner where the flame extinguishment was observed at approximately 2 kV/cm (Figs. 3.3e and 3.3f). The extruded coflow burner did not experience a flame extinguishment until

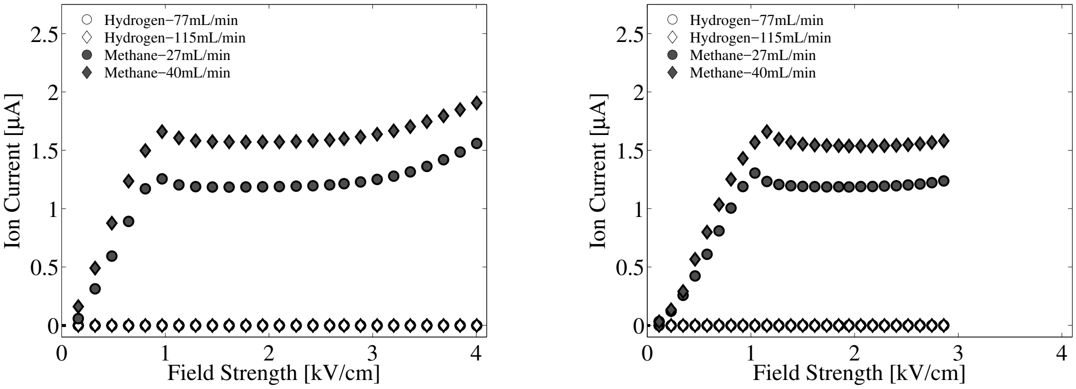

(a) Coflow flush burner - 2.5 cm

(b) Coflow flush burner - 3.5 cm

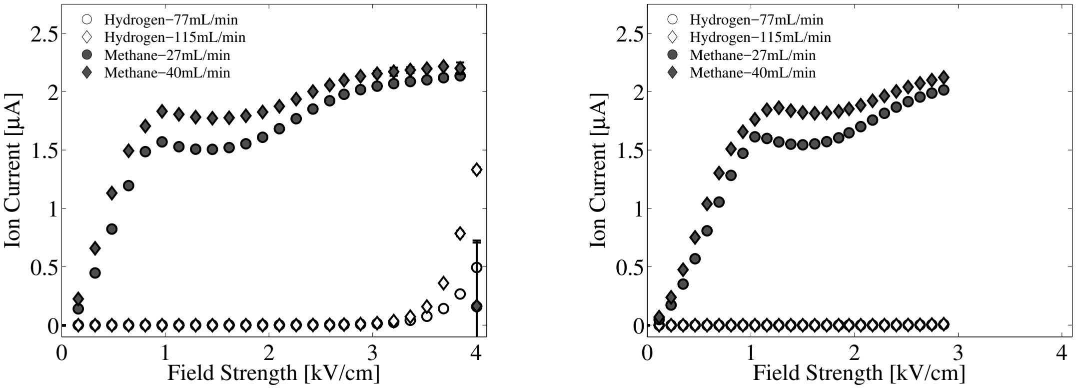

(c) Coflow extruded burner - 2.5 cm

(d) Coflow extruded burner - 3.5 cm

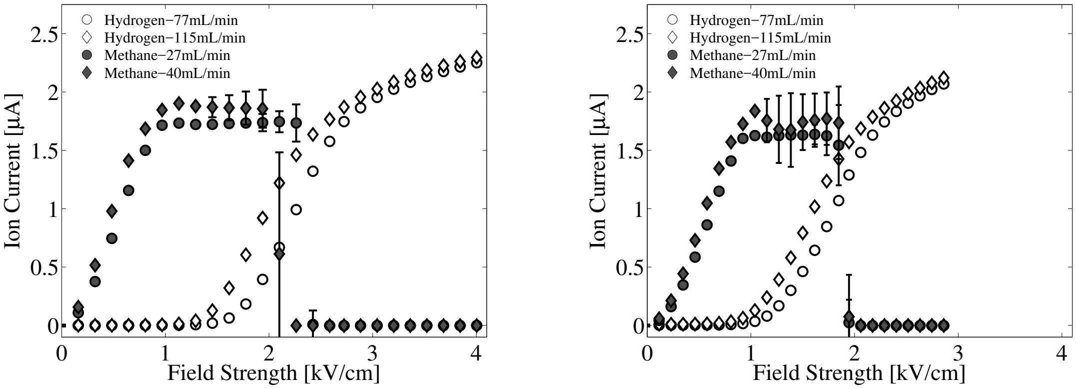

(e) Jet burner - 2.5 cm

(f) Jet burner - 3.5 cm

Figure 3.3: I-V curves: error bars represent the standard deviation of the instantaneous values from the average values at each voltage step.

4 kV/cm (Fig. 3.3c).

3.3.2 Super-Saturation Ion Current

An increase in ion current beyond saturation has been observed before. For instance, Yamashita et al. [2009] described that this could be due to air entrainment into the fuel flow creating a partially premixed region just ahead of the flame. The experiments of Weinberg and Carleton [2009] showed that no discernible changes in saturation ion current could be found under an admixture of less than 70% air content on a volumetric basis. Especially above 80% air admixture, large increases in saturation ion current were measured. However, for admixtures under the 70% limit the saturation ion current only scaled with fuel flow rate, and thus, only with carbon atom addition. Karnani and Dunn-Rankin [2015] suggested that the increase beyond saturation was due to secondary ionization mechanisms, specifically pointing to thermionic emission from the hot surface of the burner as the source.

The three competing theories for increases in ion current beyond saturation that have been discussed in the literature are summarized here (e.g. Yamashita et al. [2009], Weinberg and Carleton [2009], Karnani and Dunn-Rankin [2015]);

i) While electrical breakdown is highly unlikely due to the small field strengths used in these experiments ($\ll$ 30 kV/cm), the possibility of local breakdown due to mechanisms such as corona discharge and thermionic emission are possible. Such secondary ionization mechanisms are likely to be dependent on electrode geometry and may be enhanced by the low density gas created by the flame.

ii) Negative charges are mostly thought to be electrons since studies have shown very low concentrations of negatively charged ions in flames, e.g. Goodings et al. [1979], Prager et al. [2007]. However, high energy electrons within large electric fields may provide enough energy to release further electrons upon impact with neutral molecules. This type of secondary ionization mechanism is generally thought to happen with large negative electric fields where electrons are repelled from the flame away from the burner.

iii) Enhanced air entrainment caused by ion winds may also provide dramatic changes in local mixing, which could then affect reaction rates. This mixing enhancement is especially effective near the flame base where the interface between fuel and oxidizer region is hardest to define.

3.3.3 Hydrogen Flame Results

In order to test for corona discharge, the voltage profile from Fig. 3.2a was applied to the burner configurations without a flame. In all cases, no ion current was measured throughout the entire voltage sweep confirming that corona discharge (at least with no flame present) is not responsible. In order to test for thermionic emission, a hydrogen flame was stabilized on the burner and tested with the voltage profile. It is well-known that hydrogen/air flames do not produce chemi-ions in any significant number because the lack of carbon eliminates the strongest chemi-ion pathways. No ion current was measured with the flush coflow burner over the entire voltage sweep. A significant ion current was measured with the extruded burner above 3 kV/cm. Even more substantial ion currents were measured with the jet burner above 1 kV/cm. These results can be seen as the open symbols in in Fig. 3.3.

Comparing the ion current profiles from the hydrogen flame with the methane flame shows interesting correlations. One correlation is that hydrogen fueled systems emit significant ion currents at field strengths matching where instability was measured in the methane flame tests. This is also true for the cases where the methane flame was extinguished.

The comparison between hydrogen and methane ion current profiles also reveals that (for the coflow burners) the initial increase in saturation ion current is at field strengths lower than those able to produce ion currents in the hydrogen flames. This finding suggests that the flame is producing an increase in saturation ion current with the help of an ion wind before secondary ionization appear.

3.3.4 Further Discussion

It will be shown in the following chapter that the increase in saturation ion current is coupled to the flame geometry and, more specifically, the ability of large positive ion winds to slowly detach the flame from the burner. The base of a lifted flame possesses edge flame characteristics; see for instance Chung [2007]. These characteristics, such as propagation speed, are made possible by the formation of a partial premixing region just upstream of the flame base. It seems plausible, therefore, that an electric field detached flame can produce a partially premixed flame region with an air dilution exceeding 70%. The concept of electrically controlled mixing would provide an interesting demonstration of how electric fields can control flame characteristics through ion winds and a useful feedback mechanism for the control of flames.

3.4 Electric Probe

The ion current measurements presented in this chapter were shown to provide valuable information about the interaction between ion winds and flame dynamics. However, these ion currents are global measurements representing charge displacement. Local measurements, i.e. ion current density, are desired to quantify the ion wind body force. The classic work of Lawton and Weinberg [1964] and Lawton et al. [1968] first described the concept of using ion current measurements to quantify ion wind body forces in order to predict gas flow velocities. Their simple, idealized theory gave predictions of an ion wind body force of 8000 N/m^3 which enhance combustion gas flow rates to velocities on the order of 5 m/s. The ion current density that they used for their calculations was 250 μA/cm^2 which they acquired from a premixed flame. Xu [2014] also attempted to quantify the ion wind body force for similar conditions but using plasma sheath theory. This study predicted ion wind body forces about half of that found by Lawton and Weinberg [1964] but still reasonable agreement when considering how different the two methods were.

The simulations of Speelman et al. [2014] and Speelman et al. [2015] studied the same premixed one dimensional flame configurations as the studies described in the previous paragraph using a detailed multicomponent reacting mixture CFD model. Their simulations included detailed neutral and chemi-ion chemistry mechanisms and Maxwell equations. The prediction of ion current density was found to be in the range of 10-30 μA/cm^3. Their predicted total ion currents and ion currents at saturation, 100-200 μA in both cases, were found to have reasonable agreement with experimentally obtained values.

Papac and Dunn-Rankin [2007] used experimentally acquired total ion current measurements in their simulations in a simple way to predict ion current densities in their chemi-ion driven flow simulations. However, this method did not allow for the interactions between the enhanced gas flows and the flame dynamics. Regardless, the simulation produced accurate prediction of the enhanced gas flow as observed through their schlieren experiments. Belhi et al. [2010] used a much more detailed simulation to predict the interaction between ion winds and flame dynamics for a two dimensional conical type flame.

A simple simulation similar to the one produced by Papac and Dunn-Rankin [2007] but with the capability to predict flame dynamics and ion wind interactions is also desired. Aside from simplifying the chemi-ion mechanisms, more experimental studies are needed to understand how chemi-ions and electrons are transported through the inter-electrode space and how they enhance the combustion environment. One such experiment was demonstrated by Papac [2005] who used a spherical electric probe to measure directly the ion current density just ahead of a downstream mesh electrode. It was found in this study with a "point-to-plane" type burner-electrode configuration that the profile of the ion current density match that of a Warburg distribution: see Sigmond [1982]. Papac [2005] found that the ion current density measurements could fit well the two parameter function shown in Eq. (3.2).

$$\frac{j(r)}{j_0} = b\left(\frac{H}{\sqrt{H^2 + r^2}}\right)^m \tag{3.2}$$

In this empirical formula, b is a scaling factor and m is the Warburg exponent. From Papac [2005], m was found to be a function of field strength. However, the actual relationship of m to the field strength was never determined.

A similar electric probe experiment was performed on the burner/electrode configuration used in this dissertation. The objectives of performing this experiment were to a) determine the ion current density profile of this burner electrode configuration so that they may be compared to numerical simulations, b) determine the relationship between the Warburg exponent m to electric field strength, and c) quantify the ion wind body force.

The experiment is described in Fig. 3.4. The electric probe was made from a stiff stainless steel wire with a 0.5 mm diameter that was held between a "U-shaped" horizontally translatable arm (Fig 3.4b). The position of the electrical ground and resistor was switched as shown in Fig. 3.4a. A second shunt resister with the same resistance was added in order to read the current collected by the electric probe separately from the main resistor attached to the mesh electrode. The probe was orientated horizontally and stationed 1.5 mm below the mesh electrode. It was found through preliminary tests that any closer than this could create current bleeding from the electric probe to the mesh electrode at high voltages.

The choice of a long wire probe, as opposed to the spherical probe chosen by Papac [2005], was due to the smaller length scale and less disturbance to the base experiment. The length scale of the experiment is on the order of a few millimeters in the radial direction. This is approximately the resolution which could be achieved by a spherical probe. The extra insulation that is required by the spherical probe also adds to its intrusiveness. A wire probe is harder to analyze because it produces a line measurement instead of a point measurement but the geometry is smaller and less invasive. The requirement of deconvolving the line

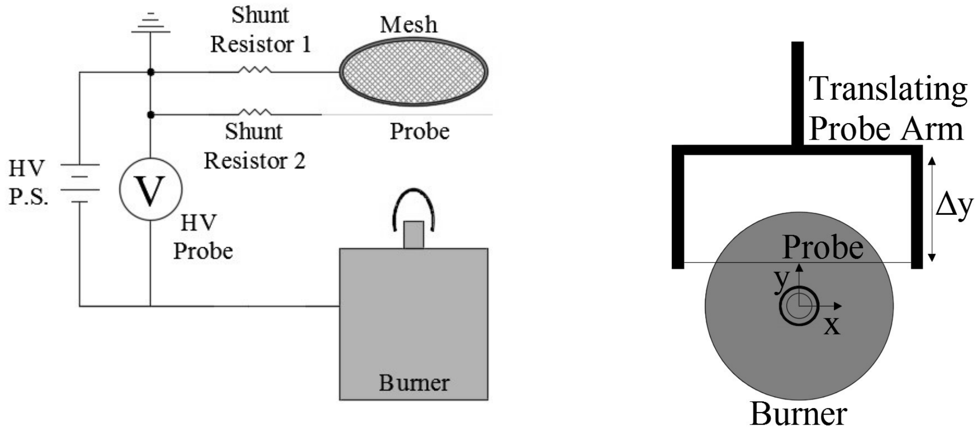

(a) Electrical schematic.

(b) Wire electric probe arm description

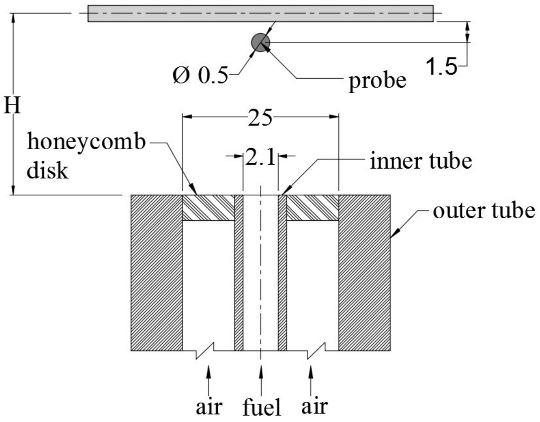

(c) Coflow burner with wire probe description

Figure 3.4: Description of wire electric probe.

measurement to a point measurement is fortunately relatively simple and common practice for radially symmetric measurements. An inverse Abel transform can be used to make this deconvolution. Dasch [1992], for example, describes several Abel inversion algorithms and compares their performance. Some contributions to the uncertainty of the algorithms are related to the distance $\triangle r$ between points relative to the signal-to-noise ratio of the projection, the presence of sharp edges (large gradients between two points), and error propagation towards the center axis.

The experiment was performed by allowing the flame to stabilize under a given electric field strength. The translating arm containing the wire moved horizontally into the flame starting

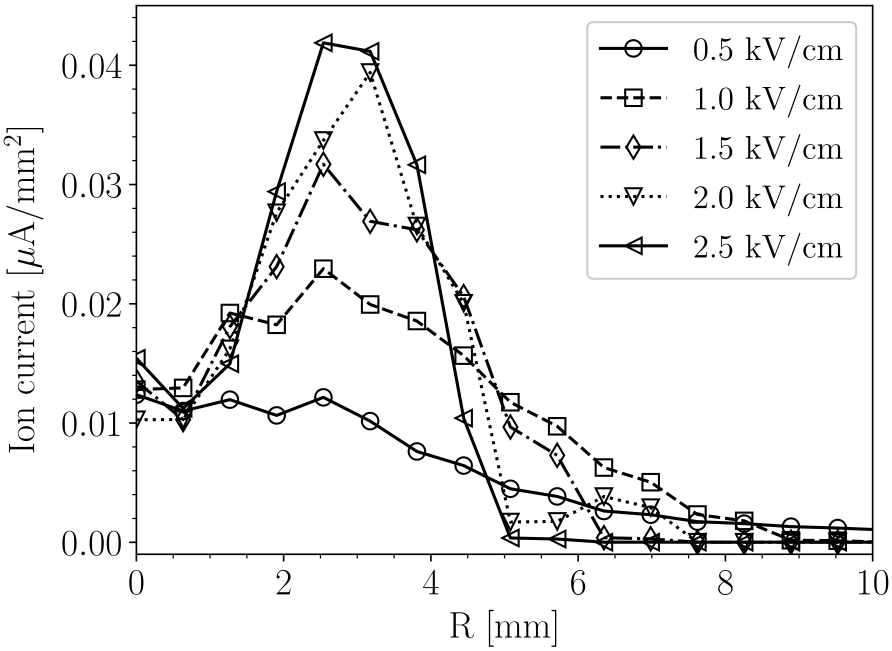

Figure 3.5: Downstream ion current density measurements acquired from wire probe measurements.

at a position far from the burner's center axis. At various positions from the center axis, the wire probe was stationed and ion current measurements were collected by the wire probe and the mesh electrode for 2 seconds (2000 samples each), after which, the probe was moved toward the center for another measurement. After a measurement was taken with the probe positioned on the burner axis, more measurements were taken beyond the center in order to verify axial symmetry. These symmetry-confirming measurements were only used for reference, not for analysis.

The results of the experiment after applying an inverse Abel transformation are shown in Fig. 3.5. The ion current density measurements were found to have a peak on the order of 2-4 μA/cm^2. The error of there measurements related to the Abel inversion The measurements above this do have extra current being produced by secondary ion current mechanisms created by high field strengths in a low density gas. The thin wire probe likely increased the potential for secondary ion currents.

The most interesting finding from Fig. 3.4 was that the ion current density does not have the same profile found by Papac [2005] (whose burner/electrode configuration was designed to simulate a point-to-plane configuration). The profile shown in Fig. 3.5 shows the peak ion current density not on the center axis as was found from the Warburg distribution profile and Eq (3.2). Rather, the peak ion current density is radially offset about 2-3 mm from the center axis of the burner. This radial position is also the radial location of the flame (This can be seen in the next chapter, Fig. 4.4). This off-set peak profile was also verified by the measurements used to confirm axial symmetry. Because the distribution is no longer of classical Warburg form, acquiring a relationship between m and electric field strength cannot be achieved by this experiment; it is very exciting to see however, that a simple change in burner electrode configuration can produce a very different result in ion current density distribution. More verification and analysis are needed for this method, but the electric probe method is a useful tool that will allow us to study the transport of chemi-ions and electrons in chemi-ion driven flows by providing spatial distributions of the important ions downstream of different flames.

Chapter 4

Flame Geometry

4.1 Flame Geometry Overview

An important concept that separates non-premixed flames from premixed flames is that the time limiting factor of non-premixed flames is the transport of fuel and oxidizer in order to provide effective mixing of reactants to the reaction zone. This is different from premixed flames where a chemical time-scale is the important time-limiting factor. Because chemical time-scales are much faster than mass transport time-scales, non-premixed flames exhibit very thin reaction zones (on the order of 1/10 of a millimeter) compared to premixed flames (approximately 1 mm). Burke and Schumann [1948] famously demonstrated how to predict flame heights of axially symmetric non-premixed flames using very simple transport theory and infinitely fast chemical kinetics. This work was expanded upon by the well-cited studies of Roper [1977] and Roper et al. [1977], who showed the effect of gas acceleration due to the body force of gravity. Other variations of the theory have been performed, for example, by Chung and Law [1984], Sunderland et al. [1997], Vázquez-Espí [2001] and Krishnan et al. [2008]. However, each of these studies built upon the underlying notion, first described by

Burke and Schumann [1948], that non-premixed flame shapes can reliably be predicted by mass transport while completely neglecting complex chemistry. In these studies, the flame geometry is usually defined as an infinitely thin line where the fuel and oxidizer are in stoichiometric proportions. On the contrary, the position of a premixed flame is controlled by the burning rate of the reactant mixture.

Simulations of axially symmetric non-premixed flames have also been accomplished. The combustion groups from Yale University have been particularly active in this arena, e.g., Smooke et al. [1992], Ern and Smooke [1993], Walsh et al. [1998] and Ma et al. [2015]. Details of numerical simulations will be discussed in upcoming chapters.

While substantial work has been accomplished on non-premixed flames, relatively little has been done regarding the response of these flames to external elecric fields. A historic paper by Calcote [1948] showed that external electric fields could be used to deflect burner stabilized flames. This effect has largely been attributed to the mechanical drag created by the drifting of chemi-ions and electrons through a mostly neutral gaseous medium. The notion of a mechanical drag, also referred to as an ion wind, has been described in another historic paper Chattock [1899].

Over the decades since Calcote [1948], many potential uses of external electric fields have been envisioned in order to control combustion in ways that traditionally could not have been achieved, but again, most of these studies have been with premixed flames. An example of an industrial application has been described recently in Barmina et al. [2016]. For both premixed and non-premixed combustion, much needs to be explored in order to understand the practicality of these visions. One phenomenon that can provide substantial insight into the potential practical value of electric field control of flames is the effect of ion currents on flame geometry.

Simulations have been performed to predict the electric field effects on non-premixed axially symmetric flames by Hu et al. [2000] and Belhi et al. [2010]. The experimental work of Sang Min et al. [2005], Won et al. [2007, 2008] and Xiong et al. [2015, 2017] have looked at the effect of AC and DC fields on axially symmetric non-premixed flames. These studies have focused on the lifting/reattachment of lifted edge flames and the formation of toroidal vortices. Kuhl et al. [2013, 2014, 2017] have looked at the electric field effect on flame structure of premixed axially symmetric flames. Chien et al. [2013] studied the electric field effect on axially symmetric non-premixed flames near an impinging surface. Their experiments focus on the transfer of heat from the flame to the surface under different field strengths and demonstrate how electrically actuated flame reaction zones can be manipulated to reduce the amount of carbon monoxide released. M. Sauer and Dunn-Rankin [2015] developed simple theoretical models for describing flame shapes in non-premixed flames near impinging surfaces but not under the influence of an electric field. The model might still be useful however if the electric body force can be effectively linked to an equivalent flow acceleration analogous to buoyancy. More on this concept appears in Ch. 7. The main point here is that flame shape does provide a potentially quantitative indicator of local convective behavior.

4.2 Brief Review of CH* Chemiluminescence

The flame's geometry was studied using CH^* chemiluminescence images of the methane flame stabilized on the burners described in Ch. 2. The light emitted by CH^* chemiluminescence is the primary source which produces a flame's characteristic blue color centered at 431 nm. CH^* is the strongest natural light emitting flame species (at least for most non-premixed flames) that can be seen by the human eye. The light collected from CH^* chemiluminescence also strongly represents the full location of the flame sheet compared to other commonly observed flames species such as OH, OH^*, and CH_2O; many of which have strong features in specific locations of the full flame. CH^* is the most commonly used flame species for comparison with theoretical and numerical non-premixed flame models when studying flame location. From these reasons, CH^* is the optimal flame species for studying the non-premixed flame geometries.

In general, the spontaneous emission of light occurs during the relaxation of a electronically excited molecule to its ground state. Three main ways to achieve electronic excitation by collisions in a gas are by *a*) the conversion of translational energy into electronic energy, *b*) the conversion of internal energy into electronic energy, *c*) and chemical reaction (chemiluminescence). Gaydon and Wolfhard [1979] described that inside the reaction zone of the flame item (c) best explains the concentrations of electronically excited radicals.

Two early reviews that describe chemiluminescence in flames can be found in the well-cited textbooks of Gaydon [1957] and Gaydon and Wolfhard [1979]. Gaydon originally suggested the production of CH^* by the C_2 reacting with OH (reaction (4.1a)). It was later suggested by Reisler et al. [1980] that a reaction between C_2H and O_2 could be the dominating reaction (reaction (4.1b)). Devriendt et al. [1996], however, provided strong evidence in favor of the reaction represented by reaction (4.1c)

Becker et al. [1980] measured the Einstein coefficient for the spontaneous emission of light from the relaxation of CH^* to its ground state (reaction (4.1d)). Later, the relaxation of CH^* to its ground state through collisional quenching, reaction (4.1e), was studied by Garland and Crosley [1988] and Tamura et al. [1998]. The details on the reaction kinetic parameters will be put off for later chapters but the accurate prediction of chemiluminescence relies on all of these reactions.

$$C_2 + OH \rightleftharpoons CH^* + CO \tag{4.1a}$$

$$C_2H + O_2 \rightleftharpoons CH^* + CO_2 \tag{4.1b}$$

$$C_2H + O \rightleftharpoons CH^* + CO \tag{4.1c}$$

$$CH^* \rightleftharpoons CH + h\nu \tag{4.1d}$$

$$CH^* + M \rightleftharpoons CH + M \tag{4.1e}$$

4.3 Flame Geometry Results

The following chemiluminescence images were captured with a Nikon D90 digital camera and a 430 nm (10 nm full width at half max) filter. Details on the procedure of imaging and quantifying of flame chemiluminescence can be found in the literature, e.g. Walsh et al. [1998], Giassi et al. [2016]. The f-number used to take these images was 5.6. The ISO setting was set to 100 and the shutter speed varied between 3 to 5 seconds depending on the strength of the light emission from the flame. After spatially calibrating the camera, the spatial resolution was found to be 17±1 microns between pixels in both the horizontal and vertical directions.

Figs. 4.1a - 4.1h show the flame's CH^* profile under varying electric field strengths. After the external field was initiated, the flames were allowed to re-stabilize before the images were taken. The images were deconvolved with an onion-peeling Abel inversion to reveal the two dimensional flame contour. Details of this Abel inversion algorithm can be found e.g. in Dasch [1992]. The pixel intensities in all the images were normalized by the maximum value in the entire series of images. This maximum was found in Fig. 4.1h. White lines can be found in the bottom left corner of each image which were artificially imposed onto the images and represent the position of the burner's fuel tube. The solid white line represents the external features of the burner while the dashed white line represents an internal feature (internal diameter). The nominal field strength is defined as before; Eq. (3.1). The images show the experiments performed using the protruded fuel tube burner.

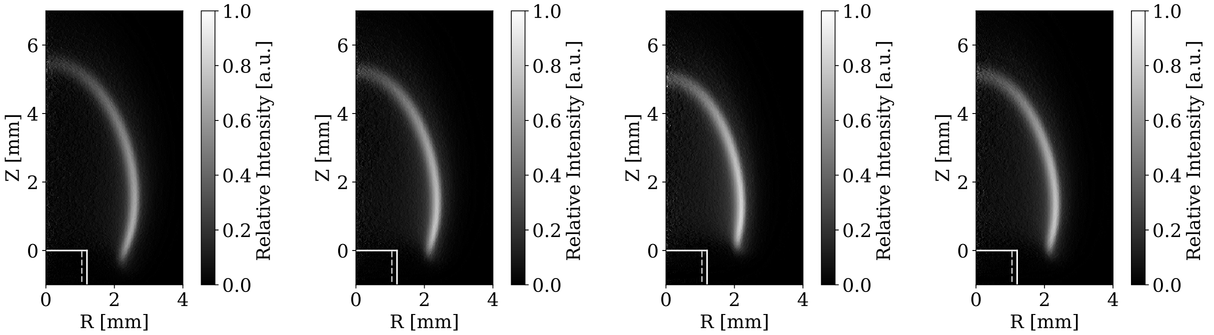

(a) 0.0kV/cm (b) 0.5kV/cm (c) 1.0kV/cm (d) 1.5kV/cm

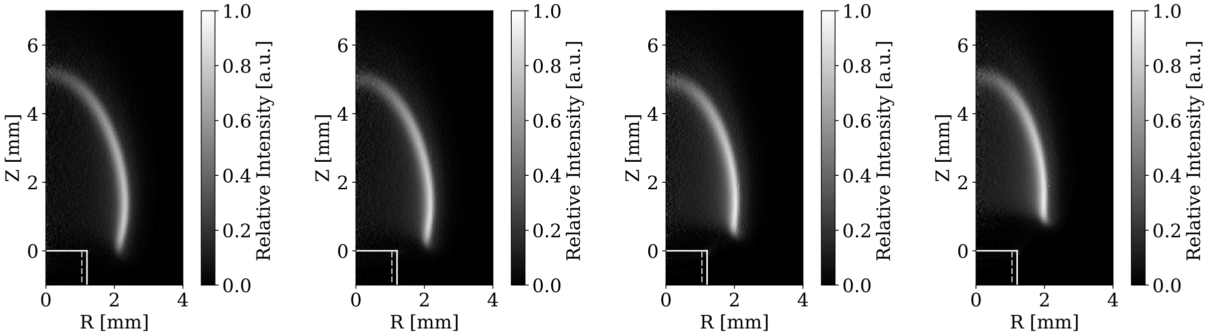

(e) 2.0kV/cm (f) 2.5kV/cm (g) 3.0kV/cm (h) 3.5kV/cm

Figure 4.1: Chemiluminescence flame contours as a function of field strength. Field strength = -$\triangle V/H > 0$. Pixel light intensity is normalized by the maximum intensity found in Fig. 4.1h. Coflow with protruding fuel tube. $H = 2.5$cm , $\dot{Q}_{fuel} = 27$mL/min

The pre-deconvoluted chemiluminescence images were carefully taken so that the images had a high signal-to-noise ratio and the flame pixel intensity profiles were found to be smooth. Also, it can be seen in Fig. 4.1 (and later confirmed in Ch. 6) that the CH^* signal is weak near the center axis. So while noise is seen to be generated radially within the CH^* signal, this region is of little interest and the actual CH^* signal is well represented. For these points mentioned in this paragraph, the uncertainties related to the Abel inversion algorithm are negligible.

What can be seen from this series of images is that the geometry of the flame subtly responds to the external electric field with a slight decrease in flame's height and a slight decrease in the flame's width. The more significant changes in this series of images is the lifting of the flame's base and increased CH^* light emission at high field strengths. These two flame characteristics will be quantified as a function of field strength near the end of this chapter.

As discussed in Ch. 3, previous simulations have predicted that the enhancement to saturated ion currents may be caused by enhanced mixing of fresh oxidizer with fuel in this flame base region, which results in a partially premixed flame as described by Yamashita et al. [2009]. The mixing is explained by entrainment of ambient air into the gas flow forced by the ion wind. The lifting of the flame seen in Figs. 4.1a - 4.1h may be the result of this mixing.

To amplify the visibility of the subtle flame shape changes, Fig. 4.2 shows the series of flame contours superimposed onto each other. The details of how the these flame contours lines were obtained can be found in App. B. The modification to the spatial features (e.g. slight decrease in height and radius and lifting of flame base height) described above are clearly visible in this figure.

Fig. 4.3 shows the effect on the flame geometry keeping all experimental parameters the same as in Fig. 4.1 except with a negative field strength. In this case, as the absolute value of the field strength is increased, the surface area of the flame dramatically increases. The flame base flares outward making the flame less curved. The CH^* chemiluminescence also significantly decreases with field strength.

The same experiment was done for the flush fuel tube exit burner. A sample series of images for this burner configuration is shown in Figs. 4.4a - 4.4i. As a note, the artificially imposed white line extends across the width of each image representing the top surface of the coflow burner and the two vertical dashed lines represent the location of the inner and

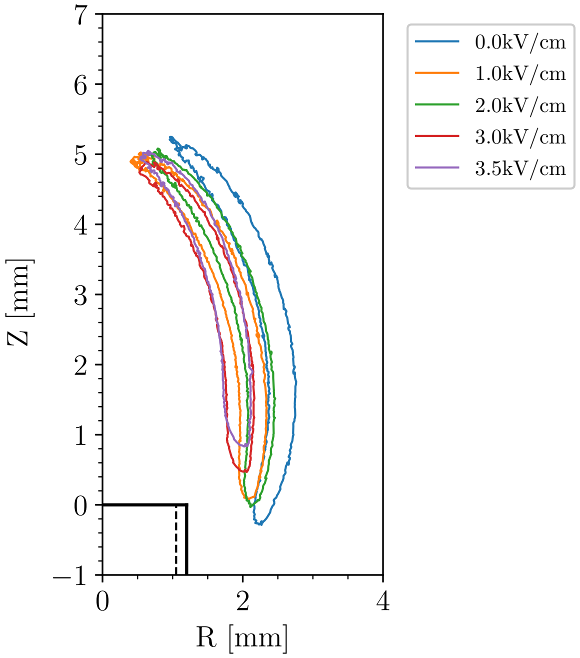

Figure 4.2: CH^* flame contours as a function of increasing field strength. Coflow (protruding) - 2.5cm , 27mL/min , $E > 0$ (See appendix for details on how contours were obtained).

outer diameter of the fuel tube.

The flames from the flush tube coflow burner emit less light than the flames from the protruding tube coflow burner. The height of the flame is taller for the flush tube case and in general they have wider radii. Also, the flush tube burner creates less curvature flames. All of these traits are likely due to the restricted air entrainment of the flush tube burner compared to the protruding tube version.

The external electric field modification to the flush burner flames have similar traits to the protruding tube case. For instance, the height and width of the flame experience a general decrease with increasing field strength. This is more clearly visible in Fig. 4.5. The pixel light value in the flame also experiences an increase in intensity with increasing field strength similar to the protruding tube case. However, the most distinctive difference of the flush tube case from the protruding tube is that the height of the base of the flame does not vary

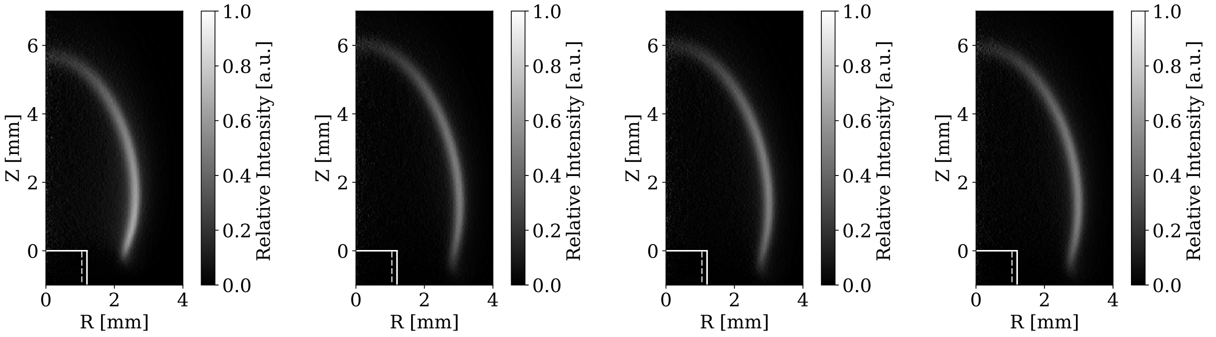

(a) -0.0kV/cm (b) -0.5kV/cm (c) -1.0kV/cm (d) -1.5kV/cm

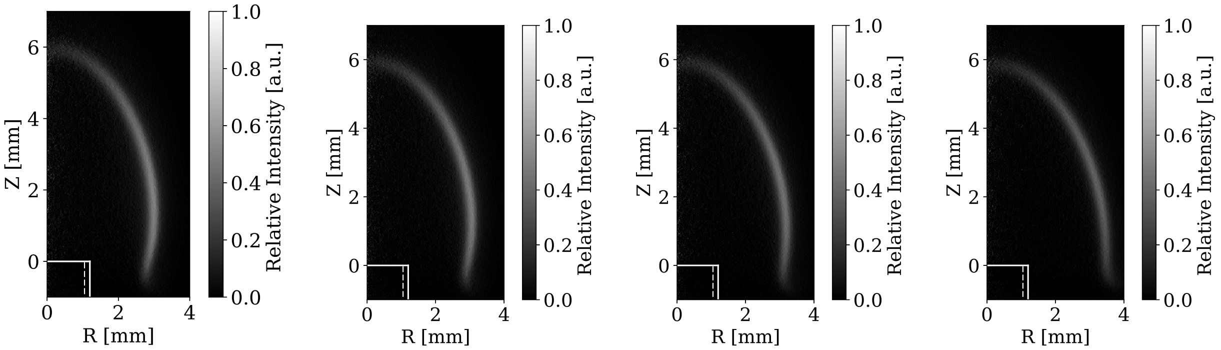

(e) -2.0kV/cm (f) -3.0kV/cm (g) -3.5kV/cm (h) -4.0kV/cm

Figure 4.3: Chemiluminescence flame contours as a function of field strength. Field strength = -$\triangle V/H < 0$. Pixel light intensity is normalized by the maximum intensity found in Fig. 4.1h. Coflow with protruding fuel tube. $H = 2.5$cm , $\dot{Q}_{fuel} = 27$mL/min

significantly with change in the electric field strength. Another interesting feature of the flush tube case is that the external field initially changes the flame geometry compared to no field, but then little variation in the flame geometry is seen until the field strength surpasses 4 kV/cm.

A summary of the analysis for all experimental configurations is shown in Figs. 4.6a - 4.6f, including a comparison with the respective ion current measurements. For the burner with the protruding fuel tube, Figs. 4.6a, 4.6c, and 4.6e, a clear trend can be seen between the height of the flame's base, the intensity of light emitted from the flame by CH^* and the chemi-ion production (identified by the ion current above 1kV/cm). While this does not directly confirm the prediction of the simulation from Yamashita et al. [2009], it is consistent

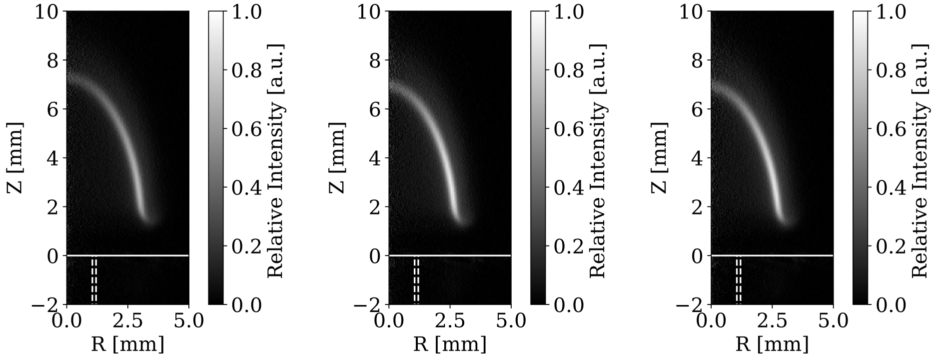

(a) 0.0 kV/cm (b) 0.57 kV/cm (c) 1.14 kV/cm

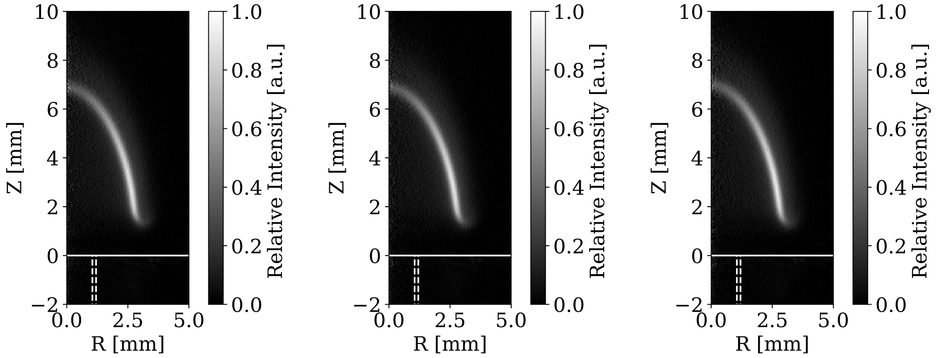

(d) 1.70 kV/cm (e) 2.27 kV/cm (f) 2.84 kV/cm

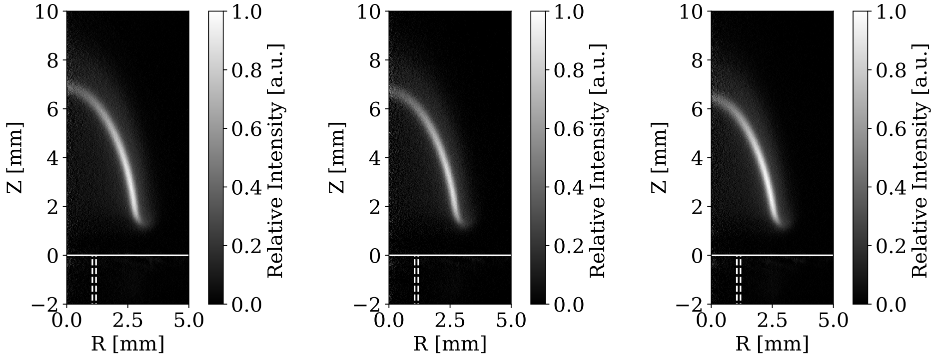

(g) 3.40 kV/cm (h) 3.98 kV/cm (i) 4.54 kV/cm

Figure 4.4: Chemiluminescence flame contours as a function of field strength. Field strength = -$\triangle V/H > 0$. Pixel light intensity is normalized by the maximum intensity found in Fig. 4.4i.Coflow with flush fuel tube. $H = 2.2$cm , $\dot{Q}_{fuel} = 27$mL/min.

with the hypothesis. Figs. 4.6b, 4.6d, and 4.6f, on the other hand, show that for a flush fuel tube the height of the flame's base is uncoupled from the CH^* chemiluminescence and chemi-ion production. Regardless of the unchanged height of the flame in these three figures,

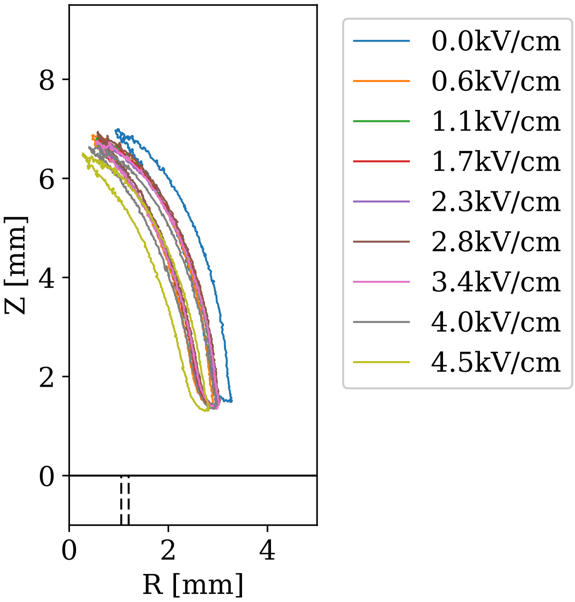

Figure 4.5: CH^* flame contours as a function of increasing field strength. Coflow (flush) - 2.2cm , 27mL/min , E > 0 (See appendix for details on how contours were obtained).

the CH^* chemiluminescence and the chemi-ion production both demonstrate enhanced levels when the electric field strength rises above 3kV/cm.

Although there are clear and reproducible electric field effects on non-premixed co-flow flame shape, because of the burner geometric effects on the results between the extruded and flush tube coflow burners, no clear conclusion can be made yet on the dominant connection between the enhanced flame dynamics and the ion currents. A study on the fuel tube geometry (tube diameter and height above the coflow section) may also be necessary and issuggested for future studies.

Although partial premixing may participate in the enhanced ion production, it may not be the only source or even the primary source. More investigation is still needed and numerical study is desired. In Ch. 6, one such numerical study will examine further the altering of flame dynamics by body forces acting on the combustion gas.

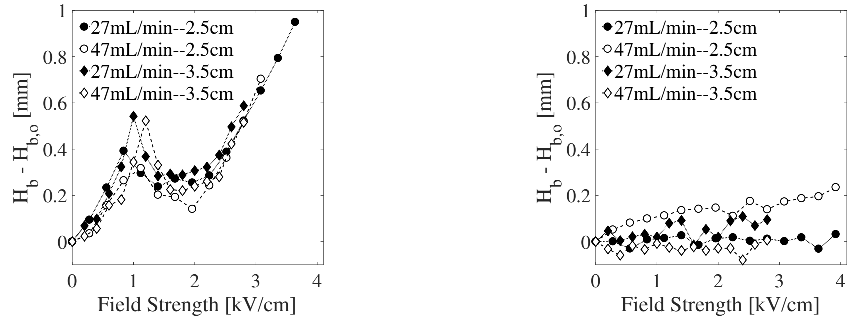

(a) Flame-base height: (protruded tube)

(b) Flame-base height: (flush tube)

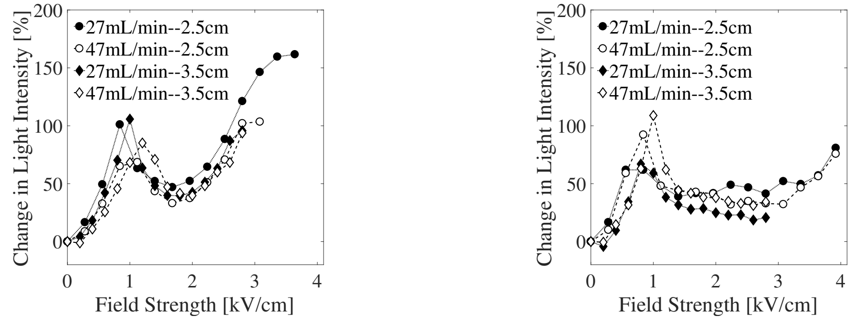

(c) CH^* light emission: (protruded tube)

(d) CH^* light emission: (flush tube)

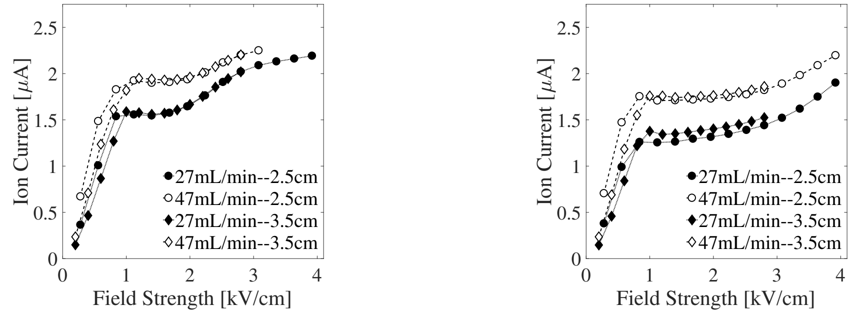

(e) I-V curve: (protruded tube)

(f) I-V curve: (flush tube)

Figure 4.6: Comparison of ion current to flame properties: 4.6a - 4.6e results for protruded fuel tube and 4.6b - 4.6f results for flush fuel tube. H is designated in each figure as either 2.5 or 3.5 cm.

Chapter 5

Gas Density Field Imaging

5.1 Introduction

Under ion wind theory, ion currents transfer their momentum onto the bulk gas through non-reacting collisions. The result is an enhancement to the flow field surrounding a flame which then leads to the experimentally observed changes to flame characteristics. Therefore, in order to observe how ion currents produce such changes, a method for visualizing the flow field is needed.

Typical methods, such as particle image velocimetry (PIV) and hot wire anemometers, are unreliable in measuring velocities of flow fields while external fields and ion currents are present. The major reason for this is because hot surfaces of particles or instruments have the potential to produce excess ion currents through secondary ion producing mechanisms such as thermal ionization. Another complication arises due to particulates acquiring charge while being seeded into the flow. This will add an extra force onto the particle body and will force it to travel along an electric field line rather than the gas streamline. This has been observed by Park et al. [2016]. Tran and Cha [2016] used oil droplets in place of solid particles to measure the gas velocity around a propagating edge flame while using DC fields. The same experiment was also done using AC fields by Tran and Cha [2017]. The goal was to measure the propagation velocity of the edge flame which is a characteristic of premixed flames. In both cases, their results demonstrate ion winds acting on their flames. Altendorfner et al. [2011] and Kuhl et al. [2013, 2014, 2017] used PIV with solid particles to study the gas velocity surrounding conical premixed flames. However, these experiments do not verify that the effects of charge attachment or secondary ions from the particles are negligible. Papac and Dunn-Rankin [2006] used schlieren as a way to visualize the flow field of a flame's exhaust gas in order to demonstrate the capability of manipulating the gaseous flow using electric fields in order to counteract against gravity forces.

Because of the complications stated in the above paragraph, PIV will not be used as the method of analyzing the flow field. Even though oil droplets may be more reliable than solid particle seedings they burn off as they reach near proximity to the flame. Thus, oil droplet based PIV is also unproductive with the burner configurations of this study. On the other hand, schlieren is an optical technique that has been proven to be reliable at demonstrating the manipulation of a flow field through ion currents.

5.2 Schlieren Introduction

Schlieren is a non-intrusive optical method that allows for the visualization of a non-uniform fluid by taking advantage of the fluid's refractive index dependence on density. Thus, for a gaseous substance with extreme temperature gradients, such as the environment created by a flame, schlieren serves as a simple diagnostic tool for studying combustion flow environments. The refractive index of a gas, n, was found empirically to have a density dependence in the form of Eq. (5.1) (also known as the Gladstone-Dale equation).

$$n = 1 + k\rho \tag{5.1}$$

The parameter k is called the refractivity, and because it has a very small dependence on the wavelength of light it can generally be considered a constant. It has also been observed that the refractive index of gases varies very slightly from 1. Using this characteristic, an often useful form of Eq. (5.1) incorporaties the definition $k\rho = \delta$.

$$n = 1 + \delta \tag{5.2}$$

where $\delta \sim O(10^{-4})$ for most gases at atmospheric temperature and pressure. Using the ideal gas law, Eq. (5.3), and the relationship between δ and ρ, a relationship between δ and temperature could be found, Eq. (5.4).

$$p = \rho RT \tag{5.3}$$

$$\delta = \delta_0 T_0 / T \tag{5.4}$$

Weinberg [1963] showed that the angle of deflection of a light beam, ϵ_y, from a test region of interest can be described by Eq. (5.5). Using Eqs. (5.2) and (5.4), a relationship between ϵ_y with temperature is shown in Eq. (5.6).

$$\epsilon_y = -\frac{1}{n} \int \frac{\partial n}{\partial y} \partial z \tag{5.5}$$

$$\epsilon_y \sim -\int \frac{\partial \delta}{\partial y} \partial z = \delta_0 T_0 \int \frac{1}{T^2} \frac{\partial T}{\partial y} \partial z \tag{5.6}$$

Here, z is in the direction of light propagation and y is direction of density gradient.

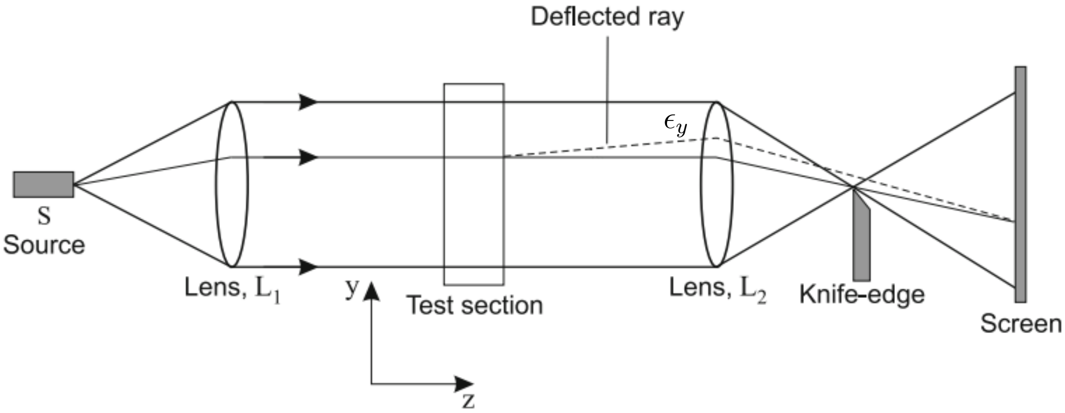

Figure 5.1: Schlieren Concept

5.3 Schlieren Introduction

Eq. (5.6) shows that the bending of a light ray will vary with the gradient of temperature. Fig. 5.1 shows a schematic of a simple linear schlieren configuration. A point source of light, s, is placed at a focal length distance away from a converging lens, L_1, in order to form parallel rays of light that are directed through the test medium. A second lens, L_2, is placed within the path of the collimated light and focuses the test medium location with respect to a screen. Even though the collimated light is being deflected by the density gradient, no luminosity variation will be produced on the screen because the test medium is in focus. The deflected light will thus appear on the screen as if it were not deflected. In order to reveal the schlieren image, a knife edge is placed at the focal point between the lens and the movie screen. The edge of the knife must be perpendicular to the direction of the temperature gradient. What will appear on the screen is the difference between the background light from the light source, L_o, and a portion of the deflected light which is a function of ϵ_y. The deeper the knife edge is positioned into the focal point the more light will be subtracted from the background light creating a stronger contrast in the schlieren image. If the knife edge completely blocks the focus spot, a dark field schlieren will result.

Fig. 5.2 is a sample schlieren image that was obtained from the experiments. Two curved,

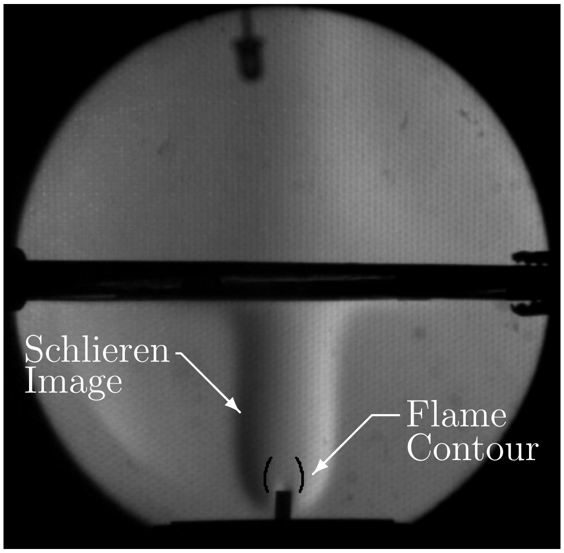

Figure 5.2: Snapshot from schlieren video.

black lines are artificially superimposed onto the image representing where the flame would lie with respect to the schlieren image. The two lines were produced by taking the peak CH^* signals from the deconvolved images from the previous chapter.

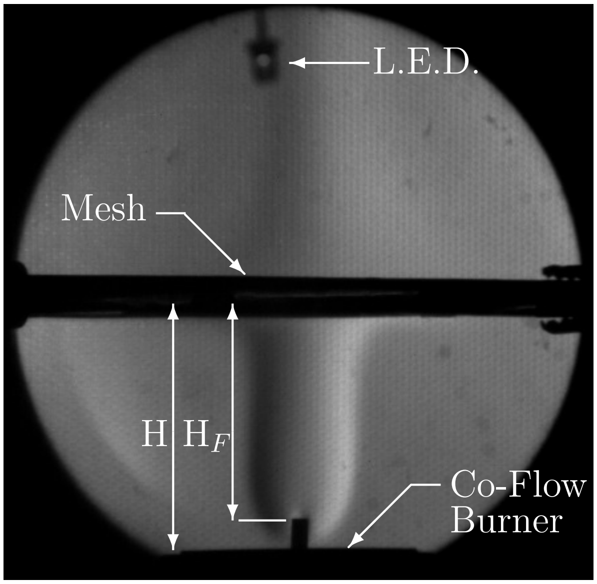

Figure 5.3: Description of components that can be seen in the sample schlieren image.

5.4 Transient Schlieren Imaging

One advantage of schlieren imaging is that the intensity is controlled by the illumination source brightness so short exposure and high speed imaging is possible even when the natural flame light is too dim to expose the camera sensor. A schlieren system similar to the one shown in Fig. 5.1 was used to study the transient behavior of the gaseous flow field created by a methane flame stabilized on the co-flow burner described in Ch. 2. A description of the components is shown in Fig. 5.3, where they show up as black silhouettes. Prior to each test, the methane flame is given sufficient time to stabilize at a specified flow rate/concentration with no external field. At t = 0 ms, the high voltage power supply is triggered to apply a voltage difference between the mesh electrode relative to the grounded burner (Fig 2.3).

An instantaneous step signal was used for the experiments. Preliminary tests showed that slower high voltage power supplies that couldn't obtain the full desired voltage within 1 ms had a major effect on the transient response of the ion current measurements. This is because the characteristic time related to ion transport is on the order of a few milliseconds. Because the transient ion current measurement is a physical indication of an ion wind force, a time dependent high voltage signal would create an unwanted characteristic time "stack up" leading to a complicated transient observation of the physical phenomena being tested; in this case the combustion flow field. Hence, for these studies a high performance high voltage power supply was necessary.

The high voltage probe was used to verify that the desired step voltage was fully obtained within 1 ms of the command signal and was constant. This ensured that the time scale related to generating the external electric field did not play a role in the analysis of the more critical combustion-relevant time scales; time scales related to ion transport, generation of ion wind through ion/neutral collisions, the interaction of the ion wind with observable flame properties, and the achievement of a new steady state.

A high-speed video camera (Vision Research Phantom V4.3) was used to capture the transient schlieren image with a frame rate of 1000 hz. At the same instance of t = 0 ms, a voltage is also applied to an LED light to determine the moment the external field is applied. The LED can be seen in the schlieren videos (Fig. 5.3). Different tests were performed using different voltage step sizes. The voltage range selected was meant to span the sub-saturation, saturation, and super-saturation regions that were described in Ch. 3.

As a brief generalization of the results, as the electric field was triggered, a change in the thermal boundary layer (schlieren boundary) was observed as a thinning of the boundary layer radius. The transient effect of the boundary layer thinning was seen as a large initial wave that began near the burner nozzle tip and propagated downstream up to the mesh electrode. Smaller secondary waves were also observed following the initial wave until the boundary layer achieved a new steady state. The new steady states were generally observed to be decreasing in radius with increasingly negative mesh electrode potential.

5.4.1 Initial Wave

A set of frames captured from one test video are shown in Fig. 5.4. The electrode spacing and flow condition for this test are associated with the 27 mL/min VCC curve from Fig. 3.3d. The applied voltage that was used was -4.4 kV applied to the mesh electrode (that is, a nominal field strength of 1.25 kV/cm). This series of images only shows the initial wave.

Each schlieren video was analyzed to study the propagation of the initial plume wave motion. Schlieren imagery is very useful for showing thermal boundary layers and helps visualize flow fields but actual velocity measurements are not directly obtainable because the schlieren is showing a gradient line and not a material line. However, the transient thermal plume wave captured in these videos results from the enhanced convection produced by the ion wind. Therefore, the plume wave may provide the order of magnitude of the enhanced convection.

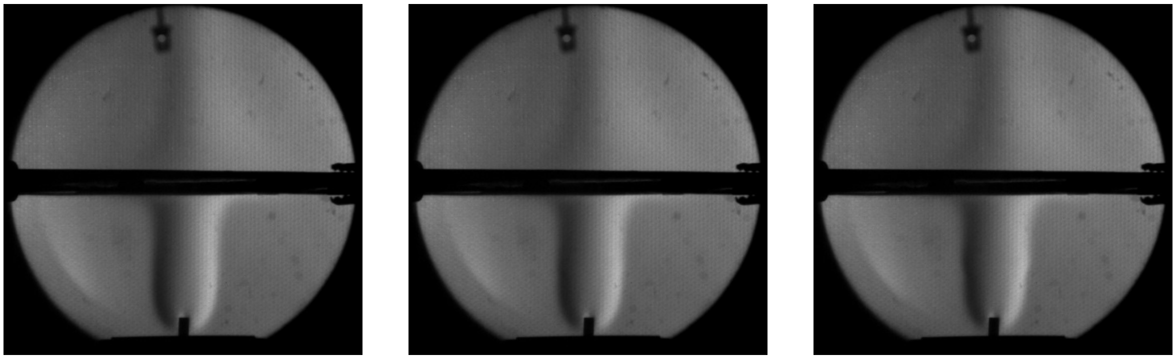

(a) 0 ms (b) 5 ms (c) 10 ms

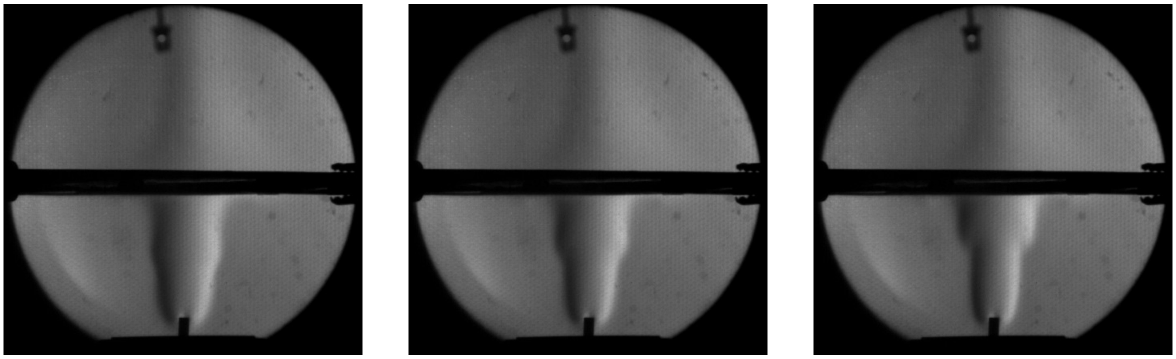

(d) 15 ms (e) 20 ms (f) 25 ms

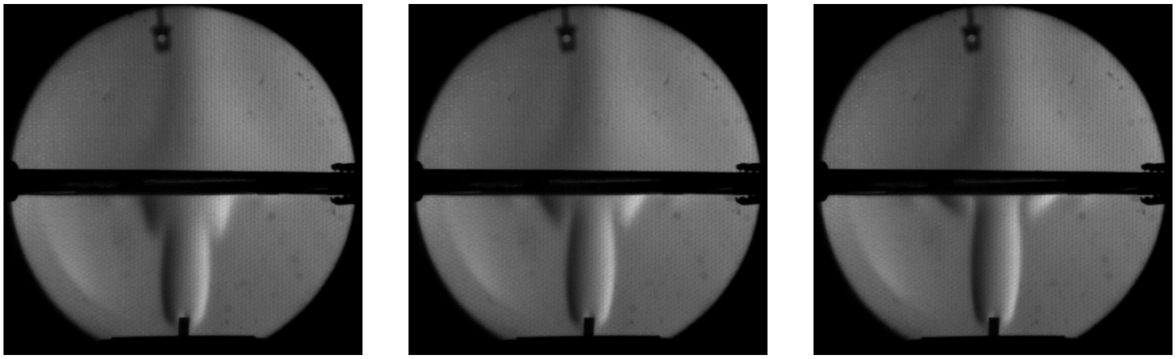

(g) 30 ms (h) 35 ms (i) 40 ms

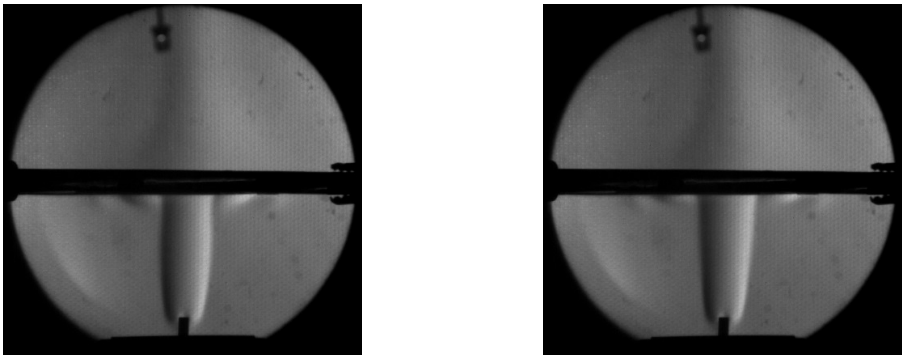

(j) 45 ms (k) 50 ms

Figure 5.4: Transient schlieren video: 1.25 kV/cm step, 3.5 cm electrode spacing, 27 mL/min.

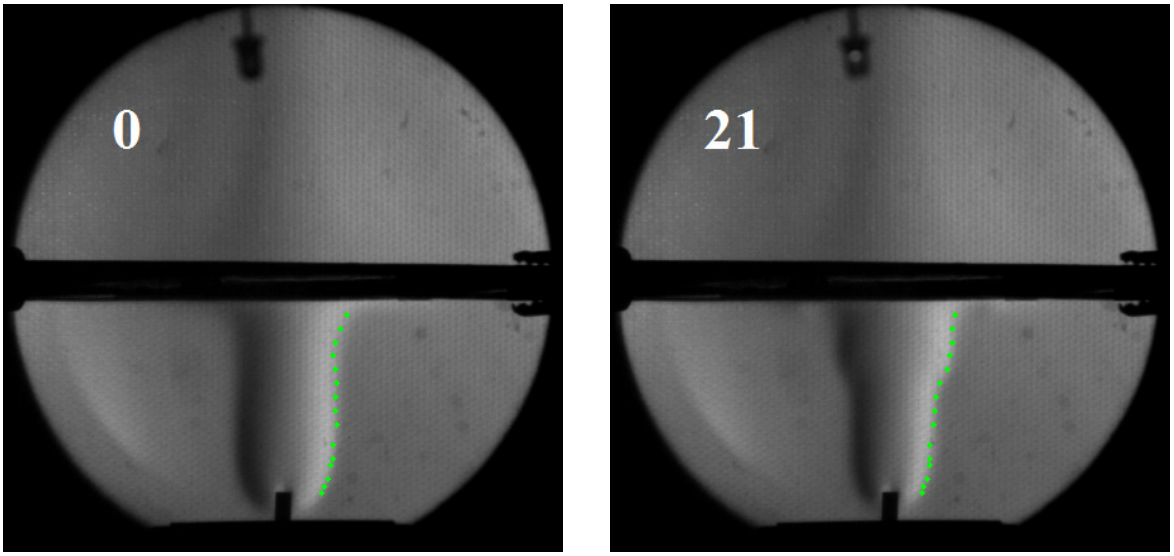

(a) 0 ms (b) 21 ms

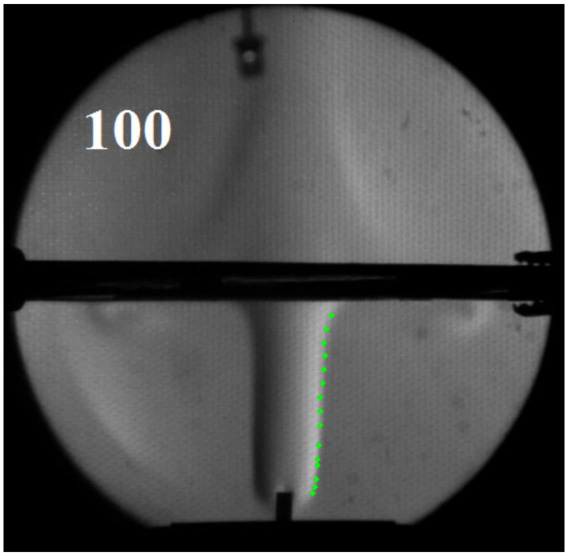

(c) 100 ms

Figure 5.5: Sample images showing thermal column radius markers. 1.25 kV/cm step, 3.5 cm electrode spacing, 27 mL/min.

A MATLAB script was created to analyze the radius of the thermal plume at different heights over time to measure the speed of the envelope wave. The radius was found by locating the peak gradient of the light intensity. The results of this is demonstrated in Fig. 5.5 where the green markers are the boundary layer radial locations found by the MATLAB script. Three snapshots from the video are shown to demonstrate the before, during and after effect of a

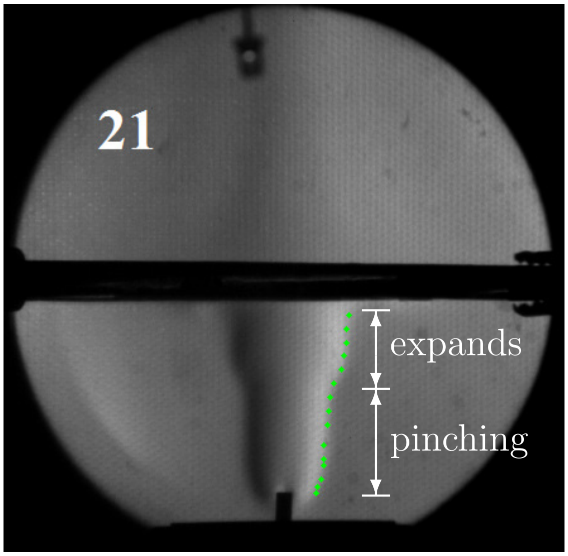

Figure 5.6: Description of observed thermal plume wave.

step voltage on the thermal plume radius. The radius of the thermal plume is seen to be significantly thinner after the field is turned on.

Within the lower region of the thermal plume at a given height the plume radius experiences a pinching motion (decrease in radius) as the thermal plume wave reaches that location. In the upper region, however, the thermal plume experiences and initial expansion of the radius at a given height followed by a decrease in radius. Fig. 5.6 shows a snapshot of the thermal plume wave in transition and highlights the difference between these upper and lower regions.

The location of the wave was determined by the instant that the thermal plume's radius experienced either a drop in radius (for the lower region) or an initial increase in radius (upper regions). These points in time were stored along with the respective axial position where they were observed. The slope of the curve produced when plotting the axial height vs point in time is defined as the velocity of the thermal wave, V_{wave}. This procedure was followed with several field strengths and 2 different mesh heights. Fig. 5.7 shows the results of the analysis. The thermal plume wave velocities imply that the enhanced convection is on the order of a few meters per seconds (2-7 m/s). This is compared to a cold flow velocity

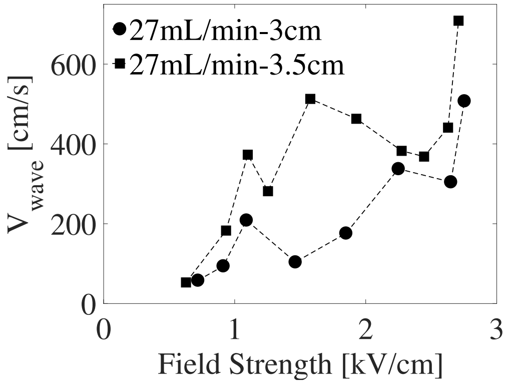

Figure 5.7: Thermal plume wave velocity

of 13 cm/s for the same mass flow rate and an expected buoyancy driven velocity less than 1 m/s. It is clear, therefore, that the ion driven wind enhances the body force convection in these flames.

5.5 Steady Schlieren Images

The initial wave formed by the ion wind was found to propagate through the inter-electrode space within ∼50 ms of the time the electric field was initiated. This was shown in Fig. 5.4. However, 1 or 2 much weaker thermal plume waves follow the initial wave so that the final state of of the thermal plume was achieved at ∼ 90-110 ms after the field is applied. Fig. 5.8 shows the final steady state location of the schlieren image boundary as a function of electric field strength. The values shown in this figure were taken from the schlieren videos for frames where t > 100 ms after the field is turned on. Therefore, for each height in each field strength, several markers are plotted over each other to show the variance in the schlieren radius as calculated by the MATALB program. The results show that the schlieren radius decreases from ∼7-8 mm without a field to ∼4-5 mm with a field present. The thinner thermal boundary layer can be explained by an electric field forced enhancement to the radially-inward and upwards convection. Further investigation and evaluation of this phenomenon will be made with the numerical simulations in Ch. 6.

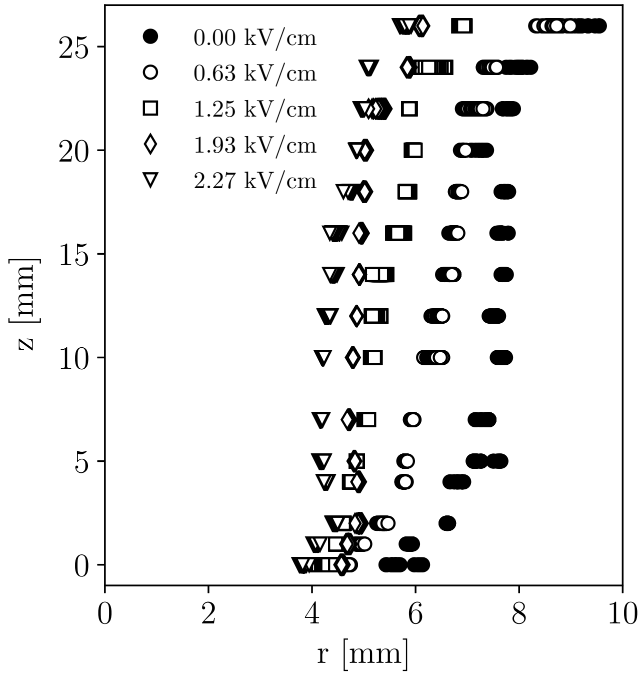

Figure 5.8: Schlieren boundaries: H = 3.5 cm - 27 mL/min.

5.6 Concluding Remarks

In order to study how ion winds are able to manipulate flame dynamics, a method of studying how ion winds manipulate the gaseous flow field is needed. Schlieren was the method of choice to observe the flow field reacting to an external electric field. Schlieren imagery was used to capture the transient motion of a non-premixed flame's thermal plume reacting to an instantaneous step voltage change, using a high-speed camera. A thermal plume wave was observed and a wave velocity on the order of 2-7 m/s was measured. The cause of the wave is enhanced convection due to ion-wind body forces. The magnitude of the velocity is an indicator of the strength of the ion wind. While further investigation is still needed to determine what type of local gas velocity is needed to produce such wave velocities, the wave velocity represents the order of magnitude of the gas velocity. Thus, the ion wind enhanced gas is seen to accelerate significantly (at least at the order of buoyancy) for the low gas nozzle velocities tested in this study. However, this ion wind acceleration will almost certainly be ineffectively small for more practical, large-scale velocities since buoyancy forces and fuel nozzle velocities will dominate over the ion winds. Applications of using external electric fields on combustion for manipulation via ion winds are, therefore, more suitable for low Reynolds number flows or in low Reynolds number regions of more robust flows.

Final steady schlieren images were also studied in Sec. 5.5. A thinning of the thermal boundary layer by several millimeters was observed for field strengths on the order of 1-2 kV/cm. This boundary layer thinning is also the result of enhanced upward convection due to ion wind body forces.

Chapter 6

Numerical Model

6.1 Numerical Introduction

In order to study further how electric fields may produce modifications to the flame's geometry and flow field that were observed in the previous chapters, a numerical simulation is useful to help capture the underlying physics. The experimental results shown previously imply that the primary effect is caused by an ion wind. The resulting change to the flow field causes enhancement to other mechanisms important to the non-premixed flame, including the location of the flame's position and intensity.

Only a handful of numerical work on electric field effects on axially symmetric non-premixed flames have been published, for example, by Hu et al. [2000], Papac and Dunn-Rankin [2007], Yamashita et al. [2009] and Belhi et al. [2010]. While the description of the numerical work in this dissertation will focus on creating the foundation for a reliable non-premixed axially symmetric flame, the primary objective is to build an extension of those previous studies by accurately predicting flame geometry, chemiluminescence intensity, flow field changes and how all of these can be manipulated by body forces.

This chapter will not show simulations involving Maxwell's equations or chemi-ions as this is an area of active research well beyond the scope of this dissertation. What will be shown is the method for creating and validating how complex components (boundary conditions, chemical mechanisms, external forces, etc...) will affect the numerical predictions. Even though Maxwell's equations will not be calculated, the results of these simulations will aid in creating a greater understanding of how a complex combustion system could produce the experimental observations ($CH*$ chemiluminescence, schlieren images, etc...).

6.2 Numerical Description

6.2.1 Mesh Description

The simulation shown here utilized the framework of an open-source software; OpenFOAM (Weller et al. [1998]). A three dimensional mesh was created in OpenFOAM. The mesh is a long wedge with a 5° angle representing a slice of a cylinder where the tip of the wedge is the axis of symmetry (see Fig 6.1). Although this mesh contains points in three dimensions, any radial effects are neglected and the system is only evaluated in the r and z directions making it two-dimensional.

Fig. 6.2 shows more details of the mesh represented only in the r and z directions. The bottom left corner of Fig. 6.2 shows two solid black lines representing the outline of the fuel tube (same as the cut corner of Fig. 6.1). A dashed vertical line can also be seen next to these solid lines that represents the inner diameter of the fuel tube. The medium that is being evaluated was split into 15 regions, which are separated by small dashed lines and can be identified by the roman numerals (i-iv) and lower case alphabet (a-d) grid system. In anticipation that the simulation results will produce a flame resembling the experimental results, it was expected that the flame will sit in regions ib, iib, and iia. The highest resolution

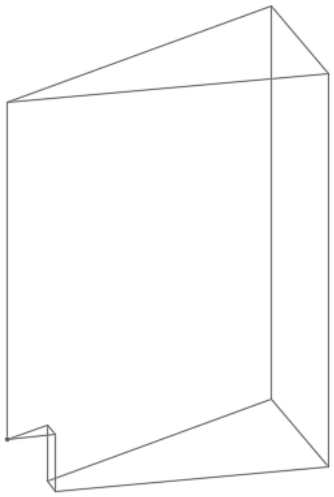

Figure 6.1: OpenFOAM mesh description.

was chosen in this region. The regions outside of these three become progressively coarse in order to reduce the computational time. The distance between points in regions ib, iib, and iia is 33 microns in the r and z directions each. This was chosen because the resolution of the camera used in Ch. 4 was measured to be 17±1 microns (in both directions) and found to produce well spatially resolved flame contours. However, the computational time with a mesh with 17 microns within a region as large as what is needed from these simulations is excessive. A grid dependency test of the simulation also showed little difference with the slightly coarser mesh. The experimental results found in Ch. 4 the CH^* contours with a thicknesses on the order of 1/10th of a millimeter. A pixel-to-pixel distance of 33 microns was, therefore, acceptable. Further details of the mesh can be found in Table 6.1.

6.2.2 Governing Equations

The region within the mesh is simulated as a multi-component gaseous mixture. This section shows the governing equations that are discretized and solved in the OpenFOAM simulation.

Eq. (6.1) is the ideal gas law for a mixture based on a mass fraction weighted molecular

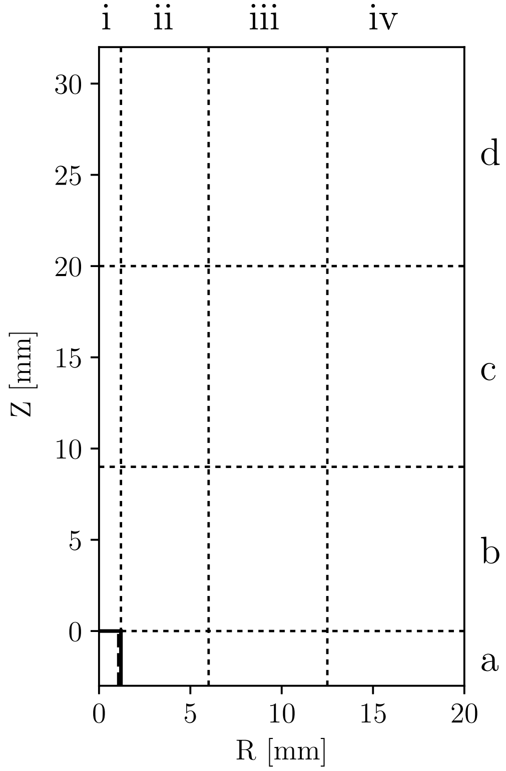

Figure 6.2: OpenFOAM mesh description.

weight (Eq. (6.2).

$$\rho = \frac{pM_{avg}}{RT} \tag{6.1}$$

$$M_{avg} = \frac{1}{\sum_{k=1}^{N} \frac{Y_k}{M_k}} \tag{6.2}$$

Eq. (6.3) is the mass conservation equation.

$$\frac{\partial \rho}{\partial t} + \frac{\partial \rho u_i}{\partial x_i} = 0 \tag{6.3}$$

Eqs. (6.4) and (6.5) are the momentum conservation equation and the shear stress tensor, respectively.

$$\frac{\partial \rho u_j}{\partial t} + \frac{\partial \rho u_i u_j}{\partial x_i} = -\frac{\partial p}{\partial x_j} + \frac{\partial \tau_{ij}}{\partial x_i} + \rho \sum_{k=1}^{N} Y_k f_{k,j} \tag{6.4}$$

$$\tau_{ij} = -\frac{2}{3}\mu_{mix}\frac{\partial u_k}{\partial x_k}\delta_{ij} + \mu_{mix}\left(\frac{\partial u_i}{\partial x_j} + \frac{\partial u_j}{\partial x_i}\right) \tag{6.5}$$

Table 6.1: Meshgrid details

region	Δx	Δz	r range	z range
i	0.033 mm	-	00.0 - 01.2 mm	-
ii	0.033 mm	-	01.2 - 06.0 mm	-
iii	0.083 mm	-	06.0 - 12.5 mm	-
iv	0.150 mm	-	12.5 - 20.0 mm	-
a	-	0.033 mm	-	-3.0 - 00.0 mm
b	-	0.033 mm	-	00.0 - 09.0 mm
c	-	0.150 mm	-	09.0 - 20.0 mm
d	-	0.300 mm	-	20.0 - 32.0 mm

The dynamic viscosity, μ, is calculated through Sutherland's Law shown in Eq. (6.6) where A_s and T_s are empirical constants. To find these constants, μ_k was calculated using Cantera (Goodwin et al. [2017]) for a homogeneous gas of each individual species k in the reaction mechanism using Lennard-Jones parameters. More details on the Lennard-Jones parameters will be provided in the following sections. μ_k is calculated as a function of temperature and fitted to Eq. (6.6). A_s and T_s for each species k were found to have a coefficient of determination value, R^2, with the Cantera derived viscosities within the range of 99.77 to 99.99%. Further details on the evaluation of the curve fitting can be found in Appendix C.1. The constants were stored and implemented in OpenFoam where the dynamic viscosity of the mixture, μ_{mix}, is calculated by taking an average of each μ_k weighted by the mass fractions of each species k: Eq. (6.7). This method of using Cantera to derive A_s and T_s values for individual species significantly enhanced OpenFOAM's base line performance, which otherwise uses transport properties of air.

$$\mu = \frac{A_s\sqrt{T}}{1 + T_s/T} \tag{6.6}$$

$$\mu_{mix} = \sum_{k=1}^{N} \mu_k(T)Y_k \tag{6.7}$$

The last term in Eq. (6.4) is the general representation of external body forces applied to the gas volume. Buoyancy is one example of a body force where $f_z = -g$ and the full term is equal to $-\rho g$. However, this general term for body forces can also be used to represent electrical body forces due to ion currents,

$$\begin{aligned}\rho \sum_{k=1}^{N} Y_k f_{k,j} &= \rho \sum_{k=1}^{N} Y_k \frac{q S_k E_j N_A}{M_k} \\ &= \rho \sum_{k=1}^{N} n_k q S_k E_j. \end{aligned} \tag{6.8}$$

S_k is either $+1$, -1 , or 0 for positive ions, electrons/negative ions and neutral species, respectively. $q = 1.60217 \times 10^{-19}$ Coulombs is the charge of an electron. E_j is the electric field strength in the direction j. M_k and n_k are the molecular weight and number density, respectively, of species k. $N_A = 6.022 \times 10^{23}$ mol^{-1} is Avogrado's number.

Eq. (6.9) is the species conservation equation for species k. $\dot{\omega}_k$ is a source term representing the total reaction rate for species k. The molecular diffusion is simplified by using a mixture diffusion coefficient, D_{mix}, for each species equation. D_{mix} was calculated through multiple means: unity Lewis number, unity Schmidt number (default OpenFOAM option), and Schmidt number equal to 0.7. However, the best results were found to be produced by a constant Schmidt number equal to 0.7. The Schmidt number, Sc, is shown in Eq. (6.10). Further evaluation on the use of these dimensionless numbers can be found in Appendix C.2.

$$\frac{\partial \rho Y_k}{\partial t} + \frac{\partial \rho u_i Y_k}{\partial x_i} - \frac{\partial}{\partial x_i}\left(\rho D_k \frac{\partial Y_k}{\partial x_i}\right) = \dot{\omega}_k \tag{6.9}$$

$$Sc_{mix} = \frac{\mu_{mix}}{\rho D_{mix}} \tag{6.10}$$

$\dot{\omega}_k$ is the total reaction rate of species k and is equal to the sum of all reaction rates associated with species k's production or destruction.

$$\dot{\omega}_k = \sum_{i=1}^{N_{k-rxns}} \dot{\omega}_{k,i} \tag{6.11}$$

N_{k-rxns} is the number of forward and backwards reactions associated with species k and $\dot{\omega}_{k,i}$ is the reaction rate of reaction i for species k. The rate constant, $\kappa_{k,i}$, associated with $\dot{\omega}_{k,i}$ takes an Arrhenius form.

The enthalpy form of the energy conservation equation, Eq. (6.12), is solved. K is the kinetic energy and defined in Eq. (6.13).

$$\frac{\partial \rho h}{\partial t} + \frac{\partial \rho u_i h}{\partial x_i} + \frac{\partial \rho K}{\partial t} + \frac{\partial \rho u_i K}{\partial x_i} - \frac{\partial p}{\partial t} - \frac{\partial}{\partial x_i}\left(\alpha_{mix}\frac{\partial h}{\partial x_i}\right) = \dot{\omega}_T \tag{6.12}$$

$$K = \frac{1}{2}u_i u_i \tag{6.13}$$

$\dot{\omega}_T$ has the relationship with $\dot{\omega}_k$ by Eq. (6.14).

$$\dot{\omega}_T = \sum_{k=1}^{N} h_k \dot{\omega}_k. \tag{6.14}$$

The thermal diffusivity, α_{mix}, is the ratio of the thermal conductivity, λ, and the product of density and heat capacity at constant pressure, c_p. This is shown in Eq. (6.15).

$$\alpha_{mix} = \left(\frac{\lambda}{\rho c_p}\right)_{mix} \tag{6.15}$$

Similar to the dynamic viscosity, λ and c_p were calculated for each individual species and a mass weighted averaged value was used for the mixture. $c_{p,k}$ was calculated for each species k by using Joint-Army-Navy-Air Force (Janaf) thermodynamic tables containing empirical coefficients that are used to calculate $c_{p,k}$ via Eq. (6.16). The Janaf tables will be described in detail in later sections. $c_{v,k}$ is calculated by assuming an ideal gas ($c_{v,k} = c_{p,k} - R$). The thermal conductivity is calculated using the modified Eucken formula shown in Eq. (6.17). Eqs. (6.18), (6.19), and (6.20) are the equations used to solve for the mixture values of c_p,

c_v, and λ, respectively.

$$\frac{c_{p,k}}{R} = ((((a_4T + a_3)T + a_2)T + a_1)T + a_0); \tag{6.16}$$

$$\lambda_k = \mu_k c_{v,k}(1.32 + 1.77\frac{R}{c_{v,k}}) \tag{6.17}$$

$$c_{p,mix} = \sum_{k=1}^{N} c_{p,k}(T)Y_k \tag{6.18}$$

$$c_{v,mix} = \sum_{k=1}^{N} c_{v,k}(T)Y_k \tag{6.19}$$

$$\lambda_{mix} = \sum_{k=1}^{N} \lambda_k(T)Y_k \tag{6.20}$$

Similar to Eq. (6.16), the Janaf tables are also used to evaluate the enthalpy and entropy of species k. This is shown in Eqs. (6.21) and (6.22), respectively.

$$\frac{h_k}{R} = \left(\left(\left(\left(\frac{a_4}{5}T + \frac{a_3}{4}\right)T + \frac{a_2}{3}\right)T + \frac{a_1}{2}\right)T + a_0\right)T + a_5; \tag{6.21}$$

$$\frac{s_k}{R} = \left(\left(\left(\frac{a_4}{4}T + \frac{a_3}{3}\right)T + \frac{a_2}{2}\right)T + a_1\right)T + a_0 lnT + a_6; \tag{6.22}$$

6.2.3 Chemical Mechanism and Thermo-transport

Gri 3.0 from Smith et al. [1999] was used as the base mechanism for all neutral molecules and their reactions. The files containing the reaction parameters, transport properties and thermodynamic properties can be found from *http://combustion.berkeley.edu/gri-mech/*.

A brief review of the history of CH^* chemiluminescence was given in Sec. 4.2. Detailed studies were performed on the validation of various chemiluminescence mechanisms by Panoutsos et al. [2009] and Kathrotia [2011]. The reaction parameters for excited species CH^* were borrowed from Walsh [2000] and Hall et al. [2005]. Separate simulations were performed with both chemiluminescence mechanisms for comparison, however, Walsh [2000] was used as the baseline mechanism.

6.2.4 Boundary Conditions

The boundary conditions were set to mimic the experimental conditions described in the previous chapters. A summary of important boundary conditions is shown in Table 6.2. Pure methane is supplied at the fuel tube exit boundary (b.c. # 1). The rest of the mesh volume is initialized to contain pure air.

Table 6.2: Mesh boundary conditions (b.c.)

b.c. #	boundary name	location	position	velocity b.c.	temperature b.c
1	fuel tube exit	ib	bottom	see *	constant T **
2	co-flow air exit	iia - iiia	bottom	0 cm/s	constant 300 K
3	far co-flow surface	iva	bottom	no slip	constant 300 K
4	fuel tube wall	iia	left	no slip	constant T **
5	mesh electrode	id - ivd	top	zero gradient	zero gradient
6	radial mesh extent	iva - ivd	right	zero gradient	zero gradient

*U_z: uniform value (Eq. (6.23)) or nonuniform profile (Eq. (6.24))
**varies between 300-500 K

Initially, the temperature of the fuel tube exit and fuel tube wall (b.c. # 1 and 4) are set to 800 K for several milliseconds to allow the fuel and air to mix and heat up to the ignition point. After a flame is established, the thermal b.c. # 1 and 4 are relaxed to more realistic temperatures. It was found that the predicted standoff distance of the bottom of the flame to the burner fuel tip depends on the thermal b.c. # 1 and 4. Since this a region of high interest, several temperatures were tested (300 - 500 K) in order to evaluate this dependence.

The velocity of the fuel exiting the burner tube (b.c. # 1) was also examined. Two different types of profiles were tested: a uniform value (Eq. (6.23)) or a non-uniform profile (Eq. (6.24)), where $\dot{Q}_f$ is the average volumetric flow rate and R is the inner radius of the fuel tube. In the experimental work, the volumetric flowrate given in each result was the reading set at the rotameters by the user. Because the temperature boundary conditions described in the simulations vary from 300 K to 500 K, $\dot{Q}_f$ was calculated from a constant mass flow rate of CH_4 (between the rotameter and the fuel tube exit) with a temperature dependent density.

$$V(r) = \frac{\dot{Q}_f}{\pi R^2} \tag{6.23}$$

$$V(r) = \frac{2\dot{Q}_f}{\pi R^2}\left(1 - \left(\frac{r}{R}\right)^2\right) \tag{6.24}$$

Fig. 6.3 shows the difference between two similar cases but with the two different fuel velocity boundary conditions of Eqs. (6.23) and (6.24). The differences found are subtle. The non-uniform velocity profile (Fig, 6.3a) produces slightly higher peak mole fraction of CH^*. It also produces a stronger CH^* mole fraction near the base of the flame compared to the results of the uniform velocity (Fig. 6.3b) case. This happens because the non-uniform profile has a higher velocity close to the center but a zero velocity near fuel tube radius. The residence time of the gas near the fuel tube wall would be longer compared to the uniform velocity case which would allow more time for the fuel to diffuse radially. The non-uniform velocity profile also produces a very slightly lower flame height compared to the uniform velocity profile. Fig. 6.4 shows the same two simulations zoomed in near the flame base. The non-uniform velocity profile produces a more rounded flame edge that flares slightly outward compared to the uniform velocity case.

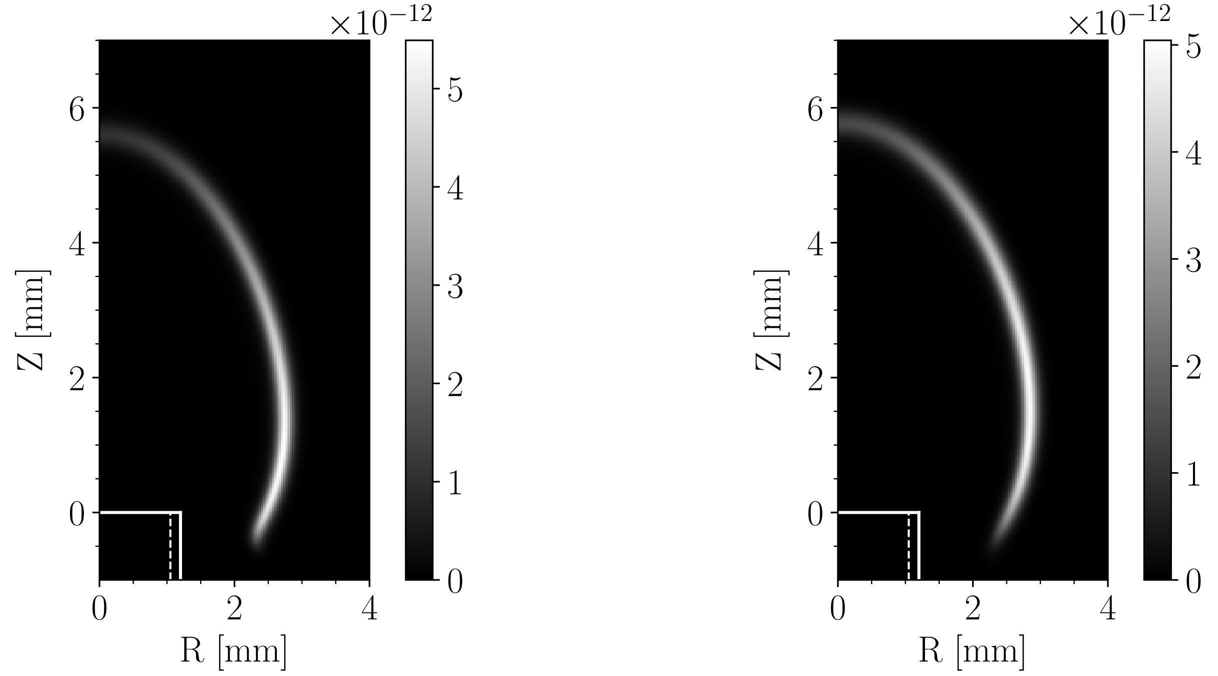

(a) Non-uniform velocity b.c.

(b) Uniform velocity b.c.

Figure 6.3: Effects of fuel velocity boundary conditions on CH^* mole fractions (numerical). $T_{b.c.} = 300$ K.

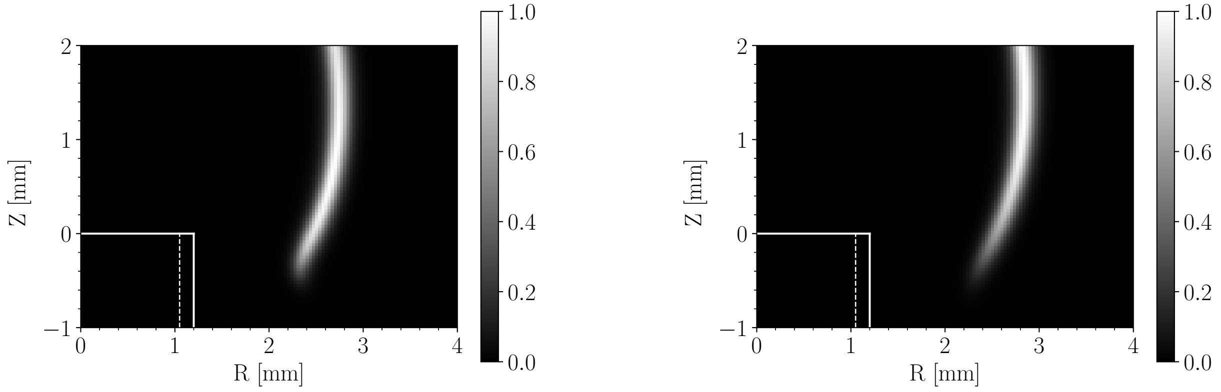

(a) Non-uniform velocity b.c.

(b) Uniform velocity b.c.

Figure 6.4: Effects of fuel velocity boundary conditions on CH^* flame base shape (numerical). $T_{b.c.} = 300$ K.

6.3 Numerical Validation

6.3.1 Temperature

Fig. 6.5 shows the temperature profiles predicted by the simulations. The differences between the non-uniform and the uniform velocity profiles are again very subtle. Perhaps the only real difference is that a non-uniform velocity profile produces a slightly higher profile near the burner tube wall. A 40 K temperature difference is found between the two simulations where the uniform velocity profile produces the hotter flames. The peak temperatures found in these simulations were 1963 K and 2000 K which are both reasonable temperature predictions for these flames.

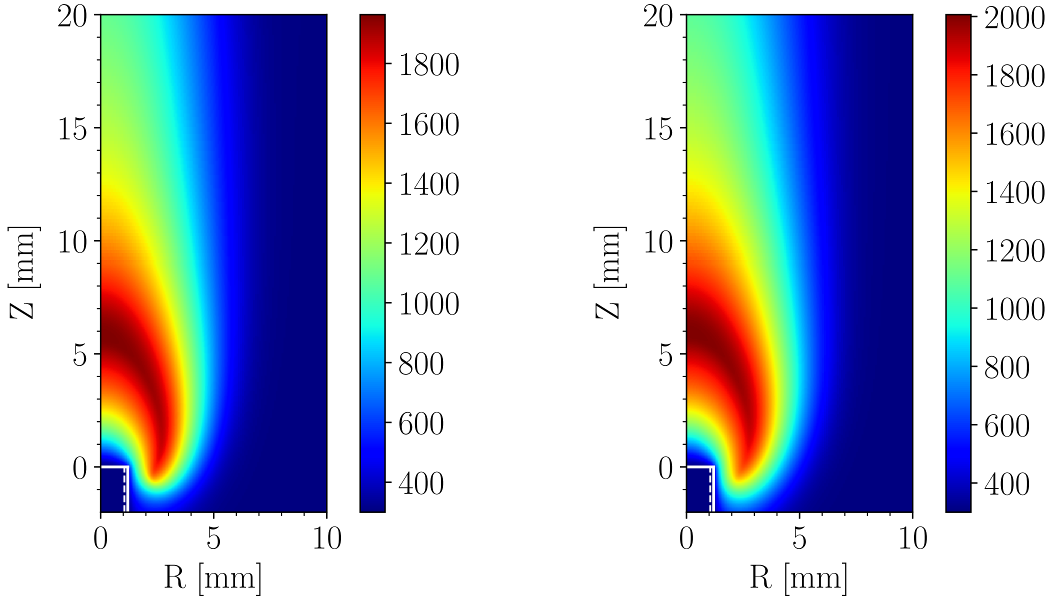

(a) Non-uniform velocity b.c. (numerical) T_{max} = 1963 K.

(b) Uniform velocity b.c. (numerical) T_{max} = 2006 K.

Figure 6.5: Temperature results

6.3.2 CH^*

The peak CH^* mole fractions calculated from the simulations of Fig. 6.3 were on the order of 5e-12. This is about 1 order of magnitude lower than the peak mole fractions experimentally obtained and computed by Walsh et al. [1998] and Walsh [2000]. The primary difference between the results shown here and the results from Walsh et al. [1998] and Walsh [2000] is the velocity conditions being used. The fuel flow velocities in this study are much lower and produce "attached" flames, whereas, the higher flow velocities of Walsh [2000] produce lifted flames. The peak mole fraction of CH^* in the lifted flames is near the flame edge where premixing is occurring much more efficiently than for the "attached" flames. Therefore, the CH^* mole fractions shown in this study are reasonable.

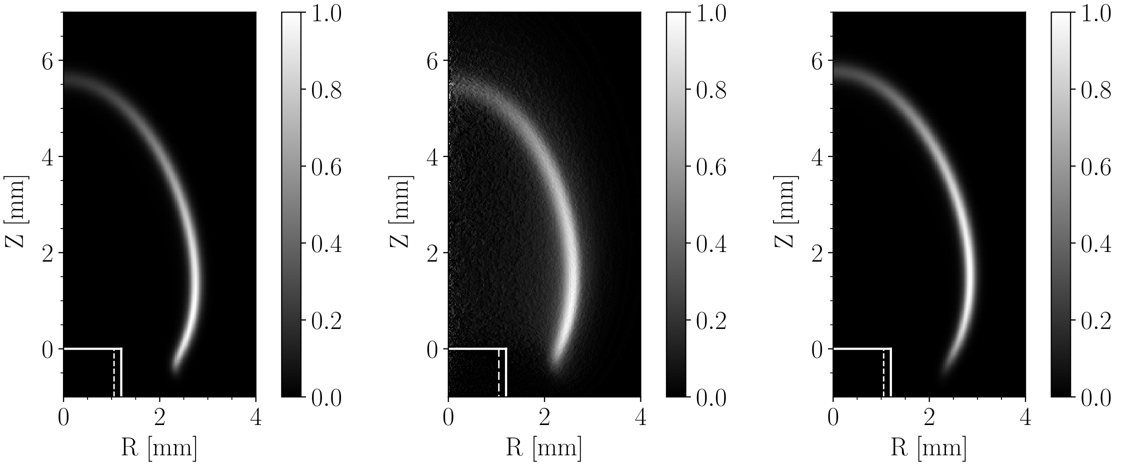

(a) Non-uniform velocity b.c. (numerical).

(b) Experimental

(c) Uniform velocity b.c. (numerical).

Figure 6.6: CH^* chemiluminescence flame comparison: 1g gravity field, no external electric field, coflow with a protruding tube, and 27mL/min fuel flow rate. Figs. 6.6a and 6.6c have a scale of mole fraction normalized by the peak value. Fig. 6.6b has a scale of pixel intensity normalized by the maximum pixel value.

A qualitative comparison between the simulated prediction of CH^* and the experimentally obtained results is shown in Fig. 6.6. In this figure, the mole fractions and pixel intensity are normalized by their respective peak value to aid in examining their spatial similarity.

In both cases, the numerically predicted CH^* profiles match well with the experimentally obtained profile. However, the non-uniform velocity profile (Fig. 6.6a) shows a better spatial match, qualitatively. Specifically, the flame heights match better between the non-uniform velocity simulation and the experimentally obtained flame (Fig. 6.6b) compared to the uniform velocity simulation (Fig. 6.6c). Also, the shape of the flame base-edge produced by the non-uniform velocity profile simulation matches qualitatively better with the experimental flame base-edge. In both simulated cases, the calculated flames sheets are thinner than the experimentally obtained flame sheets. Walsh et al. [2000] studied the effects of optics geometry (particularly the effect of f-number) on the Abel inversion results. Giassi [2017] expanded on this study and also showed the effect of other excited species that could potentially emit light within the range of the light filters. Both cases, optics geometry and unknown chemiluminescence, result in broader flame thicknesses. As stated in Ch. 4, a reasonable f-number of 5.6 and a narrow band filter (10 nm full width at half max) centered at 431 nm were chosen to minimize these effects. However, their contribution in the uncertainty of the experimental flame thicknesses should be noted.

Fig. 6.7 shows the position of various contour levels super-imposed on the normalized mole fraction profile for the simulation using a non-uniform velocity profiles. Fig. 6.7a appears to best represent the entire profile, while Figs. 6.7b and 6.7c appear close representations. Fig. 6.7d appears to be the poorest, especially for representing the flame height. However, the shape of the flame's base is well captured by the 40% contour. The 40% contours will be used for comparison with the experimental results since it reliably matches best the experimental chemiluminescence images.

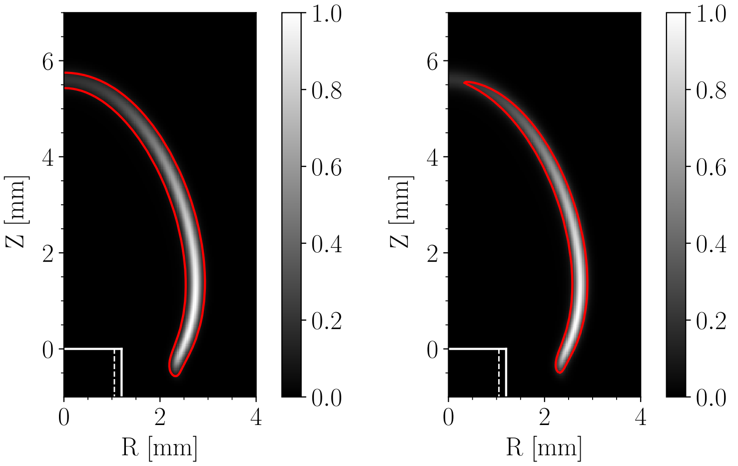

(a) 10% contour.

(b) 20% contour.

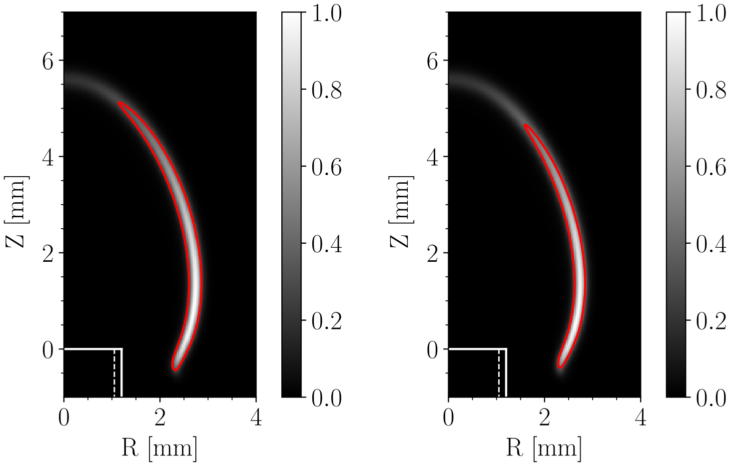

(c) 30% contour.

(d) 40% contour.

Figure 6.7: Comparison of CH^* contour levels (numerical).

6.3.3 Stoichiometric Mixture Fraction

A brief review of the simplified non-premixed conical-type flame models, e.g., Burke and Schumann [1948] and Roper [1977] was given in Sec. 4.1. More details can be found in Ch. 7 where these models are extended by considering the electric field body force acceleration as a generalized influence on flow changes in these flames. The beauty of these theoretical models is the accuracy they can achieve even with the level of simplicity of their infinitely fast chemical kinetics. This is made possible by the reduction of the mass conservation equations of fuel and oxidizer into a single equation formulated by the mixture fraction. The mixture fraction is defined in Eq. (6.25).

$$C = \frac{f - f_2}{f_1 - f_2} \tag{6.25}$$

where, $f = nX_F - X_O$, f_1 is the condition of f_1 in the fuel tube of the burner, and f_2 is the condition of f in ambient air. n is the number of moles of O_2 it would take to react stoichiometrically with fuel. X_F and X_O are the mole fractions of fuel and oxidizer, respectfully. In the case of methane, n equals 2 according to Eq. (6.26).

$$CH_4 + 2O_2 = CO_2 + 2H_2O \tag{6.26}$$

According to the aforementioned studies, the flame sheet would lie along the surface where fuel and oxidizer are in stoichiometric proportion ($C = C_{st}$). It is found for methane reacting with air that C_{st}=0.095.

Here, C_{st} is tested with the numerical model to examine how well it matches with the visual marking considered to be the flame. CH^* is the most logical marker for the reaction zone since it is what can most easily be seen (in most flame applications) by the human eye. Therefore, it makes sense to compare C_{st} with the CH^* mole fraction profile. This is shown in Fig. 6.8. The CH^* profile is found to lie just outside of the C_{st} line (on the oxidizer side). The C_{st} line stands about 0.1 to 0.2 mm from the peak mole fraction along the CH^* curve. This is true everywhere except at the upstream leading edge of the flame. The edge of the flame diverges from the C_{st} line because the C_{st} is a property of non-premixed flames. Even though conical co-flow flames are considered non-premixed, the flame's edge contains many premixed flame characteristics because of the higher level of mixing occurring in this region.

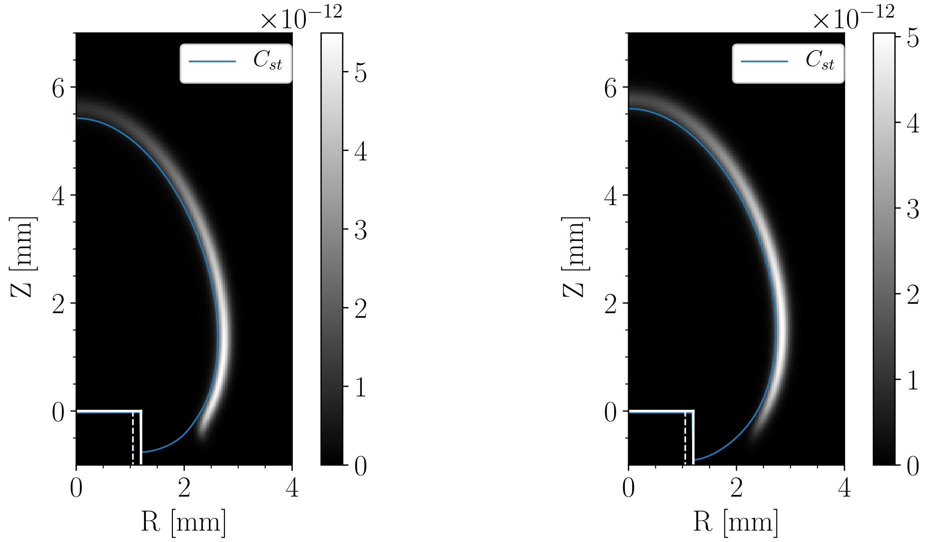

(a) Non-uniform velocity b.c. (numerical).

(b) Uniform velocity b.c. (numerical).

Figure 6.8: CH^* flame contour vs C_{st}.

The stoichiometric mixture fraction may not be a perfect marker for the CH^* profiles but the spatial off-set distance (1/10th mm) is small enough for the theoretical simplification to be justified with typical experimental spatial uncertainty.. Another test for the C_{st} line is to also compare it to the region of substantial local heat-release of the flame. This is shown in Fig. 6.9. Similar to the CH^* comparison, the local heat-release is on the oxidizer side of the C_{st} line. The offset distance between the line and the peak locations along the heat-release curve is again on the order of 1/10th of a millimeter.

6.4 Schlieren Prediction

6.4.1 Introduction

Ch. 5 revealed how the thermal boundary layer above a non-premixed co-flow flame responds to external electric fields and ion winds. Schlieren imagery is an age-old technique

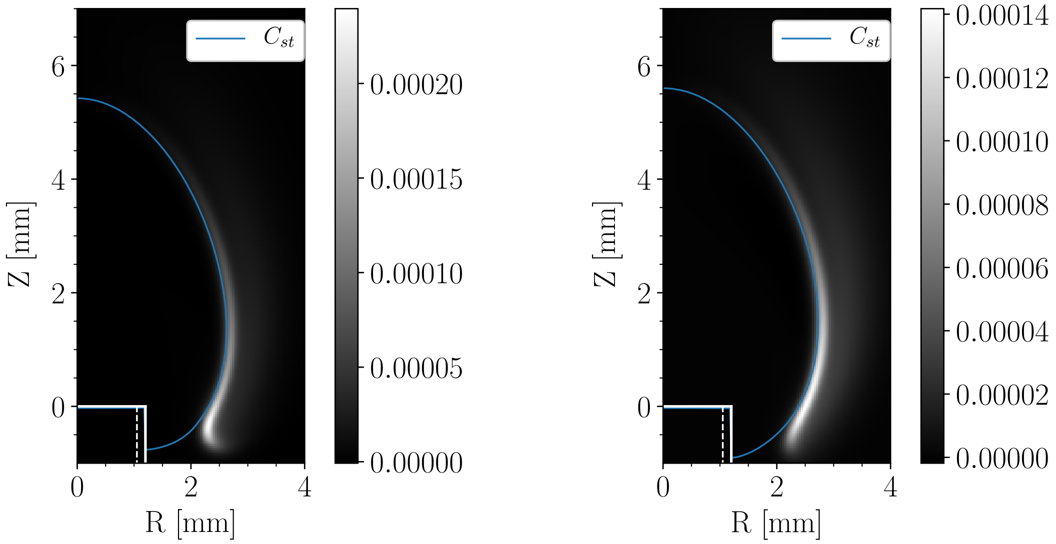

(a) Non-uniform velocity b.c. (numerical).

(b) Uniform velocity b.c. (numerical).

Figure 6.9: Local heat release $\dot{\omega}_T$ [J/m^3/s] vs C_{st}.

with applications in many scientific disciplines. However, the difficulty in using schlieren is determining how to make quantified measurements. For instance, a schlieren image can be used to determine the location of a shock-wave formed by an extremely fast moving object through a fluid but acquiring measurements of temperature or density from the schlieren image is much more difficult to achieve because it requires derivatives of potentially noisy signatures that then amplifies the noise. The schlieren experiments in Ch. 5 attempt to quantify the thermal flow environment under external electric fields. The location of the thermal boundary layer was found and the speed of an ion wind convected wave through that boundary layer was measured.

In this section, simple schlieren and light theory will be applied to the numerical prediction of an axially symmetric co-flow flame in order to provide another form of validation to the OpenFOAM simulation and to see a deeper understanding of what the experimental schlieren images could tell us about chemi-ion driven flows.

Referring to Eqs. (5.1) - (5.6) and following the procedure suggested by Dunn-Rankin and

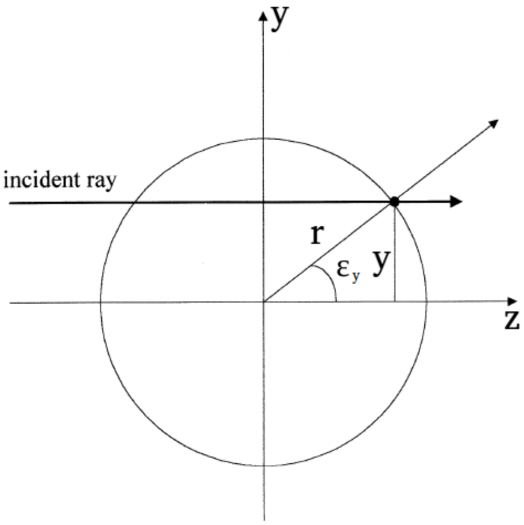

Figure 6.10: schlieren coordinate system diagram for an axially symmetric system.

Weinberg [1998], we begin by starting with Eq. (5.5).

$$\epsilon_y = -\frac{1}{n}\int \frac{\partial n}{\partial y}\partial z$$

The coordinate system is shown in Fig. 6.10. The z direction is the propagation direction of the collimated light. The origin formed by r and y is the central axis of the burner/flame. The y axis is perpendicular to the z direction.

Eq. (5.5) can be transformed by applying the definitions shown in Eq. (6.27).

$$n = f(r), \tag{6.27a}$$

$$\frac{\mathrm{d}n}{\mathrm{d}r} = f'(r), \tag{6.27b}$$

$$\frac{\mathrm{d}n}{\mathrm{d}y} = \frac{y}{r}f'(r), \tag{6.27c}$$

$$dz = \frac{r}{\sqrt{r^2+y^2}}dr \tag{6.27d}$$

The resulting equation is shown in Eq. (6.28).

$$\epsilon_y \sim -\frac{1}{f(r)} \int_y^\infty \frac{y}{\sqrt{r^2+y^2}} f'(r) dr \tag{6.28}$$

It was stated in Ch. 5 that $\delta = k\rho$ is very small ($\delta \sim O(10^{-4})$) for gases. Thus, $f(r) = n$ is approximately 1. $f'(r)$ can be expanded by Eq. (6.29).

$$\begin{aligned} f'(r) &= \\ &= \frac{\mathrm{d}}{\mathrm{d}r}\left(1 + k\rho\right) \\ &\sim \frac{\mathrm{d}}{\mathrm{d}r}\left(\frac{1}{T}\right) \\ &\sim -\frac{1}{T^2}\frac{\mathrm{d}T}{\mathrm{d}r} \end{aligned} \tag{6.29}$$

Combining Eq. (6.28) with Eq. (6.29), a convenient formula for ϵ_y can be found. This is shown in the Eq. (6.30).

$$\epsilon_y = constant \times \int_y^\infty \frac{y}{\sqrt{r^2+y^2}} \frac{1}{T^2}\frac{\mathrm{d}T}{\mathrm{d}r} dr. \tag{6.30}$$

Eq. (6.30) can then be discretized by applying the trapezoidal rule shown in Eq. (6.31).

$$\epsilon_y(y_i) \sim \sum_{j=i+1}^{N} \frac{F_{i,j-1} + F_{i,j}}{2}(r_j - r_{j-1}) \tag{6.31a}$$

$$F_{i,j} = \frac{y_i}{\sqrt{r_j^2 + y_i^2}} \frac{1}{T(r_j)^2} \frac{\mathrm{d}T(r_j)}{\mathrm{d}r} \tag{6.31b}$$

It is best to normalize ϵ_y, since the contrast of the experimental schlieren image could be increased or decreased by placing the knife edge further into or out of the focal point in order to increase or decrease the amount of deflected light blocked by the knife-edge. The results after applying Eq. (6.31) to the temperature results of the simulations are shown in Fig. 6.11. The color map of the figure is plotting ϵ_y normalized by the absolute maximum value of ϵ_y.

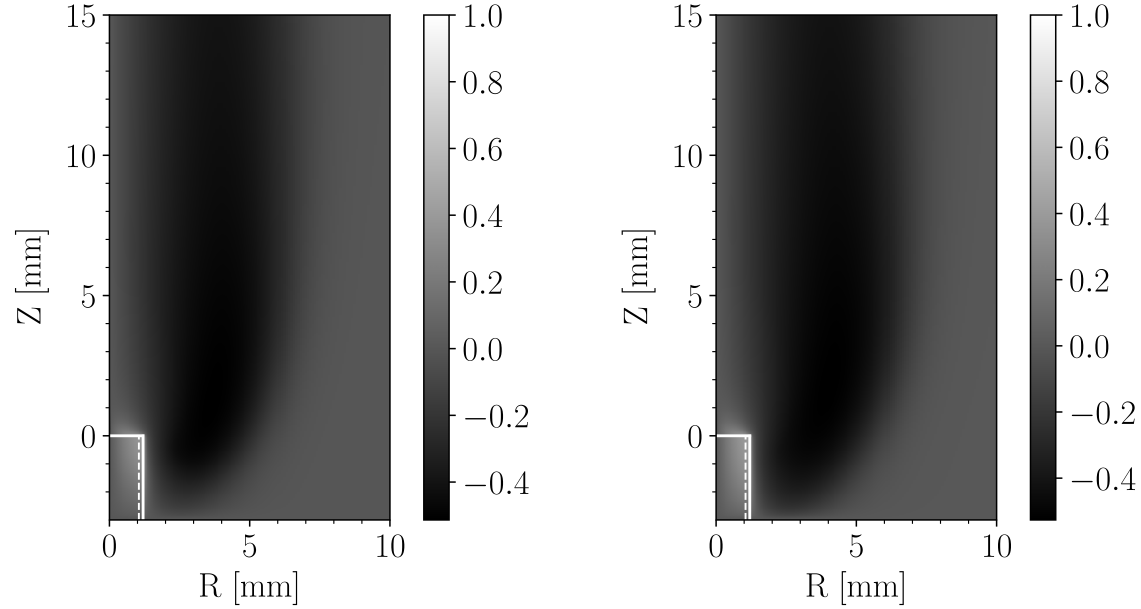

(a) Non-uniform velocity b.c.

(b) Uniform velocity b.c.

Figure 6.11: Simulation predicted schlieren images: ϵ_y normalized by the $|\epsilon_y|_{max}$

What appears on an experimental schlieren image is not directly ϵ_y. The experimental image is the background light created by the point source minus the portion of deflected light that is blocked by the knife-edge. This can be described by Eq. (6.32).

$$I = I_0 - A(\epsilon_y) \tag{6.32}$$

I is the illumination on the screen [energy/area/time], I_0 is the illumination on the screen if the density of the gas was uniform everywhere (i.e the background light intensity), and $A(\epsilon_y)$ is the portion of deflected light blocked by the knife-edge. The relationship betwee A and ϵ_y is unknown at this point.

Fig. 6.12a shows the normalized ϵ_y are various heights. These profiles can be compared to the experimentally obtained pixel intensity profiles from the schlieren images, an example of which can be seen in Fig. 6.12b. The pixel intensity profile shown in this figure was taken from the same frame shown in Fig. 5.5a. The pixel intensity profile is seen to be inversely symmetrical about the zero radius axis. This happens because the knife-edge only blocks light from one side while light is allowed through the other side.

The simulated schlieren profiles in Fig. 6.12a show good qualitative agreement with the experimental profile in Fig. 6.12b. The overall profiles appear to agree, however, the simulated peaks appear just under $r = 5$ mm while the experimental peak appears at just over $r = 5$ mm.

As a side note, the schlieren boundary radii shown in Fig. 5.8 were produced by determining the location of the peak gradient of pixel light intensity along a horizontal line such as the profiles in Fig. 6.12b. This was shown to be a reliable way of finding the radius of the schlieren image (see Fig. 5.5). This is because the pixel intensity profile has a very abrupt change in gradient at the schlieren edge. However, the simulated schlieren profiles in Fig. 6.12a have a much smoother gradient near the edge. Therefore, edge finding is much more difficult.

Finally, Fig. 6.13 overlays the experimental values of the schlieren boundary (taken from Fig. 5.8) onto the simulated normalized ϵ_y. Contour lines are also included in the image to compare the experimentally obtained schlieren boundary layer to the simulation schlieren results. The experimental schlieren boundary layer points lie within the 1% normalized ϵ_y contour line. The 5 and 10% contour lines are shown to be the best match with the exper-

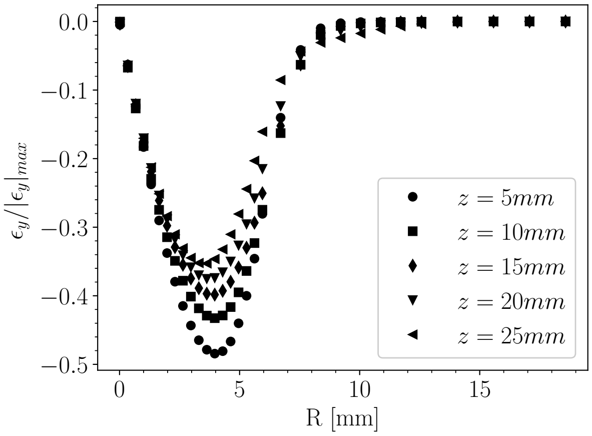

(a) Simulation predicted Normalized ϵ_y at various heights.

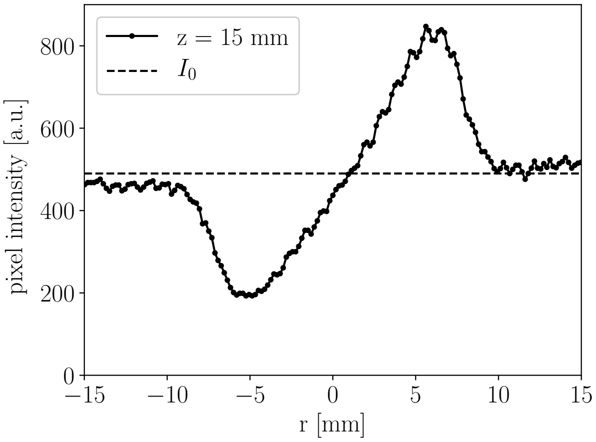

(b) Sample experimental schlieren pixel intensity profile across a horizontal line.

Figure 6.12: Comparison of computed vs experimental schlieren profiles.

imental data. This positive comparison between measurement and calculation is important because it confirms the reliable prediction of the thermal field around the flame (i.e., the broader convective transport) in addition to the appropriate location of the reaction zone.

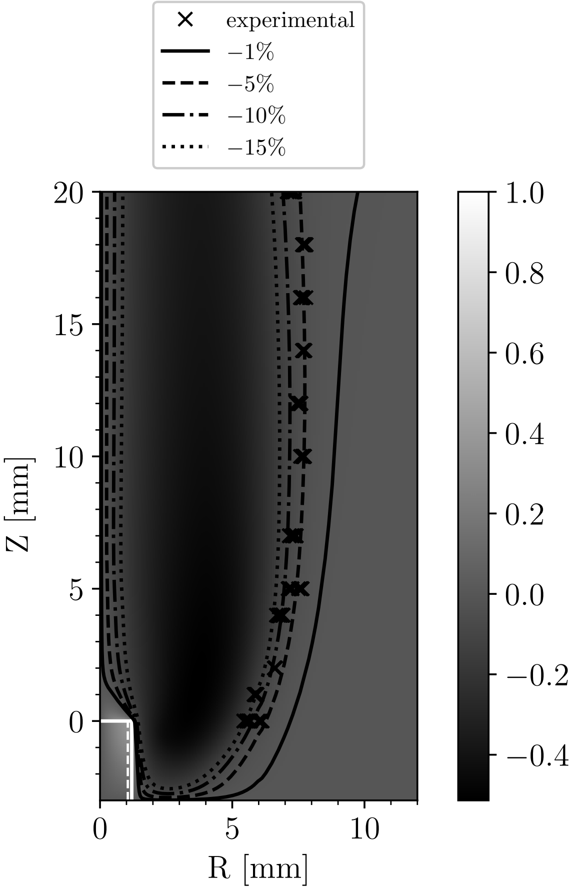

Figure 6.13: Comparison of normalized ϵ_y at various heights with experimentally obtained schlieren boundary (Fig. 5.8): 0 kV/cm.

6.5 Effect of Body Forces on Coflow Flames

6.5.1 Introduction

One major goal of this dissertation is to demonstrate if ion winds are enough to explain all of the observed changes to the flame and flow dynamics when an external field is applied to a non-premixed coflow flame, and if electronic effects on chemistry are negligible. Ideally, simulations of coflow flames with chemi-ion chemistry and Maxwell's equations would test this theory. A simpler test could be to generalize the ion wind body force into a more easily simulated body force. Buoyancy forces are readily implemented body forces in most reacting CFD simulations and so a generalized form of body force would be similarly straightforward to incorporate.

Many parallels have been made in previous studies between buoyancy forces and ion wind body forces; see, for example, Carleton and Weinberg [1987], Papac and Dunn-Rankin [2006], Dunn-Rankin and Weinberg [2006], Papac and Dunn-Rankin [2007], and Karnani [2011]. The simulations in Papac and Dunn-Rankin [2007] show that buoyancy forces and ion wind body forces cannot cancel each other completely since the temperature gradient profiles needed for buoyancy do not exactly match the location of ion currents needed to form ion wind forces. However, the micro-gravity drop tower experiments from Karnani et al. [2012] show that electric fields can be used to simulate buoyancy forces in environments where gravity is negligible.

Simulations were performed on testing the effect of enhanced gravity on various non-premixed coflow flame parameters, e.g. flame geometry, flame tip height, flame base-edge height, CH^* chemiluminescence, and schlieren profiles. While it cannot be expected that enhanced gravity will produce exactly what would be produced if chemi-ion chemistry and Maxwell's equations were employed, parallels can be drawn where applicable in order to assess the performance of enhanced body forces as the source of the observed flame/flow dynamics seen in the previous chapters.

6.5.2 Results

In this section, we will refer to Eq. (6.4) but replace the generalized form of body forces with ρg. g is the gravity level of the system and is equal to the $G = 9.81$ m/s^2 times a constant.

$$\frac{\partial \rho u_j}{\partial t} + \frac{\partial \rho u_i u_j}{\partial x_i} = -\frac{\partial p}{\partial x_j} + \frac{\partial \tau_{ij}}{\partial x_i} + \rho g \tag{6.33}$$

Fig. 6.14 shows the simulated prediction of CH^* mole fraction profiles under increasing levels of gravity. Qualitatively the effect of enhanced gravity produces what was found to happen when external electric fields are used in experiments. That is, the flame height decreases slightly, the radius of the flame decreases slightly, the base of the flame increases significantly, and the peak mole fraction increases with increasing gravity. The gravity level at which point the flame could not sustain itself (extinction limit) was not exactly determined in this study, but as a general guide the flame was not sustainable (blow out) around and above 3 G.

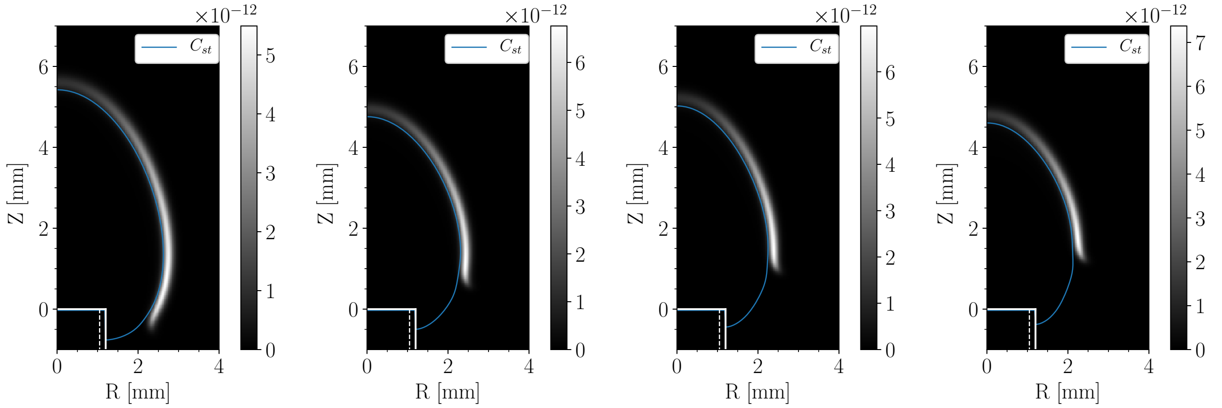

(a) 1.00 G. (b) 1.50 G. (c) 1.75 G. (d) 2.00 G.

Figure 6.14: Effect of body forces on CH^* mole fraction.

Fig. 6.15 shows the combined contour lines of each simulation case from Fig. 6.14 and compares them to the experimental equivalent CH^* chemiluminescence contour results using external electric fields (Fig. 4.2). The spatial comparison of simulated flame location with experimental shows very good agreement.

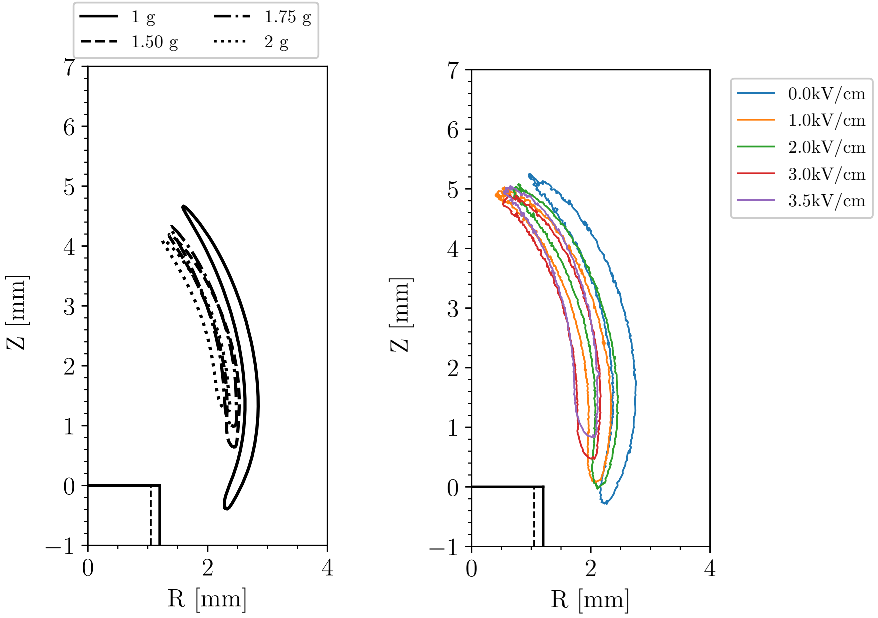

(a) CH^* contours - simulation (b) CH^* contours - experimental

Figure 6.15: Effect of body forces on CH^* mole fraction. Simulation versus experiment

Figs. 6.16a and 6.16b show the simulated percent change in peak CH^* mole fraction and difference in height of the flame's base, respectively, as a function of gravity level. These results are compared to the experimental results from Sec. 4.3 (re-shown in Figs. 6.16c and 6.16d).

The comparison of the flame's base height shows the enhanced gravity levels between 1-2 times that of normal gravity could increase the base height to the same levels as seen with external electric fields. The suggestion from Ch. 4 is that this increase in flame base lifting would increase the local mixing in this region which would be the cause of the observed increase in CH^* light emission from the flame. This is seen to happen in the simulations, however, the percent increase in peak CH^* mole fraction is much less than

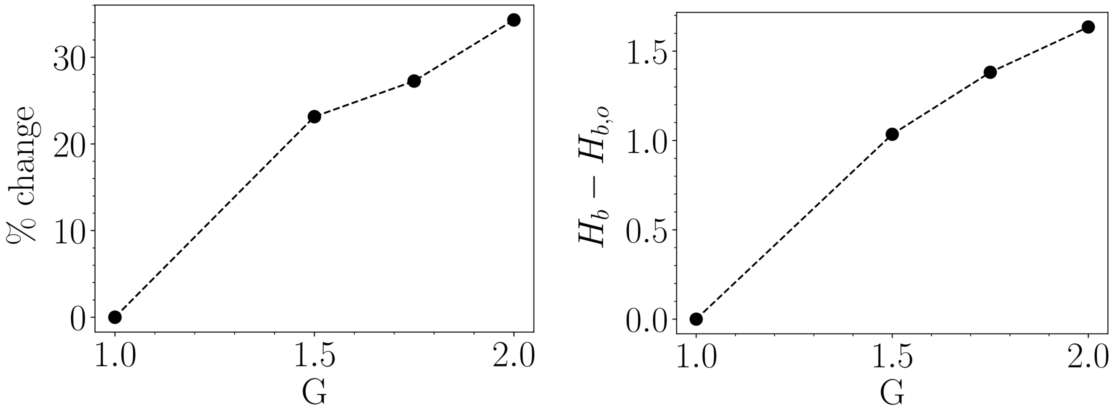

(a) peak mole fraction

(b) base height.

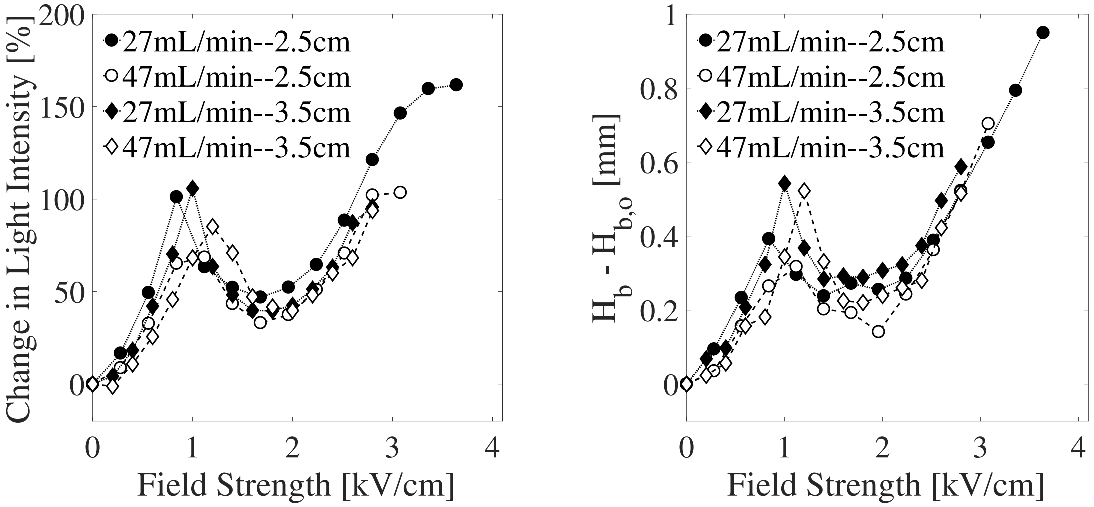

(c) Fig. 4.6c

(d) Fig. 4.6a

Figure 6.16: Effect of body forces on CH^* flame characteristics.

the percent increase in pixel light intensity from the CH^* chemiluminescence images. The incompatibility between the two results could be due to multiple causes.

1. the ion wind hypothesis presented in Ch. 4 is inadequate to explain the increase of CH^* pixel light intensity,

2. the similarities between ion wind body forces and buoyancy forces are enough to explain transport but are unable to capture CH^* chemistry,

3. the simulation is unable to capture the proper CH^* mole fractions at enhanced gravity

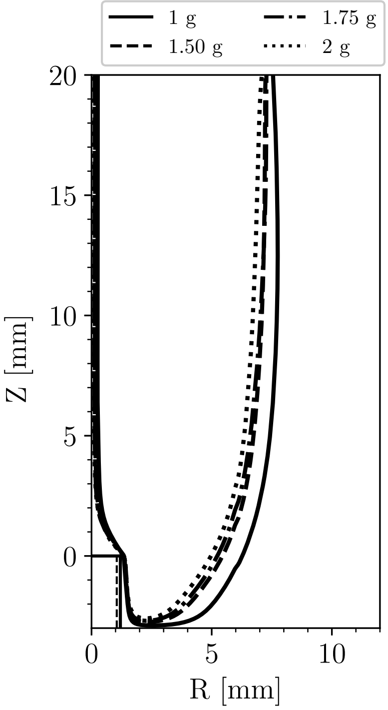

Figure 6.17: Simulated schlieren boundary layer thickness vs gravity.

levels due to inadequate chemistry, and

4. the simulations are predicting CH^* correctly and the CH^* experiments need to be quantitatively calibrated to ensure linearity.

While it is possible that experimental effects are partly responsible, the very significant uncertainties in chemical kinetics and the extremely low concentrations of excited species suggest that a quantitative comparison with computations is a major challenge.

Fig. 6.17 shows the results of the predicted schlieren radius under different gravity levels. Once again, the results show good qualitative agreement when compared with Fig. 5.8 but underpredict the thermal boundary layer reduction.

Fig. 6.18 shows the peak axial velocity predicted by the OpenFOAM simulations under increasing gravity fields. As would be expected, the axial velocity increases, but only by

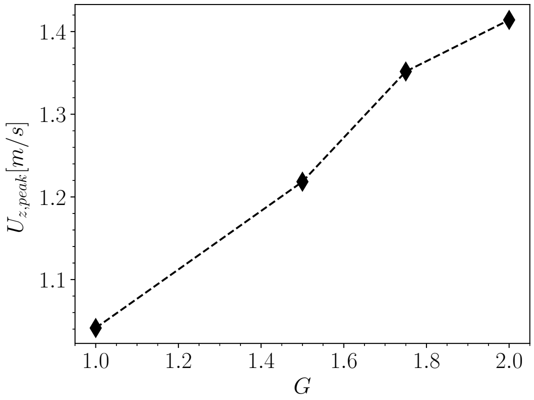

Figure 6.18: Predicted peak axial velocity, U_z, vs gravity.

about 40%. The velocity measurements underpredict what was suggested by the experiments using external fields. This finding seems reasonable in that thermally driven buoyancy is likely to be a more diffuse body force as compared to the more narrowly focused ion wind body force effect. While the overall influence is similar, the local flow acceleration will be more sensitive to streamline compression from the tightly directed electric field driven forces.

6.6 Conclusion

This chapter started by introducing the concept of testing the effect of body forces, such as ion winds, on non-premixed coflow methane flames. The openFOAM simulation was described and validated by testing the effect of boundary conditions and comparing multiple important flame parameters, e.g. flame geometry via CH^* chemiluminescence and predicted schlieren profiles, alongside experimental results without external electric fields. These tests showed very promising results. Enhancing gravity was then tested to see if generalizing ion wind forces into simple body forces, in this case buoyancy forces, is sufficient to explain the experimental results shown in the previous chapters.

The results showed that enhancing gravity was enough to explain nearly all the experimental observations, especially spatial variations in flame shape. The CH^* peak mole fraction and peak velocity were found to have disparities when compared to the experimental results. The peak CH^* peak mole fraction and peak velocity qualitatively agreed but significantly under-predicted the experimental results. It is not yet clear what is the reason for the difference. Thus, further studies should be made to clarify if the issue is in the hypothesis, the experiment, or the simulation.

Chapter 7

Analytical Flame Model

7.1 Introduction

The prior chapter provided the promising indications that a generalized body force could provide an important qualitative assessment tool for nonpremixed flames under the influence of electric fields. It is therefore interesting to extend that concept to the classical analytical nonpremixed flame models.

As described earlier, Burke and Schumann [1948] proposed an analytical model to describe the structure of axisymmetric diffusion (non-premixed) flames. In order to make the mathematics reasonable, some rather extreme simplifications were made to uncouple the governing equations. These simplifications include the following; *a*) the radial velocity was neglected and the axial velocity was in the upwards direction and constant everywhere, *b*) diffusion only occurred radially, *c*) infinitely fast chemical kinetics was used and the flame position occurred when the fuel and air concentrations were in stoichiometric proportions, and *d*) interdiffusion coefficients were constant. When considering the extent of their simplifications to an otherwise very difficult problem, Burke and Schumann [1948] were able to predict flame height remarkably well.

Roper [1977] extended the Burke and Schumann [1948] theory by including the radial velocity and the effects of body forces that produce acceleration in the axial velocity. The extensions were added to understand the effects of different burner geometries that the Burke and Schumann [1948] theory did not account for. One of the interesting points discussed by Roper [1977] is that when body forces are considered, such as gravity, it could be expected that an increase in velocity acceleration would increase the flame height. However, this was not been observed in experiments. Roper [1977]'s explanation is the increase in axial velocity produces a counteracting diffusion effect. Roper [1977]'s analysis shows that for circular burner nozzles, these two opposing effects cancel each other out and the flame height is seen to be independent of gravity. However, as shown by Sunderland et al. [1999] this independence from gravity does not apply universally. Sunderland et al. [1999] showed from comparisons of various experimental studies that microgravity flames have longer flame lengths than earth-gravity flames under the same conditions. It has been suggested by Krishnan et al. [2008] that the Roper model could be improved to match experimental data by selecting a more appropriate globally equivalent flame temperature.

These flame models have not been as successful in predicting flame widths as they have been in predicting flame heights. Vázquez-Espí [2001] performed a broader analysis that divided axisymmetric flames into two main categories; buoyancy driven and momentum-driven. While this idea was not new, and the concept of Froude number has been used for axisymmetric flames by others, Vázquez-Espí [2001]'s analysis sought to fully describe non-premixed conical-type flames by separating them into regimes defined by dimensionless parameters.

Far fewer analytical studies have been performed on the effects of electric fields on axisymmetric flames. This is likely due to the added challenge of including electrical aspects to an already challenging problem. As described above, studying the flame structure of buoyant and nonbuoyant flames requires many mathematical simplifications in order to decouple the equations of mass, species, momentum, and energy. The addition of electrical terms include *a*) an electrical body force in the momentum equation, *b*) a Lorentz force driven flux added to the diffusion velocities of charged species in species conservation equations, *c*) an Ohmic heating term in the energy equation, *d*) Maxwell's equation, and *e*) the addition of chemical effects due to nonelastic collisions between high energy electrons/ions and neutral species. The few analytical studies performed on electric field effects on flames have mostly been performed for 1D flame configurations; premixed flat flame, counterflow flames, spherical/droplet flames. These flame configurations allow for simplifications and decoupling of the governing equations. A series of theoretical studies on one dimensional, burner stabilized, premixed flames with electric field influence was made by Murphy et al. [2014], Sánchez-Sanz et al. [2015], and Murphy et al. [2017].

7.2 Roper's Model for Axially Symmetric Jet Flame

Following the work of Krishnan et al. [2008], who extended the works of Roper [1977] and Sunderland et al. [1997], the species conservation equation can yield the following governing equation for the mixture concentration of a combustible gas,

$$u_r(r,z)\frac{\partial C}{\partial r} + u_z(z)\frac{\partial C}{\partial z} - \frac{1}{r}\frac{\partial}{\partial r}\left(r\frac{\partial C}{\partial r}\right) = 0. \tag{7.1}$$

C is defined as $(f - f_a)/(f_0 - f_a)$ and f is defined as νX$_F$ - X$_O$. f$_0$ and f$_a$ are the initial jet and far field conditions, respectively. X$_F$ and X$_O$ are the mole fractions of fuel and oxidizer, respectively, and ν is the stoichiometric ratio between the oxidizer and fuel. Eq. (7.1) extends along the axial direction, $0 \leq$ z $< \infty$, and the radial direction, $0 \leq$ r $< \infty$.

The boundaries for Eq. (7.1) are defined as,

$$\begin{aligned} &C(r,0) = 1 && : r < d/2 \\ &C(r,0) = 0 && : r > d/2 \\ &C(r,\infty) \rightarrow 0 && : z \rightarrow \infty \end{aligned} \tag{7.2}$$

Roper [1977] performed a spatial variable transformation to Eq. (7.1). The spatial transformation is described in Eq. (7.3), where t(z) is the residence time.

$$t(z) = \int_0^z 1/u_z(z)dz, \tag{7.3a}$$

$$\eta(r,z) = r/r_D(z), \tag{7.3b}$$

$$\frac{d}{dt}(lnr_D) = u_r(r,z)/r, \tag{7.3c}$$

$$\theta(t) = D\int_0^t 1/r_D^2 dt \tag{7.3d}$$

The parameter r_D is the characteristic scale of diffusion. After applying the transformation to Eq. (7.1), the species concentration equation can be expressed in a much simpler form in terms of the new spatial variables, θ and η.

$$\frac{\partial C(\eta,\theta)}{\partial\theta} = \frac{1}{\eta}\frac{\partial}{\partial\eta}\Big(\eta\frac{\partial C}{\partial\eta}\Big). \tag{7.4}$$

The boundary conditions become $C(\eta,0) = 1$ for $\eta < 1$ and $C \rightarrow 0$ in the far field. The solution found by Sunderland et al. [1997] is shown in Eq. (7.5).

$$C(\eta,\theta) = \frac{e^{-\frac{\eta^2}{4\theta}}}{2\theta}\int_0^1 e^{-\frac{\eta_1^2}{4\theta}} I_0\Big(\frac{\eta\eta_1}{2\theta}\Big)\eta_1 d\eta_1 \tag{7.5}$$

where I_0 is the modified Bessel function of zeroth order. The location of the flame in the (η-θ) space can be found from Eqs. (7.5) by defining the flame as the location where the X_F and X_O are in their stoichiometric proportions. For methane and air that location is where

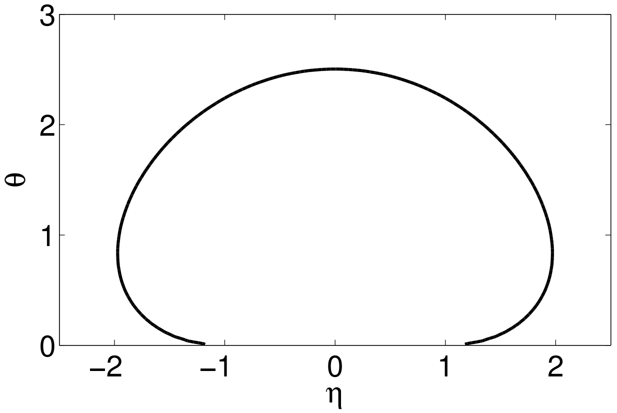

Figure 7.1: Flame contour plot of $C_{st} = 0.095$ in η-θ space

$C_{st} = 0.095$. Fig. 7.1 shows the flame contour of a methane flame defined by $C_{st} = 0.095$. For the location of the flame height, $C_{st}(\theta_F, 0) = 0.095$ when $\theta_F = 2.50$.

The conversion back from (η,θ) to (r,z) was demonstrated by Sunderland et al. [1997] for cylindrical coordinates. The characteristic diffusion length, r_D, is found to be,

$$r_D = \frac{d}{2}\Big(\frac{u_0 T_F}{u_z T_0}\Big)^{1/2}. \tag{7.6}$$

T_F is a characteristic flame temperature, T_0 is ambient temperature, u_z is the axial velocity of the gas, and u_0 is the velocity at the burner nozzle.

Using Eqs. (7.3a), (7.3d), (7.6) and $D = D_0(T_F/T_0)^{1.67}$,

$$\begin{aligned} z &= \frac{u_0 d^2}{4D_0}\Big(\frac{T_0}{T_F}\Big)^{0.67}\theta \\ &= \frac{\dot{Q}_0}{\pi D_0}\Big(\frac{T_0}{T_F}\Big)^{0.67}\theta \end{aligned} \tag{7.7}$$

where, $\dot{Q}_0$ in the second equality of Eq. (7.7) is the average volumetric flowrate, $\dot{Q}_0 = u_0 A_{nozzle}$

An important result that was pointed out by Roper [1977] and those who followed his work was that Eq. (7.7) shows that the flame height, $z_F = z(\theta_F = 2.50)$, has no dependence on the changes in flow velocity, u_z. That is, the accelerating effects of body forces acting on the gas (such as those due to buoyancy) do not affect the flame height. The explanation is that while the increase of velocity would have an effect of increasing the flame height it would also have a decreasing effect on the diffusion time related to transporting oxygen to the fuel. These two effects would cancel each other, and therefore, there is no observable change to the flame height.

Under Roper [1977]'s logic, it would then be expected that 1g and μg flames would have the same flame height for the same burner conditions and initial jet velocities. Likewise, under the "ion wind" theory, the flame height should remain the same under different electrical fields. However, Edelman et al. [1973] found that increasing buoyancy effects (0g to 1g) actually reduced the flame height. Similarly, it was seen in Ch. 4 that increasing the electric field also reduced the flame height. Roper [1977] recognized this finding in Edelman et al. [1973]'s work and indicated that the two effects must not entirely cancel exactly.

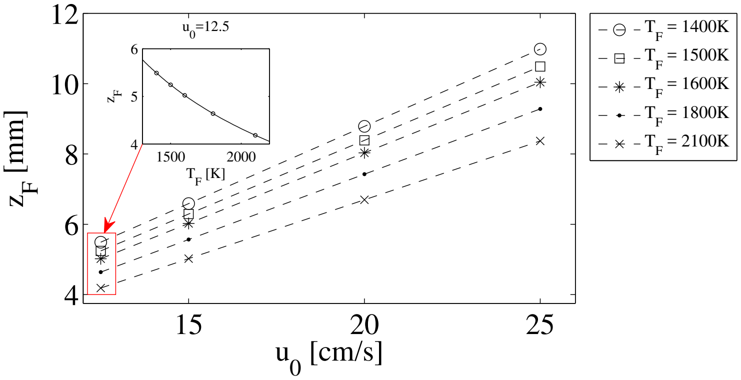

Figure 7.2: Flame height using extended Roper's Model

It was the works of Sunderland et al. [1997] and later Krishnan et al. [2008] who considered temperature effects to more accurately predict the flame height under various body forces. Similar to Roper [1977], Sunderland et al. [1997] found a $\left(T_o/T_F\right)^{0.67}$ relationship correlated with the flame height, Eq. (7.7). Roper [1977], as well as others, assumed in their analytical models that the flame temperature was the same between 0g and 1g flames. However, in reality, the temperature of a 0g flame is much lower even when keeping all other conditions the same. This occurrence is also related to the effect of gas acceleration on diffusion of oxidizer. The increase of diffusion time, caused by the lack of buoyancy induced acceleration in 0g, results in a "weaker" combustion reaction intensity. Fig. 7.2 shows the dependence of flame height with temperature and u_0 defined by Eq. (7.7). The works of Sunderland et al. [1997] and Krishnan et al. [2008] show how this explanation may be valid.

Turning now to the full geometry of the flame, the conversion of η to r can be found by combining Eqs. (7.3b) and (7.6),

$$r = \frac{d}{2}\Big(\frac{u_0 T_F}{u_z T_0}\Big)^{1/2}\eta \tag{7.8}$$

The axial velocity, u_z, needs to be defined. Roper [1977] used a one dimensional axial velocity in the form of Eq. (7.9) where a is the acceleration of the gas due to external body forces such as gravity. Sunderland et al. [1997] and Krishnan et al. [2008] used a definition of a derived from the Boussinesq approximation of buoyancy forces (Eq. (7.10)).

$$u_z(z) = \sqrt{u_o^2 + 2az} \tag{7.9}$$

$$u(z) = \sqrt{u_0^2 + 2\Big(\frac{T_F}{T_0} - 1\Big)gz}. \tag{7.10}$$

Fig. 7.3 shows the dependence of Roper's modified flame model with T_F via Eqs. (7.7), (7.8), and (7.10).

Fig. 7.3 shows a decreasing flame height with increasing flame temperature for both 0g and

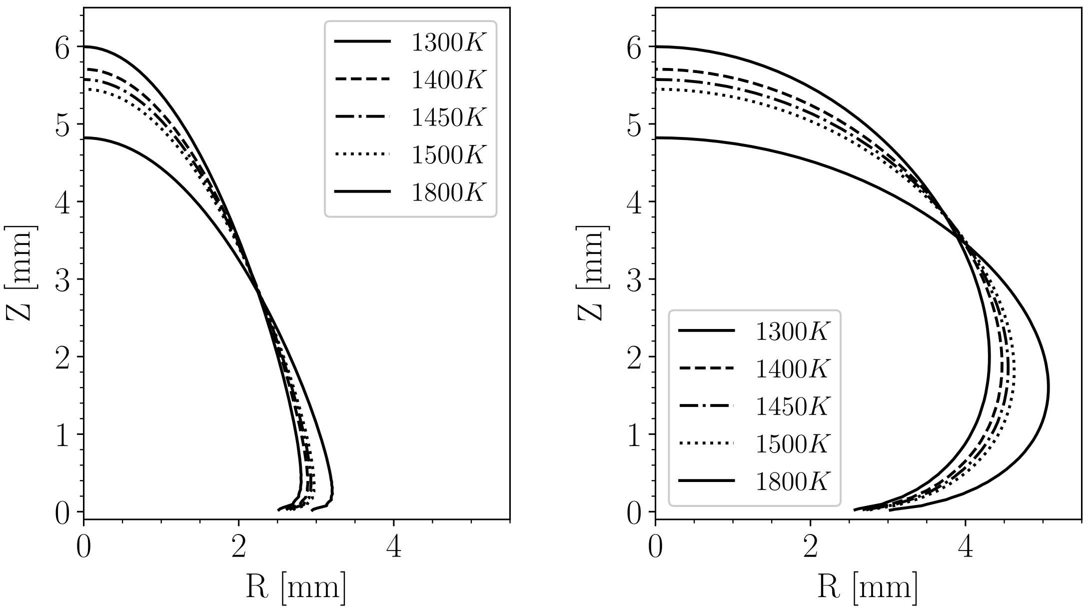

(a) w/ buoyancy effects. g = 9.81 m/s^2. (b) w/o buoyancy effects. g = 0 m/s^2.

Figure 7.3: Modified Roper flame contours in r-z coordinates: u_0 = 13 cm/s ($\dot{Q}_0$ = 27 mL/min). T_F dependence test.

1g agreeing with the hypothesis described above. However, the flame contour also grows in radius as the temperature is increased. The result is a more "compressed" flame contour with increasing temperature. It should be remembered that T_F isn't the flame temperature but rather a characteristic temperature that represents the temperature of the entire flame volume consistent with the appropriate force of a buoyancy driven acceleration.

As expected, the 0g case in Fig. 7.3b predicts the same flame heights with respect to temperature as the 1g case (Fig. 7.3a). The lower temperatures , e.g. T_F = 1200 & 1400 K, appear to have better predicted flame contours with what is to be expected from 0g flames. However, this has yet to be verified with micro-gravity experimental results.

Because of the complex coupling between temperature and buoyancy effects, the direct comparison of the results in Fig. 7.3 to experimental results is not so easy to perform. However, from a qualitative perspective, it was shown earlier that a temperature dependence was needed to accurately predict flame height but a temperature dependent flame radius appears to be much harder to predict. This is shown in Fig. 7.4. This figure shows the Roper model can most accurately predict the flame height with a T_F around 1450 - 1500 K. Higher temperatures underpredict the flame height while lower temperatures overpredict it. In all cases however, the flame's curvature is very poorly predicted.

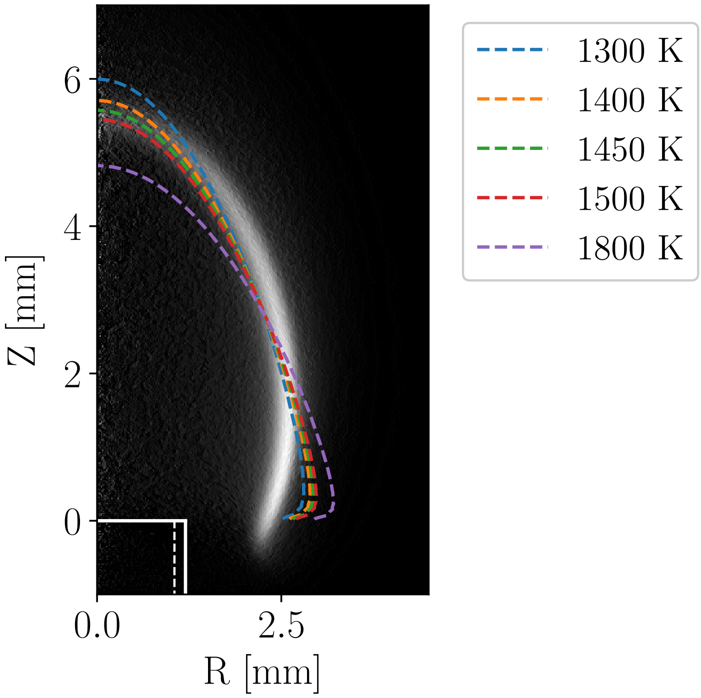

Figure 7.4: Comparison of modified Roper flame model vs experimental CH^* chemiluminescence.

Temperature effects appear in the model due to two mechanisms; the diffusion coefficient defined by $D = D_o \times (T_F/To)^{1.67}$ and the temperature dependent axial velocity, u_z defined by Eq. (7.10). In order to isolate these two effects, the simpler form of u_z (Eq. (7.9)) can be used instead. Presenting the axial velocity in the form of Eq. (7.9) is particularly useful in order to test the ion wind effect which, unlike buoyancy, is weakly dependent on temperature through ion production.

If ion production is assumed to be weakly dependent on temperature and the ion wind

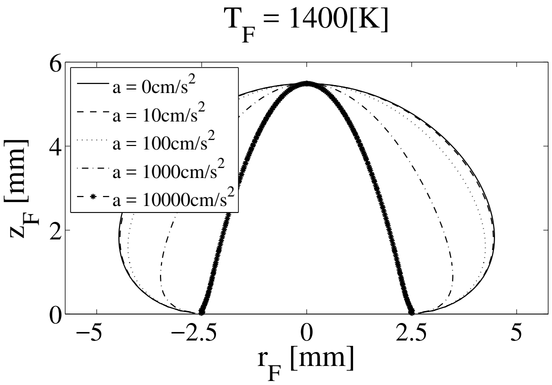

(a) $T_F = 1400$ K

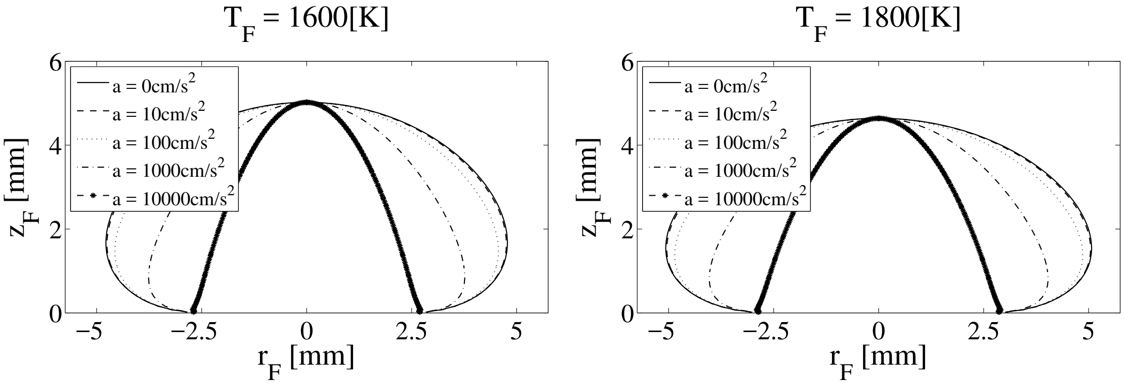

(b) $T_F = 1600$ K

(c) $T_F = 1800$ K

Figure 7.5: Flame contours in r-z coordinates showing the effect of a temperature independent acceleration.

has negligible enhancement due to the temperature field, then the total acceleration of the gas could be much more easily controlled without affecting the temperature dependence of other parameters. Fig. 7.5 shows the result when substituting Eq. (7.9) into the modified Roper Model and varying the total acceleration, a. The results shows qualitative agreement with experimental observations made while studying electric field effects on flames. These agreements are summarized below.

1. An increase in total axial velocity acceleration due to body forces (e.g. buoyancy and ion wind) results in thinner flame contours.

2. At high enough axial acceleration, the radial portion of the flame contours decreases

in curvature which produces more triangular looking flames. This has been seen experimentally by 1g electric field enhanced flames at very high electric field strengths.

3. The hypothesis that acceleration slightly modifies the near flame temperature field is enough to explain a slight decrease in height.

Points 1 & 2 suggest that the selection of u_z in the form of Eq. (7.9) (as suggested by Roper [1977]) is sufficient to describe the full flame contour.

As a final point to mention related to these results, Fig. 7.5 still shows a dramatic flame radius dependence on increasing temperature. Because this simple analytical model does not have the ability to accurately predict the temperature gradients in a flame, the temperature, T_F, could be thought of as a volumetrically averaged gas temperature that must be less than the adiabatic flame temperature (T_{ad} = 2200 K for methane). Roper [1977] proposed using T_F = 1500 K. Sunderland et al. [1997] proposed a much higher value for 1g flames, T_F = 2690 K and T_F = 1370 K for 0g flames. Krishnan et al. [2008] showed that using a varying temperature produced worse flame contour predictions. The work here shows that selecting T_F close to adiabatic temperature has an unfavorable effect on the radial portion of flame contour.

This section describes the usefulness of simple jet diffusion flame models in order to study the important parameters that control the geometry of a flame's shape. The flame contour analysis presented here shows the complex nature of a 2D flame even with the use of such a simplified model. This is because of the complex physical phenomenas occurring where coupling between temperature and body forces play major roles. This shows that there is still much research needed in order to improve our understanding before these models can be made usable for different environments (1g, 0g, external electric fields, etc...) without sacrificing their simplicity and predictability.

7.3 Electric Bernoulli's Equation

As is hinted out by the prior section, a simple analytical model describing the acceleration of gas due to ion wind forces is needed to further develop the Roper-type flame model. The proposal here is the development of a simple axial velocity derived from a Bernoulli type equation that considers effects of initial gas velocity, buoyancy driven acceleration, and external field driven acceleration.

We start with the inviscid, steady state form of the momentum equation including a body force term due to gravity and one due to the electric field term (Eq. (7.11)).

$$\nabla \cdot \left(\vec{u}\vec{u} \right) = -\frac{\nabla P}{\rho} + \vec{g} + \frac{\vec{F}_e}{\rho} \tag{7.11}$$

Using the Boussinesq approximation, its assumed that the only effects of pressure are due to the hydrostatic pressure evaluated at the ambient pressure $\nabla P = \rho_a \vec{g}$.

$$-\frac{\nabla P}{\rho} + \vec{g} = \left(1 - \frac{\rho_a}{\rho} \right) \vec{g} \tag{7.12}$$

Making the simplification that density only varies with temperature (constant pressure) and using the ideal gas law, Eq. (7.11) can be written as,

$$\nabla \cdot \left(\vec{u}\vec{u} \right) = \left(1 - \frac{T_F}{T_a} \right) \vec{g} + \frac{\vec{F}_e}{\rho} \tag{7.13}$$

The ion wind body force, $\vec{F}_e$, can be defined by Eq. (7.14) as suggested by Lawton and Weinberg [1970].

$$\vec{F}_e = \vec{E} e (n_+ - n_-) \tag{7.14}$$

Using Eq. (7.14), $\vec{g} = -\nabla \Omega_g$, and $\vec{E} = -\nabla \Phi$ into Eq. (7.13), it can be derived an electrically forced simplified form of the momentum equation.

$$\nabla \cdot \Big(\vec{u}\vec{u}\Big) = -\nabla\Big(\Omega_g(1 - \frac{T_F}{T_a})\Big) - \nabla\Big(\Phi\frac{e(n_+ - n_-)}{\rho}\Big) \tag{7.15}$$

Next, the vector identity for $\nabla \cdot \Big(\vec{u}\vec{u}\Big)$ can be used in Eq. (7.15) and then integrated along a streamline, $d\vec{r}$.

$$d\vec{r} \cdot \Big[\nabla(\tfrac{1}{2}u^2) - \vec{u} \times \vec{\omega} + \nabla\Big(\Omega_g(1 - \tfrac{T_F}{T_a})\Big) + \nabla\Big(\Phi\tfrac{e(n_+ - n_-)}{\rho}\Big)\Big] = 0, \tag{7.16}$$

For this analysis, we assume a potential flow ($\vec{\omega} = 0$) and recognize that $d\vec{r} \cdot [f] = 0$ means that f is constant along a streamline, and therefore,

$$\frac{1}{2}u^2 + \Omega_g\Big(1 - \frac{T_F}{T_a}\Big) + \Phi\frac{e(n_+ - n_-)}{\rho} = constant. \tag{7.17}$$

Eq. (7.17) is a Bernoulli equation, and shows that along a streamline the kinetic energy and the potential energies due to both gravity and electrostatics are conserved. The substitution $\Omega_g = gz$ into the second term on the left can show the buoyancy term's dependence on the z-direction. However, the electrical term (3rd) has two unknown parameters, Φ and $n_\pm$. Detailed analysis would involve solving the species conservation equation (Eq. (7.18)) for ions and electrons along with Gauss' Law (Eq. (7.19)) and the electric potential,

$$\frac{\partial q_i}{\partial t} + \nabla \cdot \vec{J_i} = \omega_i \tag{7.18}$$

$$\nabla \cdot \vec{E} = \frac{1}{\epsilon_o}\sum_i (S_i q_i) \tag{7.19}$$

where $q_i = en_i$ is the charge density of species i, $\vec{J_i} = q_i U_i$ is the current density, S_i is the charge number of species i (+1 for ions and -1 for electrons). If we take $q = \sum_i (S_i q_i)$ and substitute the electric potential for $\vec{E}$, then Eq. (7.19) will become Poisson's equation.

$$\nabla^2\Phi = -\frac{q}{\epsilon_o} \tag{7.20}$$

The 1D solution to Eq. (7.20) with boundary conditions $\Phi(z = 0) = 0$ and $\Phi(H) = \triangle V$ and assuming negligible space charge effects, $q \simeq 0$, is

$$\Phi(z) = \frac{\triangle V}{H} z \tag{7.21}$$

As analyzed in more detail later, it is useful to note that the assumption of negligible space charge effects is reasonable (except perhaps very near the flame) even though the same charges produce non-negligible flow forcing in an external field. The reason is that the very dilute concentration keeps interactions between charges small while the very strong external field acts on them independently. Using this result in Eq. (7.17) and substituting $\Omega_g = gz$,

$$u(z) = \sqrt{u_0^2 + 2\Big(\frac{T_F}{T_a} - 1\Big)gz - \frac{2\triangle Vq}{H\rho}z} \tag{7.22}$$

or by using the relationship,

$$\frac{n_+ - n_-}{\rho(T_F)} = N_a\Big(\frac{Y_+}{M_+} - \frac{Y_-}{M_-}\Big) \tag{7.23}$$

Eq. (7.22) can be rewritten as,

$$u(z) = \sqrt{u_0^2 + 2\Big(\frac{T_F}{T_a} - 1\Big)gz - \frac{2e\triangle VN_a}{H}\Big(\frac{Y_+}{M_+} - \frac{Y_-}{M_-}\Big)z} \tag{7.24}$$

N$_a$ is Avogadro's number, Y$_\pm$ is the mass fraction of ions and electrons, and M$_\pm$ is the molecular weight of ions and electrons. The third term inside the square root is the electrical component that accelerates the bulk gas. This result represents the case where space charge effects are small enough to have a negligible effect on the electric potential but still large enough to have a drag effect on the bulk gas.

In the application of external fields on non-premixed flames, charge separation will occur resulting in positive chemi-ions migrating away from the electrons/negative chemi-ions. Furthermore, with the application of external fields on burner attached flames with the external field pointing downstream of the burner, the electrons and negative chemi-ions will have a much shorter path to travel to the electrode. The shorter path will mean less interaction with the neutral gas, and thus less contribution to the gas acceleration. Therefore, we can make another simplification that the electrical acceleration term in Eq. (7.24) will be solely due to positive chemi-ions. Eq. (7.24) can then be written as,

$$u(z) = \sqrt{u_0^2 + 2\Big(\frac{T_F}{T_a} - 1\Big)gz - \frac{2e \triangle V N_a Y_+}{H M_+} z} \tag{7.25}$$

It is readily seen that Eq. (7.25) maintains the same form as used by Krishnan et al. [2008] if $\triangle V = 0$. Defining acceleration terms as shown in Eq. (7.26), Fig. 7.6 shows the evaluation of buoyancy and electrical forces. Figs. (7.6b) and (7.6c) are evaluated using a temperature dependent density for air (see Eq. (7.23)). The red lines in these figures represent the evaluation of a_{elect} using a calculated density of air at 300 K.

$$a_{buoy} = 2\Big(\frac{T_F}{T_a} - 1\Big)g, \tag{7.26a}$$

$$a_{elect} = \frac{2e \triangle V N_a Y_+}{H M_+}, \tag{7.26b}$$

To estimate more explicitly the conditions under which space charges can be neglected, we can go back to Eq. (7.20) but this time retain the space charge as a potential source. To

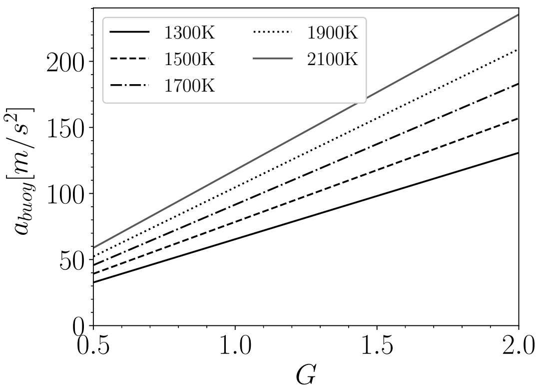

(a) a_{buoy}.

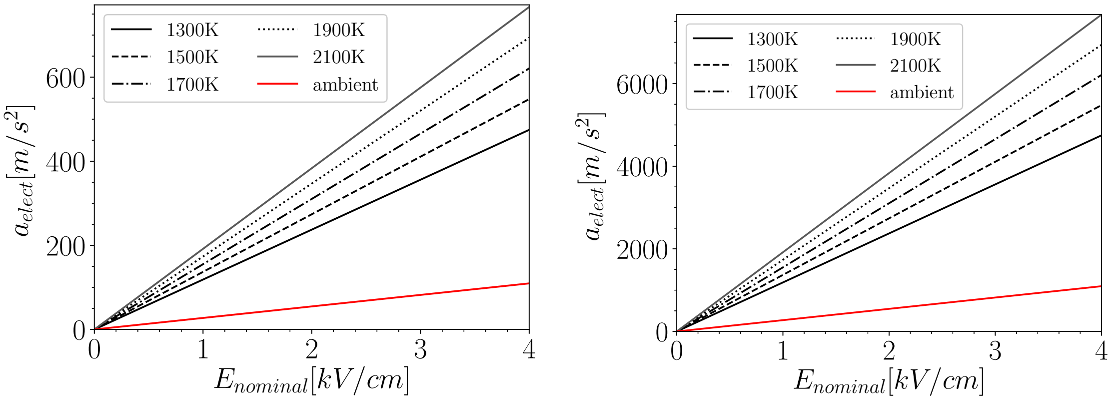

(b) a_{elect} : $n_+ = 10^9$ cm-3.

(c) a_{elect} : $n_+ = 10^{10}$ cm-3.

Figure 7.6: Acceleration terms from buoyancy and ion currents.

simplify the analysis without loss of generality in terms of relative magnitudes, the space charge is assumed to be uniform through the region. Then, the 1D solution becomes,

$$\frac{\Phi(z)}{\triangle V} = \xi + k_e(\xi^2 - \xi) \tag{7.27}$$

$$k_e = -\frac{qH^2}{2\epsilon_o \triangle V} \quad ; \quad \xi = z/H \tag{7.28}$$

Fig. 7.7 plots the results of the dimensionless electric potential of Eq. (7.27) for different values of k_e. As expected, as $k_e \to 0$ the effects of space charge are negligible. However, when $k_e \geq 1$ the space charge has a noticeable effect. Also, notice that for $k_e > 1$ the space charge creates large potential barriers for the electrical properties considered for the small

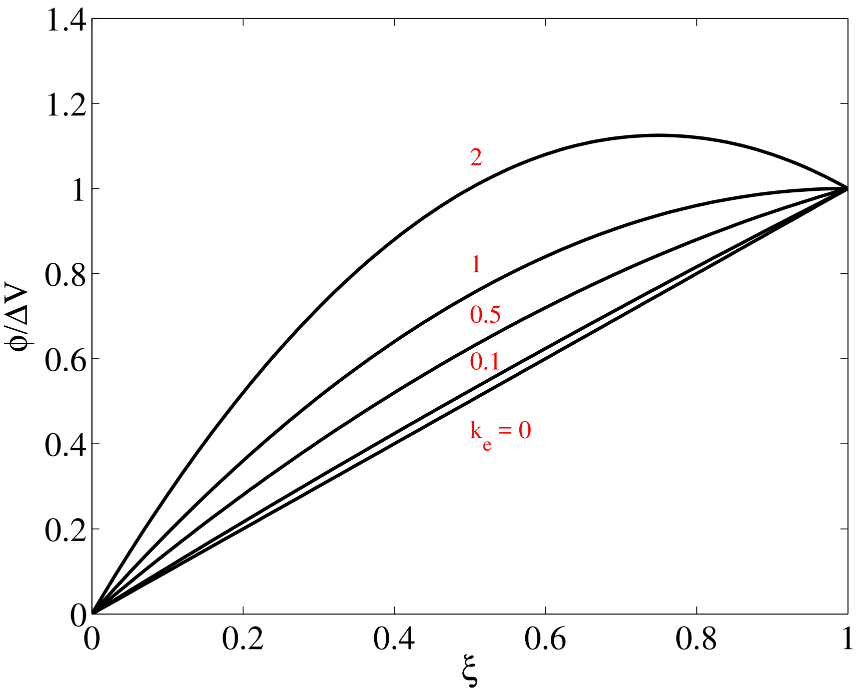

Figure 7.7: 1D Normalized Solution to Poisson's equation for constant, uniform source

methane diffusion flame considered here ($n_+ \sim 10^{15}-10^{16}$ m^{-3}) under electric fields with an order of magnitude of 10^3 V, $k_e \sim 10^1 - 10^2$. Thus, for the regions of the flow where the charges have been distributed to concentrations on the order of typical flame ion values, the space charge will have a significant effect on the local field strength. Importantly, it is in this distributed space region that the majority of the ion-driven wind force is generated so the assumption is particularly good for the estimation of the flow forcing created.

For the sake of completeness of this analysis, we can state the 1D solution to Eq. (7.20) with boundary conditions $\Phi(z = 0) = 0$ and $\Phi(H) = \triangle V$ and $q(z) \neq 0$ in terms of the Green function, $G(z, z_o)$,

$$\Phi(z) = -\frac{1}{\epsilon_o}\int_0^H q(z_o)G(z, z_o)\mathrm{d}z_o + \frac{\triangle V}{H}z \tag{7.29}$$

The first term on the right hand side represents the contribution to the electric potential due to the space charge, q, while the second term is only due to the boundary conditions (electrode potentials). From an electrical property of flames point of view, the first term could be thought of as the contribution from the flame's own internal electric field and the second term as the contribution from the external electric field. Once again solving for $q(z_o)$, and simplifying $q(z) = en_+ f(z)$, where $f(z)$ is dimensionless and defines the shape, and then dividing both sides of Eq. (7.29) by $\triangle V$,

$$\frac{\Phi(z)}{\triangle V} = -\Big(\frac{en_f}{\epsilon_o \triangle V}\Big)[f(z)] + \frac{z}{H}, \tag{7.30}$$

$$[f(z)] = \int_0^H f(z_o)G(z, z_o)\,\mathrm{d}z_o \tag{7.31}$$

It has been recorded in the literature that hydrocarbon flames can produce ion number densities between 10^{13} - 10^{16} m^{-3} through chemi-ionization. The order of magnitude for the parameters in the parenthesis in Eq. (7.30) is between 10^2 - 10^4 for $\triangle V$ in the kilovolt range compared to the second term which has an order of magnitude of 1. While the actual value of q is largely dependent on the shape function, $f(z)$, this simple analysis shows that space charge effects can have a significant effect in regions of the system where the charges are concentrated. Increasing electrode voltages will reduce the space charge effects, but within the formation zone and for detailed local understanding near the flame sheet, space charge effects in electric field combustion should not be disregarded. However, for analytical methods, an efficient way to handle the complicated space charge effects is still needed. Nevertheless, for the bulk flow region that is the focus of the simple analysis presented above, Eq. (7.24) is sufficient for moving forward. Some of the issues of where this simplified analysis might be refined will be discussed and improvements may be studied in future work.

7.4 Conclusion

Theoretical study on the geometry of non-premixed axially symmetric flames was performed by using a modified version of the Roper flame model. Because ion wind theory uses an electrical body force to explain the effects of an external field on chemi-ion producing flames, the hypothesis presented in this thesis is that it should be possible to draw parallels between electrical body forces and varying levels of gravity forces. After reviewing the literature on the Burke and Schumann flame model, the underlying mechanisms which control the flame's geometry were determined. The Roper model proved to be capable of predicting reasonably well the height of a Burke and Schumann type flame. The flame radius was less successful at predicting the curvature of the flame but the overall radius of the flame was found to be within reason especially when considering the simplicity of the model. The buoyancy forces and electrical forces were generalized to a simple acceleration term, a, which acts on the gas. The geometry of the flame was tested under different values of a to see what types of strengths would reproduce the experimental results of external fields acting on the flame. The temperature at which the transport parameters are evaluated at was found to be an important feature in order to reproduce the experimentally obtained flame heights.

A one dimensional axial velocity equation was derived from a Bernoulli type equation which includes buoyancy forces and electrical body forces. This formula was used to compare the acceleration strength of the buoyancy forces to the electrical forces on the gas velocity. A simplification was made by neglecting space charge in the Laplace equation while solving for the electric potential in order to manage the complicated effects of space charge. Space charge was, however, maintained in the electrical body force term. Under this approximation, the accelerating capabilities of external electric fields were found to be up to one order of magnitude higher compared to buoyancy forces for the gravity levels and field strengths tested in this thesis.

This theoretical analysis successfully showed that ion wind theory combined with the Roper flame model could be used to reproduce the flame geometries that were observed due to the application of external electric fields.

Chapter 8

Conclusion

Non-premixed methane flames exposed to external electric fields were studied in this dissertation. Axially symmetric, conical-type flames were chosen because of their ability to maintain their symmetry under longitudinal electric fields. Because of the complex nature of ion winds acting on the flame, multiple approaches were made; experimental, numerical, and theoretical methods.

8.1 Experimental

The experimental portions focused on three main categories:

- ion currents and I-V curves,
- flame dynamics.
- chemi-ion driven flows.

8.1.1 Ion Currents

Current-voltage curves (I-V curves) are under utilized measurements in electric field combustion studies. The ability to use external fields to manipulate flames has been demonstrated in the literature. The topic of using external electric fields instead as a diagnostic tool is mentioned less often but still possesses great potential. This requires more studies of the ion current itself. Ion currents and I-V curves can provide numerous pieces of information about the flame and the interaction between chemi-ions and the gas. Some examples of their applications were described and demonstrated. In Ch. 3, it was demonstrated how ion current measurements and I-V curves could be used to diagnose the flame and the flame's reactions where field strength or applied voltages cannot alone be deterministic. This is possible because the ion current is a total charge flux measurement with strong implications to the strength of the ion wind body force.

The I-V curves for jet and coflow stabilized methane flames were found. Sub-saturation and saturation ion currents were identified for varying electric field strengths. Saturation ion currents were found to at approximately 1 kV/cm for the methane flames tested. Enhanced saturation ion currents were found to appear in the I-V curves at approximately 2 kV/cm for the extruded tube coflow burner and approximately 3 kV/cm for the flush tube coflow burner. The enhanced ion currents have been hypothesized to be occurring due to manipulation of local mixing and flame geometry due to strong ion winds. Instabilities were found in the ion current measurements which indicated flame/ gaseous flow instabilities. These instabilities were explained by the onset of secondary ion productions. Strong enough instabilities were able to cause flame extinction. The ion current measurements were also demonstrated to be strong indicators of changes to flame characteristics, such as flame geometry and light emission.

Electric probe

A long wire electric probe was used to measure the ion current density beneath the mesh electrode. Ion current measurements are global measurements which makes them limited in their ability to quantify ion wind forces. Ion current density, on the other hand, can be used for this purpose. The deconvolved ion current density was measured between 2-4 μ/cm^2 within an effective cross-sectional area with a diameter of 5-10 mm. With field strengths above 2.5 kV/cm, the long wire probe measurements produced unreliable results due to secondary ion currents which over predict the ion current density due to chemi-ions. A unique feature of the ion current density profiles was that the peak measurement was not found on the central axis, but rather at a radius of 2-3 mm offset from the center axis. This data provides an excellent opportunity for those computing flames in electric fields to test the accuracy of their simulations with spatially resolved ion fluxes.

8.1.2 Flame Dynamics

The external electric field effects on flame dynamics was studied by measuring various flame properties via CH^* chemiluminescence. The location of light emission via CH^* chemiluminescence is commonly used as a spatial marker for the flame's reaction zone. This study helps understand the interaction between the ion currents and the flame. The deconvolved CH^* profiles were studied for the two coflow burners.

Extruded tube coflow

For the extruded tube coflow burner, the flame was seen to have a decrease in height and a decrease in radius as the field strength was increased in the positive direction. The base height of the flame increased significantly and the emission of light also increased. The amount of base height lifting and the light emission both correlated well with the ion current measurements indicating a possible coupling between them.

For increasingly negative field strengths the opposite occurs; the flame height increased, the radius increased, the height of the flame base decreased (and flared outwards), and light emission decreased.

Flush tube coflow

For the flush tube coflow burner, the flame height decreased and flame radius decreased with increasingly positive electric field strengths. The base height of the flame was found to be insensitive to the field strength but the light emission from the CH^* chemiluminescence was found to have a similar correlation to the ion current as was found in the extruded tube coflow case. This may indicate that the lifting of the flame's base does not have a strong influence on local mixing as previously suggested and that some other mechanism may be the cause of the enhanced chemi-ion and chemiluminescence production.

8.1.3 Chemi-Ion Driven Flows

The flow field was studied using schlieren imaging to visualize the thermal boundary layer reacting to ion winds. For the sudden activation of an external electric field, the thermal boundary layer was observed to have formed a wave propagating from the region near the flame to the downstream mesh electrode. The wave was measured to have a velocity of under 1 m/s for below saturation field strengths to several m/s for field strengths above saturation. These wave velocities are typical for gas velocities expected from ion winds. The propagation of the wave lasted for approximately 45-50 ms under field strengths of about 1.25 kV/cm. However, the full stabilization of the schlieren image wasn't achieved until after 90-100 ms.

The thermal boundary layer was seen to have a decreasing radius with increasing field strength. The thermal boundary layer with a radius of approximately 8 mm without a field was seen to decrease as much as 4 mm for field strength of >2 kV/cm. This decrease in the thermal boundary layer was caused by the enhanced convection from the ion winds.

8.2 Numerical

The numerical portion of this dissertation described the creation of a reacting multi-component CFD model using OpenFOAM to simulate an extruded tube coflow burner. Though the numerical model does not include Maxwell's equations or chemi-ions, the goal was to determine if ion winds could be generalized to a more simple body force that can be simulated more easily in a CFD model. Buoyancy forces have been shown to produce comparable force densities to those produced by ion wind forces. Therefore, the manipulation of buoyancy forces would be a reasonable method of testing ion wind forces without the necessity of complicated Maxwell's equations and chemi-ion chemistry; both of which still need significant study to be understood completely.

The validation of the numerical model showed reasonable predictions of various flame characteristics. These include flame temperatures, CH^* chemiluminescence profiles and calculated schlieren profiles agreeing with the experimental results of flames without external electric fields.

With the gravity level increased in the simulations, the spatial features (flame height, radius, base height) of the CH^* profiles showed excellent agreement with what occurred during the application of external electric fields. This implies that ion winds acting as body forces can very well explain the experimental observations of flame dynamics. However, the change in predicted peak CH^* mole fraction was seen to underpredict what was experimentally obtained for external electric fields with the same amount of flame base lifting. For external fields that produce 0.4-0.5 mm change in base height, an increase of flame light emission of 70-100% was measured in the experiments. For the simulations, the largest increase in peak CH^* mole fraction was predicted to be 35% for a change in base height higher than 1.5 mm. While more research is needed to identify the source of these differences, it is likely the number of uncertainties in the numerical model that produces the majority of the quantitative discrepancy. For example, CH^* is a minor constituent with peak mole fractions on the order of 1e-12. Many uncertainties will be involved in the process of predicting a species with such extremely small concentrations.

The predicted change in schlieren radius under enhanced gravity levels was also found to share qualitative agreement with the experimentally obtained change in schlieren radius under external electric fields but also underpredicted. The differences may again be explained by the uncertainties in the numerical model where the simplified implementation of transport used in the OpenFOAM equations could be the source causing the insufficient prediction.

8.3 Theoretical

The Roper flame model was used to analyze the flame location of a Burke-Schumann type flame. The parameters of the flame model were analyzed to understand the underlying mechanisms involved in determining where the flame will be located. The most important parameters found were the initial velocity, acceleration due to body forces, and temperature dependent transport coefficients. As was done through the numerical model, the acceleration term was generalized to a simple acceleration term (indistinguishable from buoyancy).

As it was found in previous studies in the literature, the Roper model proved once again to be a reliable model for predicting flame height, but not for predicting the overall flame geometry. Overall, the Roper does produce good qualitative predictions of flame contours.

To better understand how the gas flow would react to ion winds, a Bernoulli type equation was derived which includes body forces due to gravity and ion winds. This equation was then used to find the one dimensional equation for the axial velocity of a gas accelerated by buoyancy and ion wind forces. However, the current form of the equation is simplified in how it manages space charge; a concept that is known to be difficult to manage. Further development on this derivation by including a higher order of approximation of space charge effects could lead to a better understanding of the interaction between ion winds and gaseous flows. Still, in its current simplified form, this derivation has the capability of predicting well axial gas velocities within a reasonable order of magnitude.

8.4 Final Conclusion

At the beginning of this dissertation two questions were raised.

1. Is ion wind theory enough to explain the effects observed when an external electric field is applied to a methane flame stabilized on an axisymmetric burner?
2. How does an ion wind produce these observed effects?

While the discrepancies between the simulation and experimental results needs to be analyzed further, ion wind body forces are sufficient to explain much of what is observed during the application of external electric fields. However, the results also leave open the possibility that other mechanisms may be at play that would determine the cause of the enhancement to the chemi-ion production and CH^* chemiluminescence; something that is not completely explained by the hypothesis of local mixing due to ion wind flame base lifting. The evidence that shows that the enhanced mixing hypothesis is inadequate is in the discrepancies between the flush tube coflow burner and the extruded tube burner and the disparity between the experimental CH^* chemiluminescence light emission and the calculated peak CH^* mole fractions. Still, more analysis is needed to understand the differences and how much is caused by unknowns in both the experiments and the numerical simulations.

8.4.1 Further Work: Advanced Combustion via Microgravity Experiments

One major complication that appears in the experiments, simulations, and theoretical work is the effect of gravity. The magnitude of buoyancy forces is on the same order of magnitude as ion wind body forces. Whether the flow field is enhanced by ion wind forces or other types of body forces (e.g. buoyancy), the thermal field will experience modifications via the complex interaction between transport, chemical mixing, and chemical reactions (all of which are very dependent on temperature themselves). The strength of the buoyancy force is also heavily dependent on temperature. Even the ion wind body force may have some dependence on temperature through the chemi-ion production rates. The problem is further complicated by the possibility of electronic induced enhanced chemical reactions and electronic induced JSoule heating effects.

Performing experiments in a way that would allow the decoupling of ion wind effects from buoyancy effects is highly desired. A microgravity based laboratory such as the one available on the International Space Station (ISS) is an optimal environment for performing this sort of buoyancy decoupled experiments. Advance Combustion Via Microgravity Experiments, ACME, is a program of the NASA Glenn Research Center to provide academic research groups the opportunity to perform combustion experiments on-board the ISS. The Electric Field Effects on Laminar Diffusion Flames team, or E-FIELD Flames, is one university research group that is apart of ACME. The experiments performed on the ISS by the E-

FIELD Flames will be the microgravity complement to the earth gravity based experiments described in this dissertation .

The burners that will be used during the E-FIELD Flames experiments are similar to the jet burner and the extruded tube coflow burner described in this dissertation. The electrical configuration is also similar to the one described in this dissertation. However, because of the strict requirements of EMI limits on equipment, low-power high voltage power supplies were selected due to their compact size and low EMI emission. The performance of these power supplies, however, lack in transient response. This was shown by Chien [2015]. The steady state performance of the power supplies have shown to be reliable for stable flame studies. The effect of the poor time response of the power supply will be examined in future studies.

The available diagnostics on-board the ISS are total flame light emission and discrete light emission via CH^* and OH^*. These measurements can be captured through photo-multiplier tubes (PMT) for global measurements and through various cameras available on the Combustion Integrated Rack (CIR). Quantification of the CH^* and OH^* images will be available through color characterization and calibration of the camera optics and sensors. Description of the calibration can be found in Giassi [2017]. Transient ion current measurements and voltage measurements are also available. For cases where soot is present in significant amounts, soot pyrometry and soot volume fraction is also available.

Methane and ethylene flames will be tested. Methane is a relatively soot-free fuel and will be used to study flame geometry and emission of light from chemiluminescence. The effects of electric fields on flame stability and extinction will also by tested by variably diluting the fuel with nitrogen and varying the velocity of coflowing air. The same observations will be made with ethylene. Since ethylene is a much more soot producing fuel, it will also allow for a more in depth study of soot production under varying electric fields. The results of these test will be characterized by the ion current measurements as was done in this thesis.

The ISS experiments are currently scheduled to begin in March of 2018. The results of this dissertation will be an important guide to evaluating those experiments and to completely characterizing the effects of electric fields on small coflow nonpremixed flames.

In terms of the numerical simulation, one that includes chemi-ion chemistry and Maxwell's equations is also desired. These microgravity experiments combined with microgravity numerical models promise to provide the necessary decoupling of buoyancy forces in order to directly observe the interaction of chemi-ions and electrons on with flame dynamics.

Bibliography

Hartwell F. Calcote. Electrical properties of flames. *Symposium on Combustion and Flame, and Explosion Phenomena*, 3(1):245–253, 1948.

A P Chattock. On the Velocity and Mass of the Ions in the Electric Wind in Air. *The Philosophical Magazine*, 48(294):401–421, 1899.

J. Lawton and Felix J. Weinberg. *Electrical Aspects of Combustion.* Oxford University Press, 1970.

HC Jaggers and A Von Engel. The effect of electric fields on the burning velocity of various flames. *Combustion and Flame*, 285, 1971.

WJ Miller. Ions in flames: evaluation and prognosis. *Symposium (International) on Combustion*, 1973.

H. C. Jaggers, R. J. Bowser, F. J. Weinberg, and S. S. Sandhu. The effect of electric fields on burning velocity. *Combustion and Flame*, 19(1):135–136, 1972.

R.J. Bowser and F.J. Weinberg. The effect of direct electric fields on normal burning velocity. *Combustion and Flame*, 18(2):296–300, April 1972.

AB Fialkov. Investigations on ions in flames. *Progress in Energy and Combustion Science*, 23:399–528, 1997.

S. D. Marcum and B. N. Ganguly. Electric-field-induced flame speed modification. *Combustion and Flame*, 143(1-2):27–36, 2005.

D. L. Wisman, S. D. Marcum, and B. N. Ganguly. Electrical control of the thermodiffusive instability in premixed propane-air flames. *Combustion and Flame*, 151(4):639–648, 2007.

J. Lawton and F. J. Weinberg. Maximum Ion Currents from Flames and the Maximum Practical Effects of Applied Electric Fields. *Proceedings of the Royal Society A: Mathematical, Physical and Engineering Sciences*, 277(1371):468–497, February 1964.

Manh Vu Tran and Min Suk Cha. Correction of edge-flame propagation speed in a counterflow, annular slot burner. *Combustion and Flame*, 162(12):4671–4672, 2015.

Manh Vu Tran and Min Suk Cha. Propagating nonpremixed edge-flames in a counterflow, annular slot burner under DC electric fields. *Combustion and Flame*, 173:114–122, 2016.

Manh Vu Tran and Min Suk Cha. Time evolution of propagating nonpremixed flames in a counterflow, annular slot burner under AC electric fields. *Proceedings of the Combustion Institute*, 36(1):1421–1430, 2017.

Daniel C. Murphy, Mario Sánchez-Sanz, and Carlos Fernandez-Pello. The role of non-thermal electrons in flame acceleration. *Combustion and Flame*, 182:48–57, 2017.

F.G. Roper. The prediction of laminar jet diffusion flame sizes: Part I. Theoretical model. *Combustion and Flame*, 29:219–226, January 1977.

Kunning Gabriel Xu. Plasma sheath behavior and ionic wind effect in electric field modified flames. *Combustion and Flame*, 161(6):1678–1686, June 2014.

Mario Sánchez-Sanz, Daniel C. Murphy, and C. Fernandez-Pello. Effect of an external electric field on the propagation velocity of premixed flames. *Proceedings of the Combustion Institute*, 35(3):3463–3470, 2015.

Carmen Guerra-Garcia and Manuel Martinez-Sanchez. Counterflow nonpremixed flame DC displacement under AC electric field. *Combustion and Flame*, 162(11):4254–4263, 2015.

Dae Geun Park, Suk Ho Chung, and Min Suk Cha. Bidirectional ionic wind in nonpremixed counterflow flames with DC electric fields. *Combustion and Flame*, 168:138–146, 2016.

SP Burke and TEW Schumann. Diffusion flames. *Proceedings of the Symposium on Combustion*, 1-2(10):2–11, January 1948.

MD Smooke, P Lin, JK Lam, and MB Long. Computational and experimental study of a laminar axisymmetric methane-air diffusion flame. *Symposium (International) on Combustion*, pages 575–582, 1991.

Bin Ma, Su Cao, Davide Giassi, Dennis P. Stocker, Fumiaki Takahashi, Beth Anne V. Bennett, Mitchell D. Smooke, and Marshall B. Long. An experimental and computational study of soot formation in a coflow jet flame under microgravity and normal gravity. *Proceedings of the Combustion Institute*, 35(1):839–846, 2015.

Sunny Karnani. *Electric field-driven flame dynamics*. PhD thesis, University of California, Irvine, 2011.

Luck B.W. Peerlings, Viktor N. Kornilov, and Philip de Goey. Flame ion generation rate as a measure of the flame thermo-acoustic response. *Combustion and Flame*, 160(11): 2490–2496, November 2013.

D. Boothman, J. Lawton, S.J. Melinek, and Felix Weinberg. Rates of ion generation in flames. *Symposium (International) on Combustion*, 12(1):969–978, January 1969.

Tamer Badawy, Amit Shrestha, and Naeim Henein. Detection of Combustion Resonance Using an Ion Current Sensor in Diesel Engines. *Journal of Engineering for Gas Turbines and Power*, 134(5):052802, 2012.

Rahul Rao and Damon Honnery. A simplified mechanism for the prediction of the ion current during methane oxidation in engine-like conditions. *Combustion and Flame*, 162 (7):2928–2936, 2015.

S. Karnani, D. Dunn-Rankin, F. Takahashi, Z.-G. Yuan, and D. Stocker. Simulating Gravity in Microgravity Combustion Using Electric Fields. *Combustion Science and Technology*, 184(10-11):1891–1902, October 2012.

Kiyotaka Yamashita, Sunny Karnani, and Derek Dunn-Rankin. Numerical prediction of ion current from a small methane jet flame. *Combustion and Flame*, 156(6):1227–1233, 2009.

Felix Weinberg and Fred Carleton. Ionization and chemiluminescence during the progressive aeration of methane flames. *Combustion and Flame*, 156(12):2276–2284, December 2009.

Sunny Karnani and Derek Dunn-Rankin. Detailed characterization of DC electric field effects on small non-premixed flames. *Combustion and Flame*, 162(7):2865–2872, Jul 2015.

J.M. Goodings, D.K. Bohme, and Chun-Wai Ng. Detailed ion chemistry in methane-oxygen flames. II. Negative ions. *Combustion and Flame*, 36:45–62, January 1979.

J. Prager, U. Riedel, and J. Warnatz. Modeling ion chemistry and charged species diffusion in lean methane–oxygen flames. *Proceedings of the Combustion Institute*, 31(1):1129–1137, January 2007.

S. H. Chung. Stabilization, propagation and instability of tribrachial triple flames. *Proceedings of the Combustion Institute*, 31 I(August):877–892, 2007.

J. Lawton, P. J. Mayo, and F. J. Weinberg. Electrical Control of Gas Flows in Combustion Processes. *Proceedings of the Royal Society A: Mathematical, Physical and Engineering Sciences*, 303(1474):275–298, March 1968.

N. Speelman, M. Kiefer, D. Markus, U. Maas, L.P.H. de Goey, and J.a. van Oijen. Validation of a novel numerical model for the electric currents in burner-stabilized methane–air flames. *Proceedings of the Combustion Institute*, June 2014.

N. Speelman, L.P.H. de Goey, and J.a. van Oijen. Development of a numerical model for the electric current in burner-stabilised methane–air flames. *Combustion Theory and Modelling*, 19(March):159–187, 2015.

M. J. Papac and D. Dunn-Rankin. Modelling electric field driven convection in small combustion plasmas and surrounding gases. *Combustion Theory and Modelling*, 12(1):23–44, December 2007.

Memdouh Belhi, Pascale Domingo, and Pierre Vervisch. Direct numerical simulation of the effect of an electric field on flame stability. *Combustion and Flame*, 157(12):2286–2297, dec 2010.

M. J. Papac. *Electrical aspects of gaseous fuel flames for microgravity combustion and combustion control.* PhD thesis, University of California, Irvine, 2005.

R. S. Sigmond. Simple approximate treatment of unipolar space-charge-dominated coronas: The Warburg law and the saturation current. *Journal of Applied Physics*, 53(2):891, 1982.

C J Dasch. One-dimensional tomography: a comparison of Abel, onion-peeling, and filtered backprojection methods. *Applied optics*, 31:1146–1152, 1992.

FG Roper, C Smith, and AC Cunningham. The Prediction of Laminar Jet Diffusion Flame Sizes: Part II. Experimental Verification. *Combustion and Flame*, 4, 1977.

S H Chung and C K Law. Burke–Schumann Flame with Streamwise and Preferential Diffusion. *Combustion Science and Technology*, 37(1-2):21–46, 1984.

P.B. Sunderland, Z.G. Yuan, and D.L. Urban. Fourth International Microgravity Combustion Workshop. *Fourth International Microgravity Combustion Workshop*, pages 129–132, 1997.

Carlos Vázquez-Espí. Analysis of Axisymmetric Laminar Jet Diffusion Flames for Small Values of the Stoichiometric Mixture Fraction. *Combustion Science and Technology*, 171 (1):1–38, 2001.

S. S. Krishnan, J. M. Abshire, P. B. Sunderland, Z.-G. Yuan, and J. P. Gore. Analytical predictions of shapes of laminar diffusion flames in microgravity and earth gravity, 2008.

MD Smooke, Y Xu, RM Zurn, and P Lin. Computational and experimental study of OH and CH radicals in axisymmetric laminar diffusion flames. *Symposium (International) on Combustion*, pages 813–821, 1992.

A Ern and Mitchell Smooke. Vorticity-Velocity Formulation for Three-Dimensional Steady Compressible Flows. *Journal of Computational Physics*, 105(1):58–71, 1993.

K.T. Walsh, M.B. Long, M.a. Tanoff, and M.D. Smooke. Experimental and computational study of CH, CH*, and OH* in an axisymmetric laminar diffusion flame. *Symposium (International) on Combustion*, 27(1):615–623, January 1998.

I. Barmina, M. Purmalis, R. Valdmanis, and M. Zake. Electrodynamic Control of the Combustion Characteristics and Heat Energy Production. *Combustion Science and Technology*, 188(2):190–206, February 2016.

J Hu, Boris Rivin, and Eran Sher. The effect of an electric field on the shape of co-flowing and candle-type methane–air flames. *Experimental Thermal and Fluid Science*, 21:124–133, 2000.

Lee Sang Min, Park Cheol Soo, Cha Min Suk, and Chung Suk Ho. Effect of electric fields on the liftoff of nonpremixed turbulent jet flames. *Plasma Science, IEEE Transactions on*, 33(5):1703–1709, 2005.

S. H. Won, M. S. Cha, C. S. Park, and S. H. Chung. Effect of electric fields on reattachment and propagation speed of tribrachial flames in laminar coflow jets. *Proceedings of the Combustion Institute*, 31 I:963–970, 2007.

S. H. Won, S. K. Ryu, M. K. Kim, M. S. Cha, and S. H. Chung. Effect of electric fields on the propagation speed of tribrachial flames in coflow jets. *Combustion and Flame*, 152(4): 496–506, 2008.

Yuan Xiong, Min Suk Cha, and Suk Ho Chung. AC electric field induced vortex in laminar coflow diffusion flames. *Proceedings of the Combustion Institute*, 35(3):3513–3520, 2015.

Yuan Xiong, Suk Ho Chung, and Min Suk Cha. A parametric study of AC electric field-induced toroidal vortex formation in laminar nonpremixed coflow flames. *Combustion and Flame*, 182:142–149, 2017.

Johannes Kuhl, Gordana Jovicic, Lars Zigan, and Alfred Leipertz. Transient electric field response of laminar premixed flames. *Proceedings of the Combustion Institute*, 34(2): 3303–3310, January 2013.

Johannes Kuhl, Gordana Jovicic, Lars Zigan, Stefan Will, and Alfred Leipertz. Influence of electric fields on premixed laminar flames: Visualization of perturbations and potential for suppression of thermoacoustic oscillations. *Proceedings of the Combustion Institute*, September 2014.

Johannes Kuhl, Thomas Seeger, Lars Zigan, Stefan Will, and Alfred Leipertz. On the effect of ionic wind on structure and temperature of laminar premixed flames influenced by electric fields. *Combustion and Flame*, 176:391–399, 2017.

Yu-chien Chien, Koji Yamashita, and Derek Dunn-rankin. Electrical Aspects of Impinging Flames. pages 1–12, 2013.

Vinicius M. Sauer and Derek Dunn-Rankin. Impinging nonpremixed coflow methane-air flames with unity Lewis number. *Proceedings of the Combustion Institute*, 36(1):1411–1419, 2015.

A G Gaydon and H G Wolfhard. *Flames, their structure, radiation, and temperature*. Halsted Press book. Chapman & Hall, 1979.

A G Gaydon. *The Spectroscopy of Flames*. Wiley, 1957.

H Reisler, M Mangir, and C. Wittig. The kinetics of free radicals generated by IR laser photolysis. II. Reactions of C2(X 1 Σ +g), C2(a 3 Π u), C3(X̄ 1 Σ +g) and CN(X 2 Σ +) with O2. *Chemical Physics*, 47(1):49–58, 1980.

K. Devriendt, H. Van Look, B. Ceursters, and J. Peeters. Kinetics of formation of chemiluminescent CH(A2Δ) by the elementary reactions of C2H(X2 Σ+) with O(3P) and O2(X3Σg−): A pulse laser photolysis study. *Chemical Physics Letters*, 261(4-5):450–456, 1996.

K.H. Becker, H.H. Brenig, and T. Tatarczyk. Lifetime measurements on electronically excited CH(A2Δ) radicals. *Chemical Physics Letters*, 71(2):242–245, 1980.

Nancy L. Garland and David R. Crosley. On the collisional quenching of electronically excited OH, NH and CH in flames. *Symposium (International) on Combustion*, 21(1): 1693–1702, 1988.

Masayuki Tamura, Pamela a. Berg, Joel E. Harrington, Jorge Luque, Jay B. Jeffries, Gregory P. Smith, and David R. Crosley. Collisional quenching of CH(A), OH(A), and NO(A) in low pressure hydrocarbon flames. *Combustion and Flame*, 114(3-4):502–514, 1998.

Davide Giassi, Su Cao, Beth Anne V Bennett, Dennis P. Stocker, Fumiaki Takahashi, Mitchell D. Smooke, and Marshall B. Long. Analysis of CH* concentration and flame heat release rate in laminar coflow diffusion flames under microgravity and normal gravity. *Combustion and Flame*, 167:198–206, 2016.

Florian Altendorfner, Johannes Kuhl, Lars Zigan, and Alfred Leipertz. Study of the influence of electric fields on flames using planar LIF and PIV techniques. *Proceedings of the Combustion Institute*, 33(2):3195–3201, January 2011.

M J Papac and D Dunn-Rankin. Canceling buoyancy of gaseous fuel flames in a gravitational environment using an ion-driven wind. *Annals of the New York Academy of Sciences*, 1077: 585–601, September 2006.

Felix Jiri Weinberg. *Optics of Flames: Including Methods for the Study of Refractive Index Fields in Combustion and Aerodynamics.* Butterworths, 1963.

H G Weller, G Tabor, H. Jasak, and C. Fureby. A tensorial approach to computational continuum mechanics using object-oriented techniques. *Computers in Physics*, 12(6):620, 1998.

David G. Goodwin, Harry K. Moffat, and Raymond L. Speth. Cantera: An object-oriented software toolkit for chemical kinetics, thermodynamics, and transport processes. `http://www.cantera.org`, 2017. Version 2.3.0.

Gregory P. Smith, David M. Golden, Michael Frenklach, Nigel W. Moriarty, Boris Eiteneer, Mikhail Goldenberg, C. Thomas Bowman, Ronald K. Hanson, Soonho Song, William C. Gardiner, Jr., Vitali V. Lissianski, , and Zhiwei Qin. Gri-mech 3.0,. `http://www.me.berkeley.edu/gri_mech/`, 1999.

C. S. Panoutsos, Y. Hardalupas, and a. M K P Taylor. Numerical evaluation of equivalence ratio measurement using OH* and CH* chemiluminescence in premixed and non-premixed methane-air flames. *Combustion and Flame*, 156(2):273–291, 2009.

Trupti Kathrotia. *Reaction Kinetics Modeling of OH*, CH*, and C2* Chemiluminescence.* PhD thesis, 2011.

Kevin T Walsh. *Quantitative Characterizations of Coflow Laminar Diffusion Flames in a Normal Gravity and Microgravity Environment.* PhD thesis, Yale University, 2000.

Joel M Hall, Jaap De Vries, Anthony R Amadio, and Eric L Petersen. Towards a Kinetics Model of CH Chemiluminescence. (January), 2005.

Kevin T. Walsh, Joseph Fielding, and Marshall B. Long. Effect of light-collection geometry on reconstruction errors in Abel inversions. *Optics letters*, 25(7):457–459, 2000.

Davide Giassi. *Optical Diagnostics Applied to Quantitative Characterization of Coflow Laminar Diffusion Flames in Microgravity and Normal Gravity.* PhD thesis, Yale Univeristy, 2017.

Derek Dunn-Rankin and Felix Weinberg. Location of the Schlieren Image in Premixed Flames: Axially Symmetrical Refractive Index Fields. *Combustion and Flame*, 113(3): 303–311, May 1998.

FB Carleton and FJ Weinberg. Electric field-induced flame convection in the absence of gravity. *Nature*, 1987.

Derek Dunn-Rankin and Felix J Weinberg. Using large electric fields to control transport in microgravity. *Annals of the New York Academy of Sciences*, 1077:570–84, September 2006.

P. B. Sunderland, B. J. Mendelson, Z. G. Yuan, and D. L. Urban. Shapes of buoyant and nonbuoyant laminar jet diffusion flames. *Combustion and Flame*, 116(3):376–386, 1999.

D C Murphy, M Sánchez-Sanz, and C Fernandez-Pello. An experimental and numerical study of flames in narrow channels with electric fields. *Journal of Physics: Conference Series*, 557:012076, 2014.

Raymond B. Edelman, Owen F. Fortune, Gertrude Weilerstein, Thomas H. Cochran, and John B. Haggard. An analytical and experimental investigation of gravity effects upon laminar gas jet-diffusion flames. *Symposium (International) on Combustion*, 14(1):399–412, 1973.

Yu-Chien Chien. *Electrical Aspects of Impinging Flames.* PhD thesis, University of California, Irvine, 2015.

Appendices

A Burner Electrical Distributions

Fig. A.1 shows the electric field lines and constant electric potential lines created by a -1 kV voltage applied between a coflow burner and an electrode mesh (no flame). Both coflow burners are shown. These solutions were produced numerically by discretizing the Laplace equation for solving for the electric potential Φ in cylindrical coordinates.

$$\frac{1}{r}\frac{\partial}{\partial r}\left(r\frac{\partial \Phi}{\partial r}\right)+\frac{\partial^2 \Phi}{\partial z^2}=0 \tag{A.1}$$

The following boundary conditions were also discretized and solved with Eq. (A.1).

$$\left.\frac{\partial \Phi}{\partial r}\right|_{r=0}=0 \tag{A.2a}$$

$$\left.\frac{\partial \Phi}{\partial r}\right|_{r=\infty}=0 \tag{A.2b}$$

$$\Phi_{burner}=0 \tag{A.2c}$$

$$\Phi_{mesh}=V_{applied} \tag{A.2d}$$

Once Φ is obtained, the electric field can be computed by $\vec{E}=-\nabla\Phi$. Eq. (A.3) shows this relationship in cylindrical coordinates.

$$\vec{E}=-\frac{\partial \Phi}{\partial r}\hat{\mathbf{r}}-\frac{\partial \Phi}{\partial z}\hat{\mathbf{z}} \tag{A.3}$$

Fig. A.1b shows that the electric field lines for a flush tube burner are all parallel everywhere. Fig. A.1a shows that the electric field lines are parallel far away from the burner tube. Close to the tube, the electric field lines are skewed.

Fig. A.2 shows the magnitude of the local electric field normalized by $E_{nominal}$ (defined

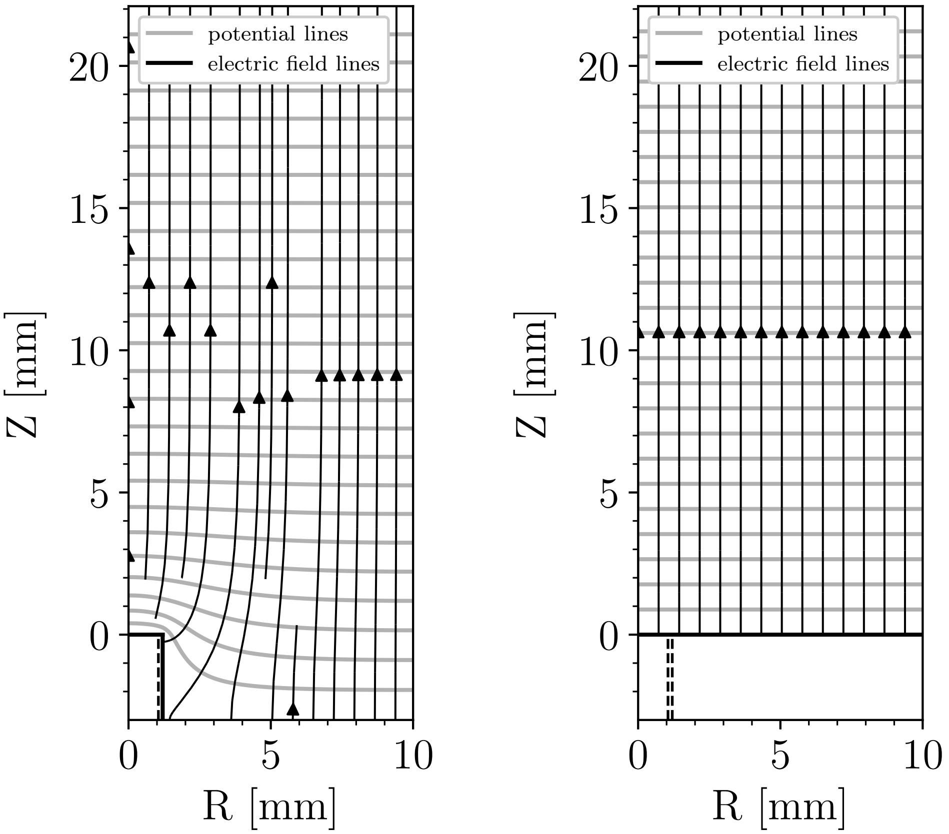

(a) extruded tube

(b) flush tube

Figure A.1: Electric field lines and constant electric potential lines. -1 kV applied to the mesh.

in Ch. 3). Fig. A.2a shows that the local electric field for a flush tube coflow burner is uniform and equal to the nominal field strength everywhere. Fig. A.2b shows that for an extruded tube burner the local field is nearly uniform and equal to the nominal field strength everywhere accept near the tube. Near the tube, the local field exceeds the nominal field strength especially near the very corner of the tube where the local field exceeds the nominal field strength by a factor of 5.

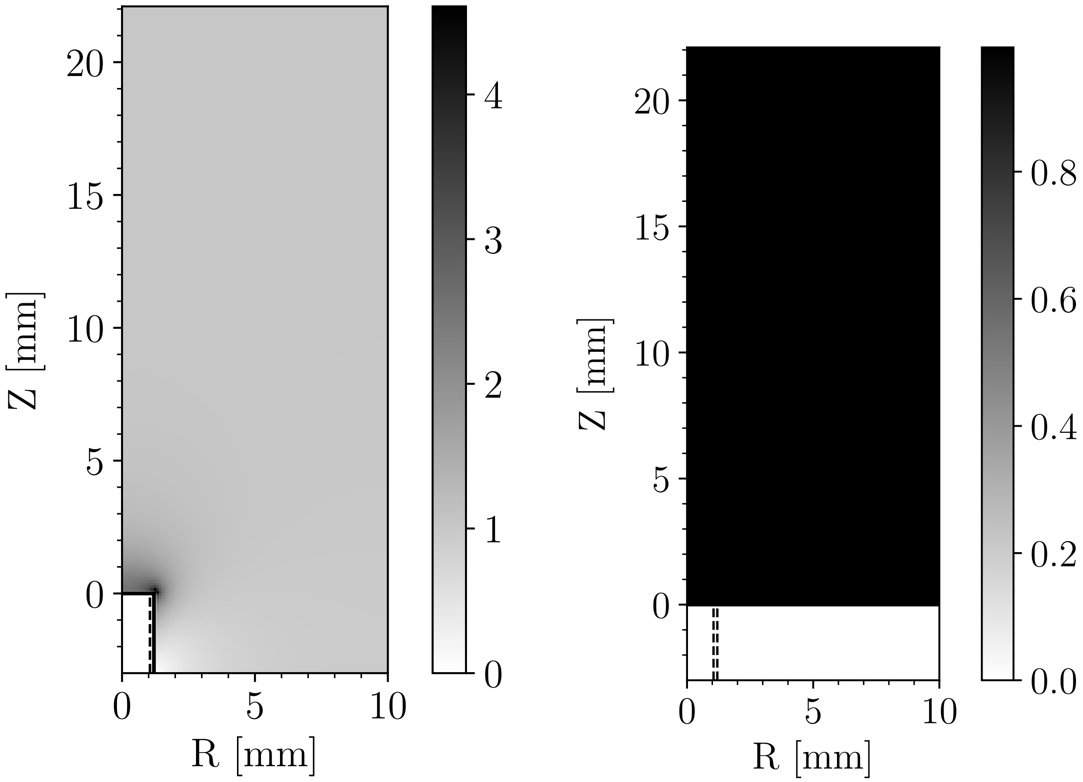

(a) extruded tube

(b) flush tube

Figure A.2: Local electric field strength (magnitude) normalized by $E_{nominal}$.

B Flame Contour Details

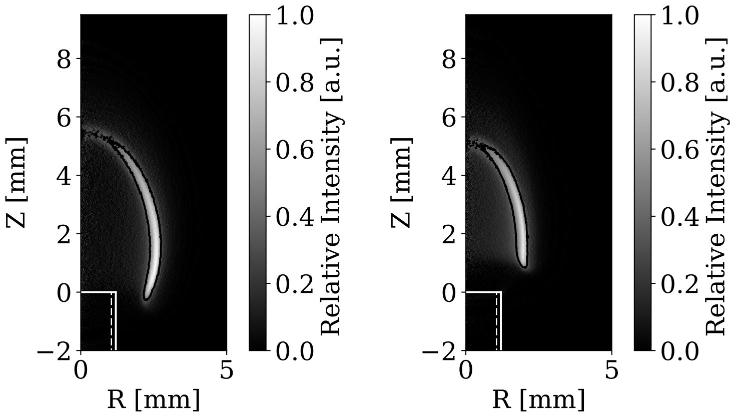

(a) 0.0 kV/cm

(b) 3.5kV/cm

Figure B.3: 40% flame contour. Coflow (extruded) - 2.2cm , 27mL/min , E > 0. These images are normalized by the maximum pixel intensity found within its own respective image.

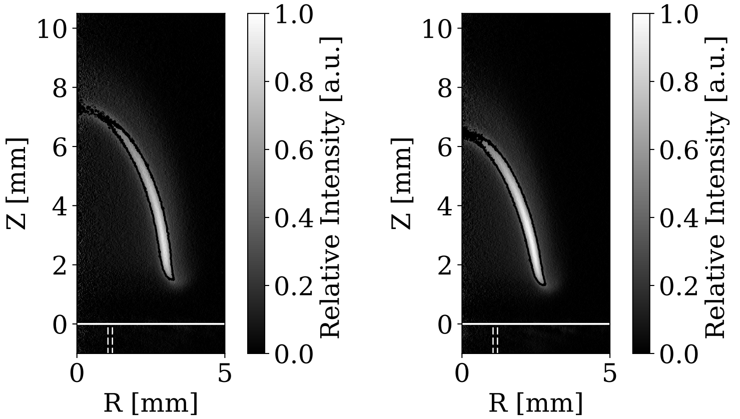

(a) 0.0 kV/cm

(b) 4.54 kV/cm

Figure B.4: 40% flame contour. Coflow (flush) - 2.2cm , 27mL/min , E > 0. These images are normalized by the maximum pixel intensity found within its own respective image.

The flame contours described in Figs. 4.2 and 4.5 were obtained by determining the contour line surrounding the portion of the flame with a pixel intensity greater than 40% of the image's maximum pixel intensity. Figs. B.3 and B.4 show sample 40% flame contour lines superimposed onto the image it was calculated from. Because the abel inversion algorithm inherently creates a slight bit of noise near the centerline of the image, below 40% of the maximum pixel intensity is not able to capture reasonable flame contours for all images. The 40% contour line was found to be an optimal choice for representing the shape of the flame's CH^* chemiluminescence spatial region. The only region where it does not represent well is near the flame tip because the noise created by the abel inversion algorithm creates smaller contour rings. Therefore, only the largest contour ring is used and the contours rings near the flame tip are discarded. The other spatial characteristics are captured well with the largest 40% contour line, including flame thicknesses, curvature, and base height.

What could also be noticed from Figs. B.3 and B.4 is the dim light signal surrounding the main flame body, particularly radially outward and above the flame. This light signal is a real result from the chemiluminescence of the flame and not noise created by the post processing. This dimmer light signal, however, is not being produced by CH^* chemiluminescence. Giassi et al. [2016] showed that it is likely due to a CO_2 chemiluminescence peak near 431 nm which is able to pass through the 431 nm filter. The choice of a 40% contour line was also made to neglect this portion of captured light.

C Numerical Simulation - Input Properties

C.1 Evaluation of the dynamic viscosity calculation

Because the Sutherland Transport model (Eq. (6.6)) is the preferred method for calculating the dynamic viscosity in OpenFOAM, it is briefly evaluated here how well this model matches the calculation of viscosity made by Cantera and Lennard-Jones parameters.

Cantera uses Eq. C.4 to calculate the viscosity of species k.

$$\mu_k = \frac{5}{16}\frac{\sqrt{\pi M_k KT/N_A}}{\pi\sigma^2\Omega_\mu} \tag{C.4}$$

K is the Boltzmann constant, N_A is Avogrado's number, σ is the characteristic diameter of the molecule given by the Leonard Jones parameters, and Ω_μ is the collisional integral of viscosity. Ω_μ is a known and tabulated function of KT/ϵ where ϵ is another Lennard-Jones parameter called the characteristic energy

The coefficient of determination, R^2, is a value that is used to determine how well a model fits to a data set. In this case the data set is the dynamic viscosity computed by Cantera (Eq. (C.4)) and the model is the Sutherland transport model (Eq. (6.6)). R^2 is calculated by Eq. (C.5), where Y is the data set, $\overline{Y}$ is the mean value of the data set, and f is the predicted values of the model. R^2 is represented as a percent where a model with an R^2 of 100% is considered a perfect model for the data set.

$$R^2 = 100 \times \left(1 - \frac{\sqrt{\sum_i \left(Y[i] - f[i]\right)^2}}{\sqrt{\sum_i \left(Y[i] - \overline{Y}\right)^2}}\right) \tag{C.5}$$

Fig. C.5 shows the results for air and CH_4. Air was found to have A_s and T_s values of

1.693e-6 and 230.35, respectively, and an R^2 of 99.82%. Methane was found to have A_s and T_s values of 1.103e-6 and 249.54, respectively, and an R^2 of 99.87%. The R^2 values for other species fall within the range of 99.77 to 99.99%. As it can be seen by Fig. C.5 and the R^2 values, the dynamic viscosities computed through Cantera are well preserved by the Sutherland transport model.

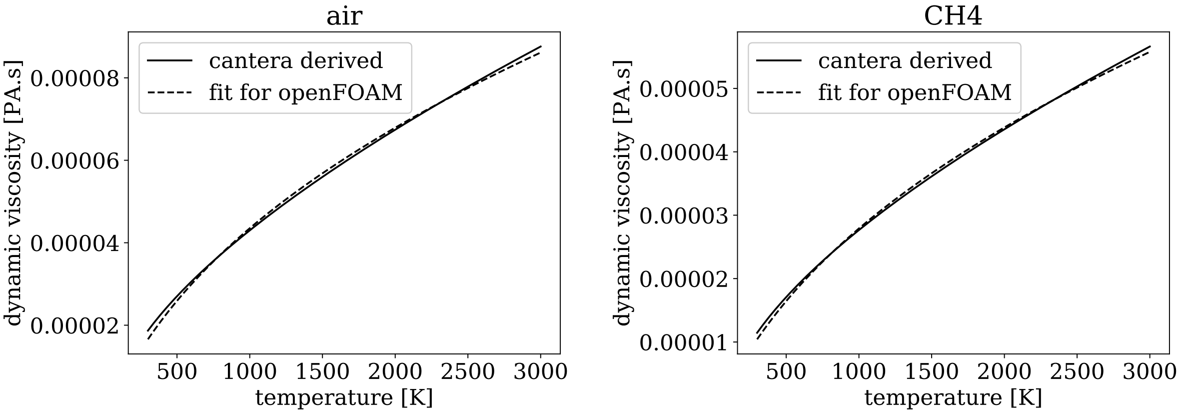

(a) air

(b) CH_4

Figure C.5: Comparison of dynamic viscosities: Cantera derived vs fit to Sutherland's Law (for OpenFOAM)

C.2 Evaluation of using Sc and Le in transport equations

The use of a single mixture value for D instead of using more detailed methods, e.g. multicomponent diffusion, greatly improves computational time. The default operation for calculating diffusion coefficients in OpenFOAM is to use unity Schmidt number to determine a mixture value of D for all species. However, this was found to over predict flame geometries significantly. Other common dimensionless number options are unity Lewis number and $Sc = 0.7$. The definitions of Schmidt number and Lewis number are shown in Eqs. (C.6) and (C.7), respectively.

$$Sc = \frac{\mu}{\rho D} \tag{C.6}$$

$$Le = \frac{\lambda}{\rho D c_p} \tag{C.7}$$

Using these two equations and the Eucken formula, Eq. (6.17), it can be shown that Le is proportional to Sc times some function of c_p. That is,

$$Le = Sc\frac{c_v}{c_p}(1.32 + 1.77\frac{R}{c_v}). \tag{C.8}$$

An ideal value for either dimensionless number for use in the simulations is one that predicts well the true values of Sc and Le and do not vary greatly with temperature or specie-to-specie interaction. Fig. C.6 shows the calculation of Schmidt and Lewis numbers as a function of temperature for major reactant species diffusing in a bath gas composed of mostly air. Fig. C.7 is the same but for the major product species.

It can be seen from Fig. C.6 that both Sc = 0.7 and Le = 1 work very well with the major reactants. Both predict reasonably well the actual Sc and Le values and have weak variations with both temperature and species-to-species interaction. However, Sc = 0.7 is the better predictor of the two in all categories. Fig. C.7 show that the actual Sc and Le values for major products are not well predicted and have vary strong variations.

The same analysis was performed in Figs. C.8 and C.9 but this time with a bath gas composed primarily of methane. Similar results were found, actual Sc and Le values are well predicted and show weak variations between temperature and specie-to-specie interactions for major reactants but are poor with major products. Sc = 0.7 is again found to be the slightly better predictor.

To quantify further the results shown in Figs. C.6 - C.9, we can calculate the variation of the cantera derived Sc and Le numbers from their mean values to determine how they vary with temperature. The coefficient of variation, COV, is useful in this type of analysis. The

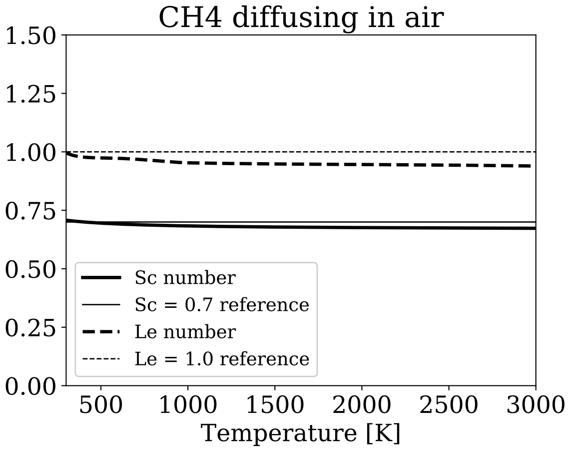

(a) CH_4 in air

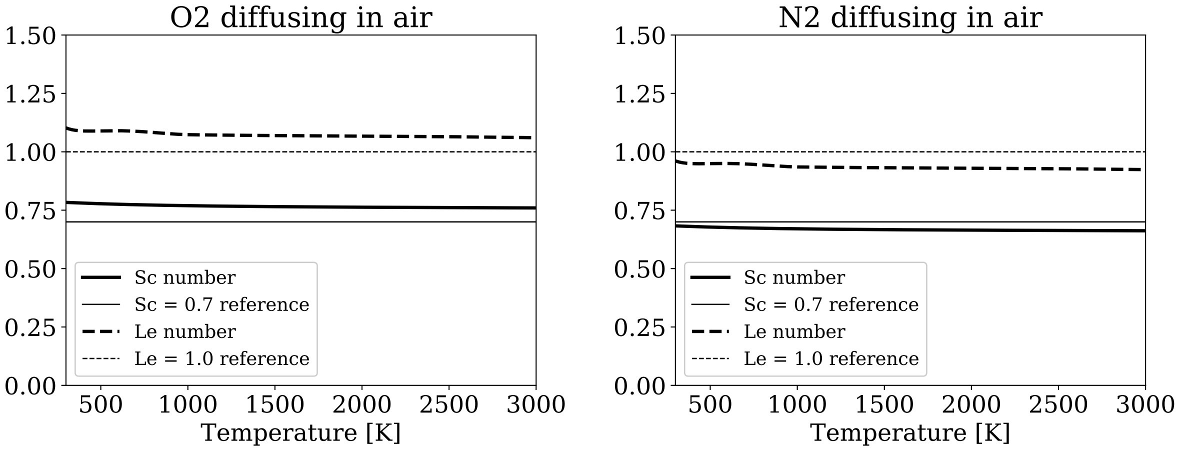

(b) O_2 in air

(c) N_2 in air

Figure C.6: Comparison of Schmidt and Lewis numbers of reactants in a bath gas composed of air.

COV is defined as,

$$COV = \frac{\sqrt{\frac{1}{N}\sum_{k=1}^{N}\left(Di_k - \frac{1}{N}\sum_{k=1}^{N} Di_k\right)^2}}{\frac{1}{N}\sum_{k=1}^{N} Di_k}, \tag{C.9}$$

where, Di is an arbitrary dimensionless number (i.e. Sc or Le). Notice that the numerator is the definition of the standard deviation. Therefore, the COV is the standard deviation normalized by the mean value of Di. Fig. C.10 shows the COV for the Sc and Le numbers for different species diffusing through different bath gases.

Fig. C.10 shows that H_2O as a bath gas has the worse dependence with temperature and is

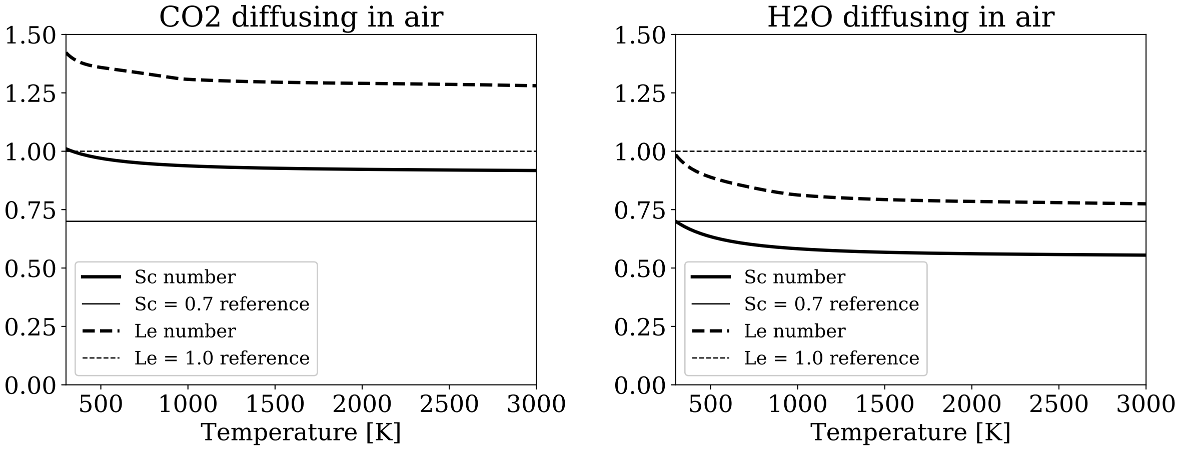

(a) CO_2 in air

(b) H_2O in air

Figure C.7: Comparison of Schmidt and Lewis numbers of products in a bath gas composed of air.

significantly higher than the other major species being analyzed. H_2O is also seen to have a strong dependence with temperature as a species being diffused through each of the bath gases. Overall, the temperature dependence results seem nearly identical for both Sc and Le numbers when normalized.

The cantera derived Sc and Le numbers can also be analyzed for their variation from the values that will be used in OpenFOAM; $Sc = 0.7$ and $Le = 1.0$, respectively. A similar value to the COV can be used for this analysis. In this case, COV' can be defines as,

$$COV' = \frac{\sqrt{\frac{1}{N}\sum_{k=1}^{N}\left(Di_k - Di'\right)^2}}{Di'}, \tag{C.10}$$

where, Di' is a constant value of either $Sc = 0.7$ or $Le = 1.0$.

The results for COV' are shown in Fig. C.11. The variation of $Sc = 0.7$ and $Le = 1.0$ from the cantera derived values are seen to be especially significant for major products species, CO_2 and H_2O, as both a bath gas and a diffusing species. It is also found that both $Sc = 0.7$ and $Le = 1.0$ are particularly bad predictors for diffusion of H_2 in all bath gas compositions.

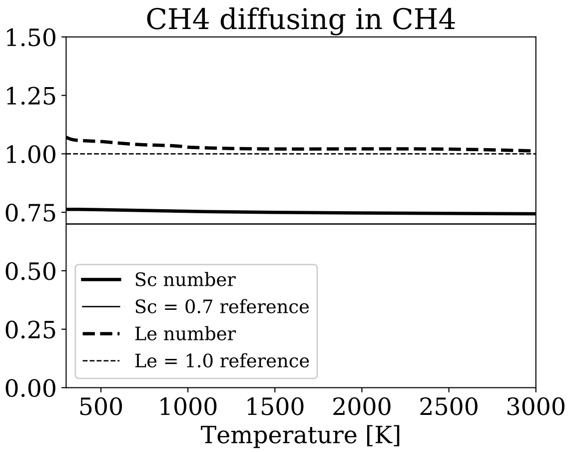

(a) CH_4 self diffusion

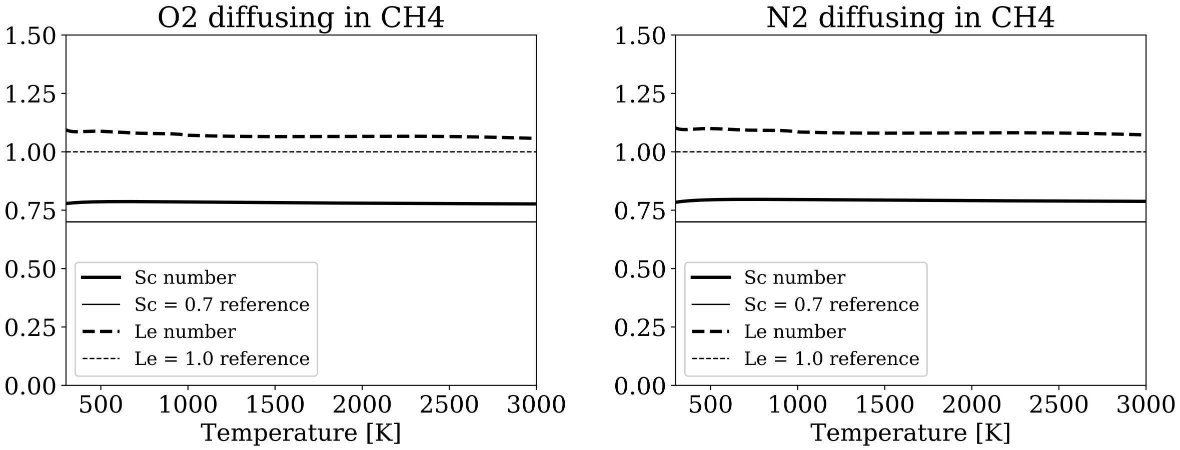

(b) O_2 in CH_4

(c) N_2 in CH_4

Figure C.8: Comparison of Schmidt and Lewis numbers of reactants in a bath gas composed of methane.

Fig. C.11 shows that $Le = 1$ may have a slight advantage over $Sc = 0.7$ due to the slightly better diffusion of the major reactants, CH_4. O_2, and N_2. However, the advantage is so narrow that it may be treated as negligible.

C.3 Final Remarks

OpenFOAM is an open source software that has all the fundamentals of a CFD program and allows its users to quickly build and customize their simulations to their needs. The

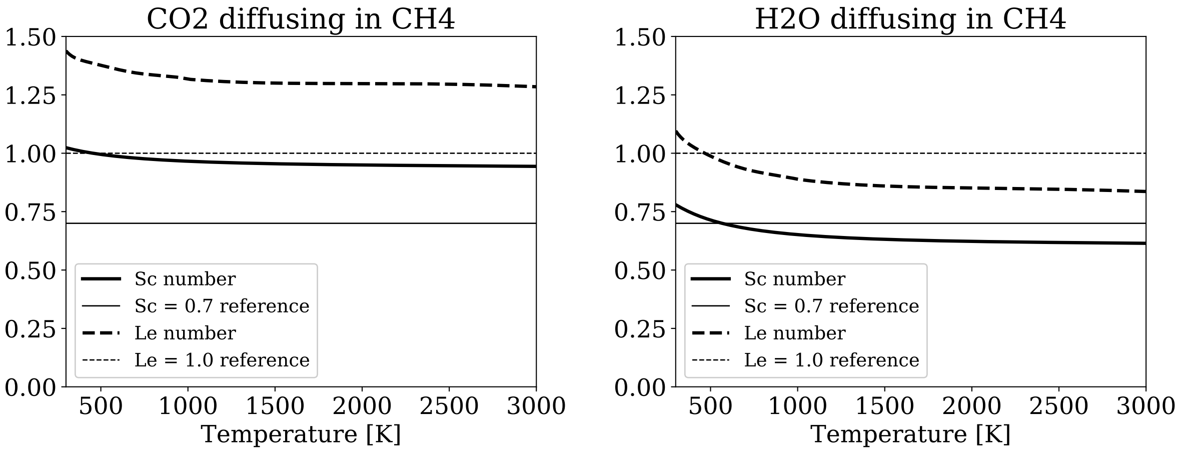

(a) CO_2 in CH_4 (b) H_2O in CH_4

Figure C.9: Comparison of Schmidt and Lewis numbers of products in a bath gas composed of methane.

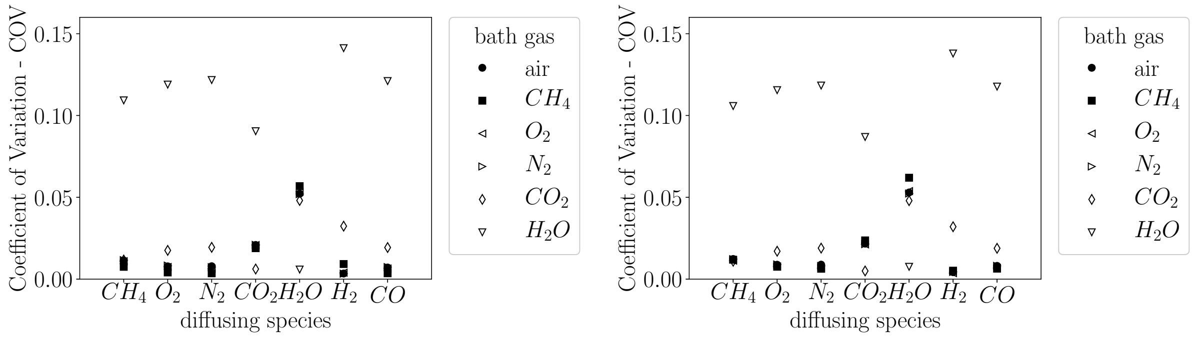

(a) Sc (b) Le

Figure C.10: Temperature dependence of Sc and Le numbers using coefficient of variation.

OpenFOAM base line code contains many simplifications for quick compilation and computational times. Among these simplifications is how OpenFOAM handles transport. That is, air viscosity is calculated as air and diffusion coefficients are determined by unity Sc number. The modifications to this baseline procedure was to calculate viscosity of individual species, input these properties into OpenFOAM, and determine a dimensionless number that is more suitable than $Sc = 1.0$. Here, it was shown that both $Sc = 0.7$ and $Le = 1.0$ both produce a much better transport model than unity Sc. More accurate transport could be made in OpenFOAM by implementing multicomponent diffusion. Aside from the task of creating a

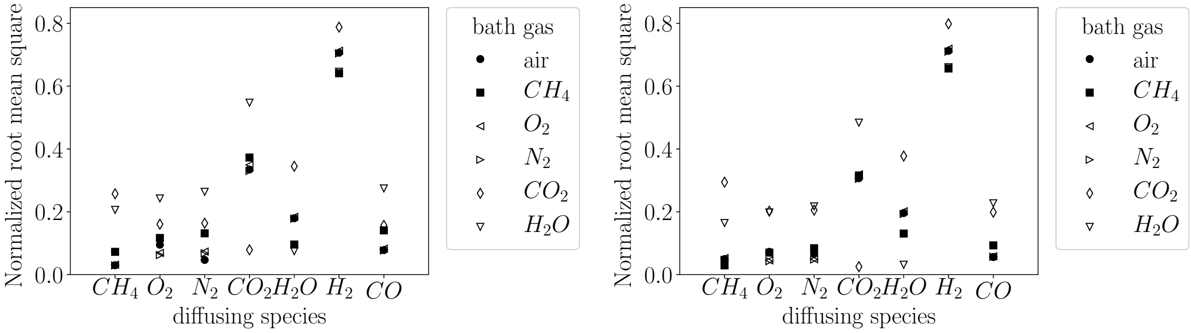

(a) Sc

(b) Le

Figure C.11: Variation of Sc and Le numbers from $Sc = 0.7$ and $Le = 1.0$ using RMS with respect to $Sc = 0.7$ and $Le = 1.0$, respectively.

code to implement multicomponent transport into OpenFOAM, one major drawback is the cost to the computational time of the simulations. Therefore, the $Sc = 0.7$ was chosen as the transport model for the simulations in this study. Multicomponent transport will be left open as an option for future simulations.